INFORMATION TO USERS

This manuscript has been reproduced from the microfilm master. UMI films the text directly from the original or copy submitted. Thus, some thesis and dissertation copies are in typewriter face, while others may be from any type of computer printer.

The quality of this reproduction is dependent upon the quality of the copy submitted. Broken or indistinct print, colored or poor quality illustrations and photographs, print bleedthrough, substandard margins, and improper alignment can adversely affect reproduction.

In the unlikely event that the author did not send UMI a complete manuscript and there are missing pages, these will be noted. Also, if unauthorized copyright material had to be removed, a note will indicate the deletion.

Oversize materials (e.g., maps, drawings, charts) are reproduced by sectioning the original, beginning at the upper left-hand corner and continuing from left to right in equal sections with small overlaps.

Photographs included in the original manuscript have been reproduced xerographically in this copy. Higher quality 6" x 9" black and white photographic prints are available for any photographs or illustrations appearing in this copy for an additional charge. Contact UMI directly to order.

Bell & Howell Information and Learning
300 North Zeeb Road, Ann Arbor, MI 48106-1346 USA
800-521-0600

UMI®

How does lightning initiate and what controls lightning frequency?

Vicki Schroeder

A dissertation submitted in partial fulfillment
of the requirements for the degree of

Doctor of Philosophy

University of Washington

2000

Program Authorized to Offer Degree: Geophysics

In presenting this dissertation in partial fulfillment of the requirements for the Doctoral degree at the University of Washington, I agree that the Library shall make its copies freely available for inspection. I further agree that extensive copying of the dissertation is allowable only for scholarly purposes, consistent with "fair use" as prescribed in the U.S. Copyright Law. Requests for copying or reproduction of this dissertation may be referred to Bell and Howell Information and Learning, 300 North Zeeb Road, P.O. Box 1346, Ann Arbor, MI 48106-1346, to whom the author has granted "the right to reproduce and sell (a) copies of the manuscript in microform and/or (b) printed copies of the manuscript made from microform."

Signature Schroeder

Date 08/14/2000

University of Washington

Graduate School

This is to certify that I have examined this copy of a doctoral dissertation by

Vicki Schroeder

and have found that it is complete and satisfactory in all respects,
and that any and all revisions required by the final
examining committee have been made.

Chair of Supervisory Committee:

Marcia B Baker

Marcia B. Baker

Reading Committee:

Marcia B Baker

Marcia B. Baker

Robert Holzworth

Dennis Hartmann

Date: 08/14/2000

University of Washington

Abstract

How does lightning initiate and what controls lightning frequency?

by Vicki Schroeder

Chair of Supervisory Committee

Professor Marcia B. Baker

Geophysics

In this thesis we focus on how lightning initiates in thunderstorms and how the subsequent lightning flash rate is controlled by thundecloud properties.

The mechanism by which lightning initiation in thunderclouds occurs is poorly understood. The maximum measured electric fields in clouds are an order of magnitude smaller than the electric fields required for dielectric breakdown of air. We evaluate two possible mechanisms for the initiation of lightning in the relatively low electric fields measured inside thunderstorms. The first hypothesis involves the local enhancement of the in-cloud electric field in the vicinity of hydrometeors. The second hypothesis focusses on high energy cosmic rays that can produce extremely high concentrations of electrons, leading to localized intense electric fields. The conclusion of our analysis is that neither of these mechanisms, operating alone, is entirely consistent with existing observations of the conditions associated with the onset of lightning. We discuss possible reasons for this result, including uncertainties in the measurements themselves.

In our study of lightning flash rate we focussed on three cloud properties which have a strong influence on the cloud electrification process: cloud condensation nucleus concentration, cloud updraft velocity and liquid water and ice entering the chrging zone in the cloud. We found that cloud condensation nucleus concentration was a non-negligible factor in controlling lightning flash rate, with peak lightning flash rate increasing roughly linearly with increasing in a given tropical sound-

ing. Our work shows that peak flash rate was highly sensitive to peak updraft velocity and that there existed significant variations in this relationship on a regional scale, with the flash rates in the tropical location being more sensitive to peak updraft velocity than in mid-latitude continental storms. We considered the feasibility of using lightning flash rate observations to give estimates of the quantity of water and ice that is transported upwards in thunderclouds. For the mid-latitude continental storms in our study we found a strong, roughly linear, relationship between the average flash rate during the storm and condensate. In other regions, however, our model predicted only a weak relationship between these two quantities.

Table of Contents

List of Figures

List of Tables

Acknowledgments

Where to start and end? No thesis is complete without a deep expression of gratitude for one's advisor. Marcia Baker has been patient and caring through my Ph.D odessy. She encouraged me through the inevitable frustrations and allowed me to run with new ideas.

On a professional level I need to thank more people than there is space for on this page. Notably I wish to thank:

- my committee (Robert Holzworth, Dennis Hartmann, Ron Merrill and Robert Houze) for their support and input
- Dr Robert Solomon and Jeremy Smith for assistance with the work in this thesis
- undergraduate researcher Linda Kenoyer who assisted me with the work on corona from ice
- all my officemates over the years for many discussion, both on academic issues and current affairs
- my classmates who helped make my first year here a lot of fun
- and many researchers around the country for discussions, data and more (Robert Roussel Dupré, Anne Boundiou-Clergerie, John Latham, William Winn, Earle Williams, Hugh Christian, Jim Weinman, Kevin Driscoll and the late Ron Geballe)

On a more personal level I wish to thank my mom for her extraordinary efforts to raise my brother and I on her own after my dad passed away. She made sure we received the best education available. Thanks to my brother for moving to Seattle and adding 'family' to the 'what I love about Seattle' column. I would like to thank all the friends I have made here in the last 6 years. Thanks for all the outdoor activites you guys did with me when my brain was fried but my body needed to move.

The best things are generally saved for last and in this case so is the largest 'Thank you'. To Brett: who has contributed so much to my life, my confidence and this work. Thank you for always

being there.

Funding for this work has been provided by the following NASA grants: NAG8-1150 and GEWEX 97-0046.

Chapter 1

Introduction

Throughout time people have been enthralled by lightning. The intense light and accompanying roar left no doubt in our ancestor's minds that this was a powerful force of nature.

The thunderbolt was used as a symbol of power by important figures in the mythology of ancient Greece (Zeus), Egypt (Typhon), the Roman Empire (Jove), India (Indra) and the Norsemen (Thor). Interestingly native people of Southern Africa and the Pacific Northwest both believed that lightning was produced by a magical thunderbird. Fig 1.1 shows my interpretation of a Native American thunderbird. The thunderbird was believed to dive from the clouds to earth, its bright feathers and beating wings resulting in lightning and thunder.

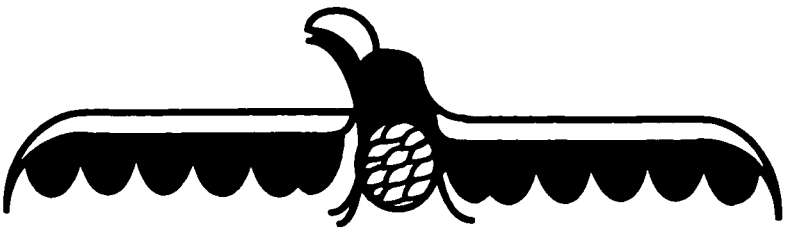

Figure 1.1: My interpretation of a magical thunderbird.

In the middle ages many churches suffered from destructive fires caused by lightning strikes to their steeples. However, some churches seemed exempt. The Cathedral of Geneva, for example, was never damaged by lightning, even when lower church steeples in the area were destroyed (Schonland, 1964). In 1771 the scientist de Saussure investigated this mystery and found that the wooden tower of the church was covered with tinned iron plates that were connected to the metal structure of the tower and to the ground - a fortuitous design!

In 1600 William Gilbert made the first scientific study of electricity. He termed substances that acquire charge when rubbed *electrics*, a word derived from the Greek word *electron* meaning amber.

During the following 150 years natural philosophers, including Sir Isaac Newton, worked on the subject of *electrics* but it was not until the mid-1700's, when Benjamin Franklin turned his attention to the subject, that substantial progress was made. Franklin was the first person to design an experiment to show that lightning was an electrical phenomenon. His original design was actually first performed by Thomas-Francois D'Alibard in France in 1752. A man was placed in a small sentry box with a long iron rod extending above it. The rod's base was insulated. As a thunderstorm came overhead the man brought a grounded wire near the rod producing sparks, just as Franklin predicted. A month later Franklin, unaware of the French result, performed his famous kite experiment. He flew a kite, with a key tied to the bottom of the kite string, during the early stages of a thunderstorm. The kite and string became slightly electrified and the twine, which is slightly conductive on a humid day, served as an antenna which then electrified the key. Franklin found that sparks then jumped from the key to his hand.

In 1773 Franklin pointed out that 'buildings that have their roofs covered with lead or other metal, and spouts of metal continued from the roof into the ground are never hurt by lightning; as whenever it falls on such a building, it passes in the metals and not in the walls'. And so the concept of installing lightning rods to protect buildings from lightning damage was born.

Lightning research lay largely dormant after Franklin's time until the invention of the Boy's camera in 1900 (see Fig 1.2a). The camera consisted of two rotating lenses and as the lightning flash made its way down to the ground the lens was moved. The subsequent offset of the images made it possible to observe the propagation of the lightning channel for the first time and, in fact, to show that the whole channel did not appear instantaneously. The camera enabled the first estimates of channel propagation velocities to be made and also showed that lightning flashes consisted of multiple strokes (Fig 1.2b). More modern cameras that are based on the original Boys design have become known as 'streak' cameras.

The first good data obtained using a Boys camera only came 30 years after its invention. Boys went to the South African Highveld where conditions for observing thunderstorms were more favorable than in his native England. Here, together with a team of South African scientists and engineers lead by Sir Basil Schonland he obtained the first good time-resolved photographs of lightning chan-

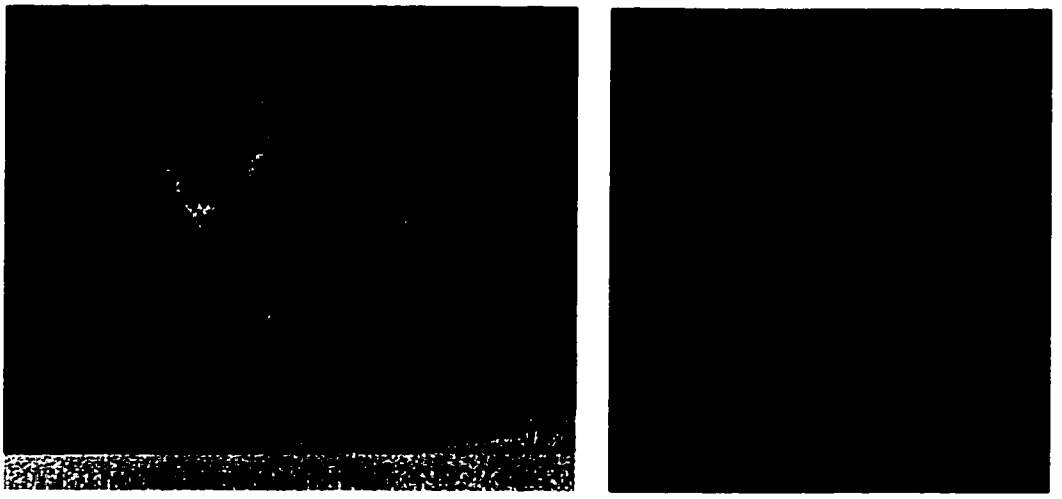

Figure 1.2: (a, left) Photo of Boys with his 'Boys camera' (Schonland, 1964) and, (b, right) an example of a lightning flash photographed with a streak camera. The camera moves during the lightning flash, enabling the resolution of, in this case, 12 individual strokes (Uman, 1987).

nels. Schonland continued to do ground breaking work characterizing lightning channels through the 1940's and 50's.

The early 1900's were also a time in which progress was made to improving our understanding of thunderstorms. In the 1920's C.T.R. Wilson estimated the charge structure in thunderclouds using surface-based electric field measurements and in 1949 a project simply called "The Thunderstorm Project" provided very valuable information about air motions in thunderclouds. WWII fighter pilot veterans flew through the thunderstorms stacked at intervals of several thousand feet. After they entered the cloud and leveled off the pilots took their hands off their controls. As the planes entered updrafts and downdrafts they dropped or shot up thousands of feet. Their altimeter readings enabled scientists to obtain data of updraft and downdraft velocities at various points in the cloud simultaneously.

Since these early projects there have been ongoing investigations into all aspects of thunderstorms. In the remainder of this Chapter I will briefly describe our current understanding of the global circuit, thunderstorm electrification and lightning.

1.1 Global Circuit

The Earth's surface has a net negative charge with an equal and opposite positive charge distributed through the atmosphere. This results in an electric field, known as the *fair weather* field, of 100 – 300 V/m directed downwards. Atmospheric conductivity is finite and increases with altitude. If there was no way to maintain the charge separation between the surface and the atmosphere, the fair weather field would dissipate in 5 to 40 min.

Thunderstorms are among the primary generators (Fig 1.3), maintaining the surface's negative charge through charge deposition via cloud-to-ground lightning (which usually carries a negative charge to ground), negatively charged precipitation and point discharges that transfer positive charge to the atmosphere.

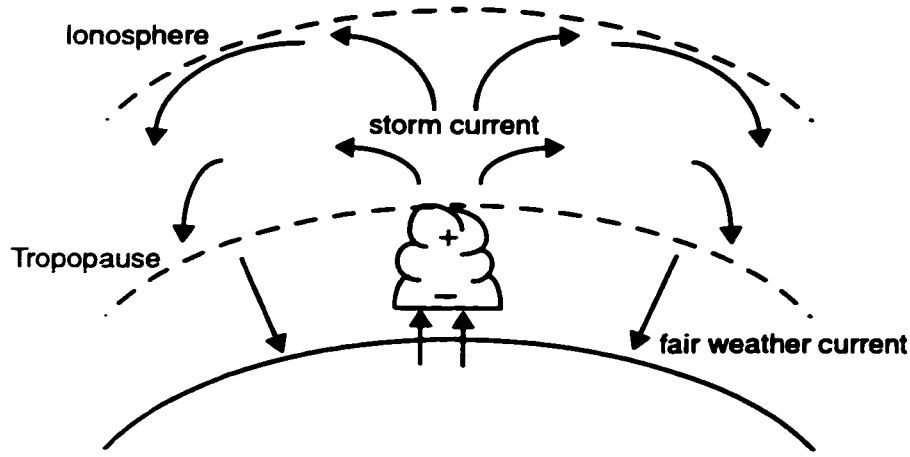

Figure 1.3: Schematic illustrating the global electrical circuit.

1.2 Thunderstorm Electrification

Lightning is most often associated with cumulonimbus clouds which are commonly referred to as thunderclouds if they produce lightning. We focus on these convective clouds in this study but it should be noted that the stratiform clouds can also become electrified and produce lightning.

C.T.R. Wilson's electric field measurements outside the cloud allowed him to infer that thunderstorms had a basic dipole structure with a positively charged region located above a negative charged region (Fig 1.4). These represent the main charge regions within the cloud. In addition, negative ions are attracted by the positive charge in the cloud and collects on the upper boundary of the cloud, forming a negative screening layer. In the lower part of the thundercloud an additional positive region may also be present. This region has two sources: positive ions created by corona from the ground and cosmic rays, and positively charged precipitation.

How do some cumulonimbus clouds become sufficiently electrified to produce lightning? There are two main categories into which cloud electrification theories fall: convective and precipitation based.

The convective theory (Vonnegut, 1953) proposes that charged particles are generated via corona discharge near the ground and by ionization from cosmic rays and radiation which is then moved to the observed locations by convection. This mechanism, however, has trouble accounting for the fact that the negative charge region is found within the same temperature range in clouds that form under very different conditions (Fig 1.4).

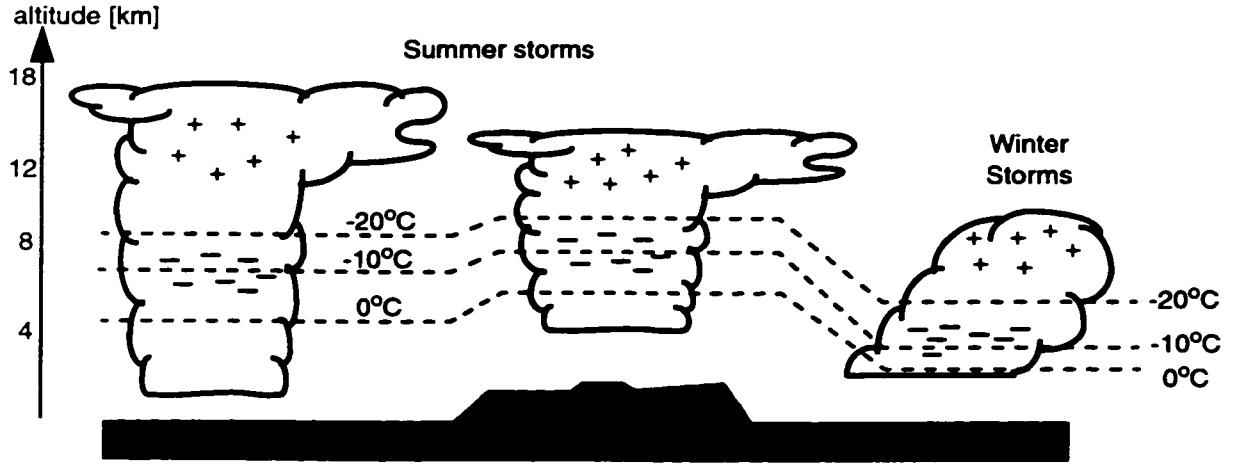

Figure 1.4: Schematic illustrating that the negative charge centers in thunderclouds are located at similar temperatures in storms that have developed under different environmental conditions. Adapted from Krehbiel (1986).

Precipitation based electrification theories involve two spatial scales: a microphysical scale on

which charge transfer between ice particles takes place and a macrophysical scale on which the charged particles are separated within the cloud, resulting in the establishment of an electric field. Precipitation based electrification is commonly accepted as the primary mechanism though it is recognized that the convective theory could be occuring simultaneously as a secondary mechanism.

In the precipitation theory rimed ice particles rise and grow within convective updrafts. As they grow larger, the fall speeds of many of these particles exceeds the updraft velocity and they begin to sediment. A number of these rimed ice particles collide with smaller ice particles rising in the updraft and laboratory studies (Jayaratne *et al.*, 1983; Baker *et al.*, 1987; Saunders *et al.*, 1991; Saunders, 1994) show that charge is transferred during such collisions. The amount and sign of the charge transport depends on the temperature and the amount of liquid water available. As shown in Fig 1.5, under typical thunderstorm conditions the small ice particles are charged positively whilst the larger ones are negatively charged. The region in which the charge transfer takes place is delineated by the -10^oC and -20^oC isotherms - and is referred to as the *charging zone*. The charge is then separated, as a result of the differing fall velocities of the charged ice particles, and an electric field is established within the cloud. If the E- field exceeds a threshold value, in the range $E \sim 100 - 300$ kV/m, lightning is initiated.

1.3 Lightning

Lightning is an electrical discharge that redistributes charge within thunderclouds or between the cloud and the ground or other clouds. There are three main types of lightning flashes:

- cloud-to-ground (CG) flashes which propagate from the cloud down to the ground. CG discharges are most often negative, lowering tens of coulombs of negative charge to ground.

- intra-cloud (IC) flashes which occur wholly within one cloud. IC flashes are the most commonly occuring flashes.

- inter-cloud flashes which propagate between clouds. These are the least frequently occuring flashes of the three.

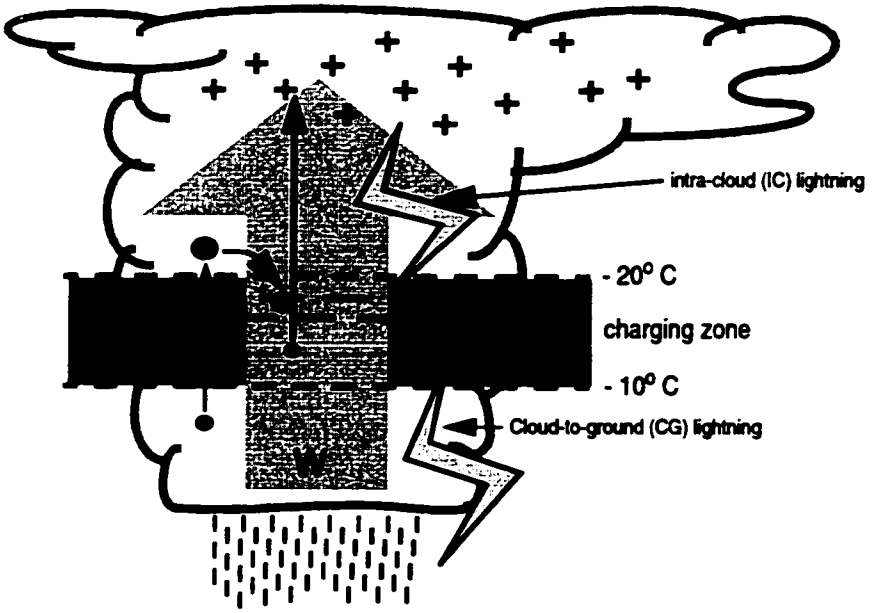

Figure 1.5: Schematic of the precipitation based thundercloud electrification process.

The Boys camera made it possible to characterize the various components that make up a lightning flash (see Fig 1.2). In CG flashes a low current ($\sim$ 1kAmp), low luminosity channel is initiated in the cloud. The leader propagates down towards the ground in discrete steps (3 - 50m long) separated by $\sim$ 50μsec pauses (Uman, 1987) and is thus commonly referred to as a *stepped leader*. The stepped leader is followed by a return stroke which propagates back up to the cloud. There may be several leader - return stroke pairs but the time between strokes is usually too short for our eyes to resolve and thus what we call a lightning flash usually consists of several individual strokes. The return stroke is the brightest phase of the flash with typical peak currents $\sim$ 40 kAmps. CG flashes typically lower $20-30$ coulombs to ground but values in excess of 200 coulombs have been recorded (Uman, 1987).

The initiation of the stepped leader phase, often referred to as preliminary breakdown, is still a subject of much debate. We discuss this topic in depth in Chapters 2 through 4.

1.4 Thesis Organization

As we have seen in the preceding sections electrification in convective clouds depends on collisions between ice particles. Thus lightning frequency is mainly a function of cloud updraft velocities and ice and water concentrations. These parameters are, in turn, influenced by initial environmental conditions such as Convective Available Potential Energy, cloud base forcing and cloud condensation nucleus concentration. It is also important to consider the role that ice and water particles may play in the lightning initiation process.

Therefore in this work we felt it was important to explore not only the basic physics of lightning initiation but also the extent to which other cloud properties may influence lightning frequency. This thesis thus has two areas of focus.

The first part focuses on our research addressing the subject of lightning initiation. In Chapter 2 we discuss the physics of the discharge process and review current hypotheses for lightning initiation. The relevant literature on this subject is very scattered, encompassing many different disciplines, each with their own set of technical jargon. We have thus tried to compile and unify the relevant information as it applies to the lightning initiation process. We follow this with results from our discharge model (Chapter 3) and with an evaluation of the feasibility of the various hypotheses (Chapter 4).

In the second part we turn our attention to thunderstorm cloud properties and how they relate to lightning flash rates (Chapter 5 - 7). We make use of a combination of a numerical thunderstorm model and observations to learn more about the physical processes occuring in thunderclouds. In addition, we consider the feasibility of using satellite lightning flash rate as a proxy for other hard to measure cloud properties.

Chapter 2

Lightning Initiation in Thunderclouds

The mechanism by which lightning initiation in thunderclouds occurs is poorly understood. The maximum measured electric fields in clouds are $E_{max} \sim$ 100 - 400 kV/m (Marshall *et al.*, 1995; Winn *et al.*, 1974) which are an order of magnitude smaller than the E-fields required for dielectric breakdown of air. The breakdown field is $\sim$ 2700 kV/m at surface pressure, dropping to $E_{breakdown} \sim$ 1600 kV/m at p=600mb.

The basic charge and E-field structures found in thunderclouds are shown in Fig 2.1. Field observations of lightning show that lightning initiates primarily in three regions - indicated in Fig 2.1 (Krehbiel, 1986; Shao and Krehbiel, 1996). In initiation regions [1] and [2] liquid and ice hydrometeors coexist while in region [3] all hydrometeors are in the ice phase.

In this Chapter we will discuss the physics of two independent hypotheses commonly forwarded as explanations for the discrepancy between E_{max} and $E_{breakdown}$. This will be followed in Chapter 3 by the results from our numerical model study into the feasibility of one of these hypotheses - the hydrometeor hypothesis. Much of the remainder of this Chapter, and Chapter 3, are taken from a previously published paper (Schroeder *et al.*, 1999). Finally, in Chapter 4, we wrap up this topic with a discussion of the implications that these hypotheses have for lightning initiation in thunderclouds.

Before proceeding any further with this Chapter we will introduce some terminology commonly used in this field. These brief definitions serve as an introduction to discharge phenomena. The physics of these phenomena will be discussed in more detail in the following sections.

- *discharge*: dielectric breakdown of a material (in our case air)
- *corona*: usually denotes the breakdown of air in the vicinity of an object (e.g. a metal spike, a raindrop, etc)
- *burst or current pulse*: a discharge that occurs intermittently

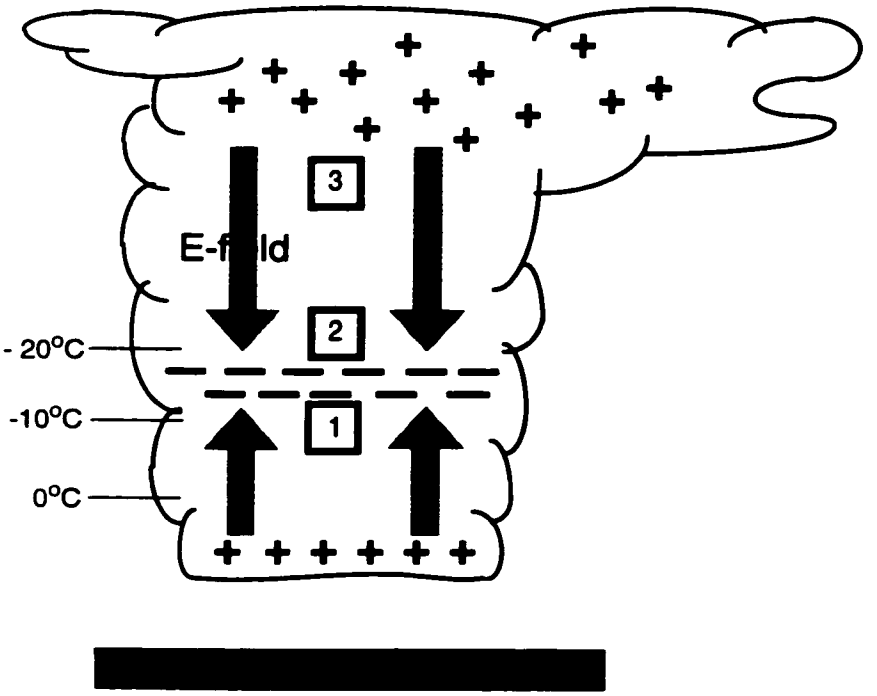

Figure 2.1: Schematic of thundercloud with typical charge and E-field structure. Lightning initiation regions are also indicated.

- *glow*: a continuous discharge that occurs in the close vicinity of an object and appears as a constant glow around the object

- *streamer*: a propagating discharge that appears as a bright, filamentary channel

- *plasma*: a gas consisting of ions, electrons, and neutral particles; the behavior of the gas is dominated by the electromagnetic interaction between the charged particles (Morris, 1996).

2.1 Hydrometeor Hypothesis

The traditional explanation for the E_{max} - $E_{breakdown}$ discrepancy is that E-field strengths in the vicinity of small hydrometeors are greatly intensified (either by drop break-up or distortion) and can reach $E_{breakdown}$ in a small volume local to the hydrometeor.

Macky (1931) investigated the distortion and break-up of water drops in strong electric fields and found that discharges could be initiated from falling water drops in uniform electric fields $\sim$ 800 kV/m. For the period following this discharges from drops were associated with drop break-up. In the 1950's and early 1960's, however, Loeb (1965) suggested that discharges could initiate from the surfaces of drops that were highly distorted by strong electric fields.

Dawson (1969) showed that both of these processes occurred and were in fact competing processes. A set of experiments for both positive and negative discharges from water drop surfaces showed that the transition from the surface-disruption mode to pure corona (distortion but no break-up) was pressure dependent. When positive and negative discharges were compared Dawson found that, for a given applied E-field, the transition from surface-disruption to pure corona always occurred at higher pressures in the positive discharge case.

Richards and Dawson (1971) followed this up with an experiment in which they more closely simulated the thundercloud environment. They studied drop instabilities and discharge initiation from water drops falling at their terminal velocities in a vertical E-field. Their results showed that for an uncharged 2mm drop E-fields in excess of 950 kV/m were necessary for drop instability and discharge initiation while for a highly charged 2mm drop the instability field was typically 550 kV/m.

Thus at this stage it was clear that the large scale applied E-fields necessary to initiate a discharge from water drops were still several times larger than the E-fields observed in thunderclouds.

Crabb and Latham (1974) showed that a pair of water drops, R=2.7mm and r=0.65mm colliding with a relative velocity of 5.8 m/s could initiate positive discharges at E-fields as low as 250 kV/m.

Griffiths and Latham (1974) also looked at ice particles as a source for discharge initiation. Again they found that, at the lower pressures where one expects to find ice particles in thunderstorms, the initiation E-fields were $\sim$ 250 - 400 kV/m.

Blyth *et al.* (1992) concluded that only two mechanisms appeared capable of initiating a dis-

charge in thundercloud conditions: warm colliding drops and individual ice particles.

More recent work by Coquillat and Chauzy (1994) and Georgis *et al.* (1995) used theoretical calculations to investigate discharge initiation from single raindrops and two closely spaced dropped respectively. The Coquillat and Chauzy (1994) study, however, required unrealistically high charges on the drops in order to achieve initiation E-fields comparable to those observed by Crabb and Latham (1974). Similarly Georgis *et al.* (1995) were unsure that the drop configurations required to initiate discharge in low E-fields were physically realisable. A computational study by Cooray *et al.* (1998) considered the possibility of a large number of rain drops interacting with each other such that the E-field at one end of the "chain" of drops was enhanced to $E > E_{breakdown}$. They concluded, however, that chains of 10 or more drops would be necessary when the applied E-field was 600 kV/m. For lower applied fields the number of drops required is increased. It seems unlikely that this would provide an effective mechanism for in-cloud discharge initiation.

It would appear then that the Blyth *et al.* (1992) conclusions still stand and that, if hydrometeors are to be considered the source of discharges in thunderclouds, the experimental work of Crabb and Latham (1974) and Griffiths and Latham (1974) offer the best insight.

In order to understand how the E-field enhancement around hydrometeors can lead to the initiation of streamers we must understand more about the discharge process itself.

2.2 The Discharge Process

Discharge physics is a broad and very diverse subject with applications in a wide variety of disciplines. Much of the work relates directly to applications in electrical engineering with a somewhat smaller body of work dedicated to processes occuring in thunderclouds. It is impossible to cover the subject comprehensively within the scope of this thesis. We will, therefore, focus on models of the discharge process that are specifically applicable to discharges that take place in thunderclouds.

2.2.1 Review

Dawson and Winn (1965) presented an early electrostatic model of creation and propagation of a streamer in the non-uniform E-field surrounding a positively charged point electrode in air. In their model electrons move toward the electrode, ionizing air molecules and creating positive space

charge that is highly localized in a spherical head in front of the original electrode, enhancing the E-field there. The enhanced E-field serves to produce new free electrons via photoionization and to accelerate these electrons towards the spherical head. The final propagation length was determined by an assumption about the rate of energy loss during the process. Their results, which were generally supported by laboratory experiments, suggested that once created, a streamer head containing approximately 10^8 positive ions can propagate several centimeters with no external field before it loses most of its energy through ionization.

A more comprehensive study of positive and negative streamer evolution was carried out by Gallimberti (1972, 1979) and his colleagues Bondiou and Gallimberti (1994) in a set of theoretical and experimental investigations of spark formation in long gaps. They defined two stages in the evolution of the discharge. The first *cold* stage in positive discharge is that described above by Dawson and Winn (1965) and Griffiths and Phelps (1976b). The second, *warm* stage is referred to as a leader (see section 2.2.3). This model has been applied successfully to observations of triggered lightning from small rockets but not to natural lightning initiation.

2.2.2 *Positive discharge types*

Here we describe several positive discharge initiation processes that can occur at the surfaces of hydrometeors in the presence of strong E-fields. We focus only on positive discharges as they have a lower initiation threshold, have been studied more extensively than negative discharges in laboratory experiments and are simpler to model.

Negative discharges have a much more complex structure than positive discharges. The negative streamer can also be modeled as a negative streamer head that moves through the enhanced E-field. An important difference between negative and positive discharges, however, is that the next generation of avalanches move away from the streamer head rather than towards it as in the positive case. Castellani *et al.* (1994) provide a detailed model of the negative discharge process.

The positive discharge process can be separated into the *surface disruption* discharge type and *pure* discharge types.

The first process, *surface disruption* discharge, occurs when the electrostatic repulsive force on a drop in a strong E-field exceeds the drop's surface tension. This results in the break-up of the

drop, and an associated discharge. In a series of laboratory experiments Dawson (1969) investigated the transition from surface disruption discharge to pure corona discharge (no drop disruption) as a function of drop size and pressure. He found that the surface E-field necessary for disruption was independent of pressure. From Dawson (1969) one can obtain the surface E-field, $E_{disruption}$, required for surface disruption discharge as a function of drop size for both positive and negative discharges.

The other processes are often referred to as *pure* discharge processes because the discharge initiates without the occurrence of drop surface disruption. In a strongly non-uniform E-field the *pure* discharge process progresses as follows:

1. *burst or current pulse* discharges, which occur intermittently

2. *constant glow*, continuous current, and

3. *streamers*, which are capable of propagating away from the electrode.

The E-field required for initiation of each of these stages is higher than for the proceeding one.

All of these processes result in the deposition of charge on the hydrometeors; the charge can be either positive or negative depending on the sign of the applied E-field.

2.2.3 Leaders

Under favorable conditions, the electron current in the streamer channel becomes strong enough that Joule heating produces a *warm* leader; a channel in which thermodynamic equilibrium is destroyed and hydrodynamic effects become important. This is commonly referred to as a leader or a *stepped-leader* in the cloud-to-ground lightning context.

The transition from streamer to leader occurs when the temperature in the streamer channel exceeds a critical temperature, above which thermal detachment of negative ions occurs and there is a large increase in electron density. Bondiou and Gallimberti (1994) calculate the critical temperature for the transition of a streamer with radius $R = 35$ μm, at an initial temperature of $T = 300$ K, to be $T_c = 1500$ K. This T_c will be reached when the linear charge density within the streamer channel reaches $\approx 10^{-4}$ C/m [Bondiou (1997)].

The leader channel that forms is a weakly ionized plasma channel. Bondiou and Gallimberti (1994) calculate the E-field and voltage drop along the leader channel. They also discuss leader propagation. A schematic for leader propagation is shown in Fig 2.2. The leader is sustained by streamers which converge on the leader tip. The current collected by the leader from each of these streamers determines the energy input into the leader. The advancing leader tip, in return, maintains the high E-field that enables the streamers to initiate ahead of the leader.

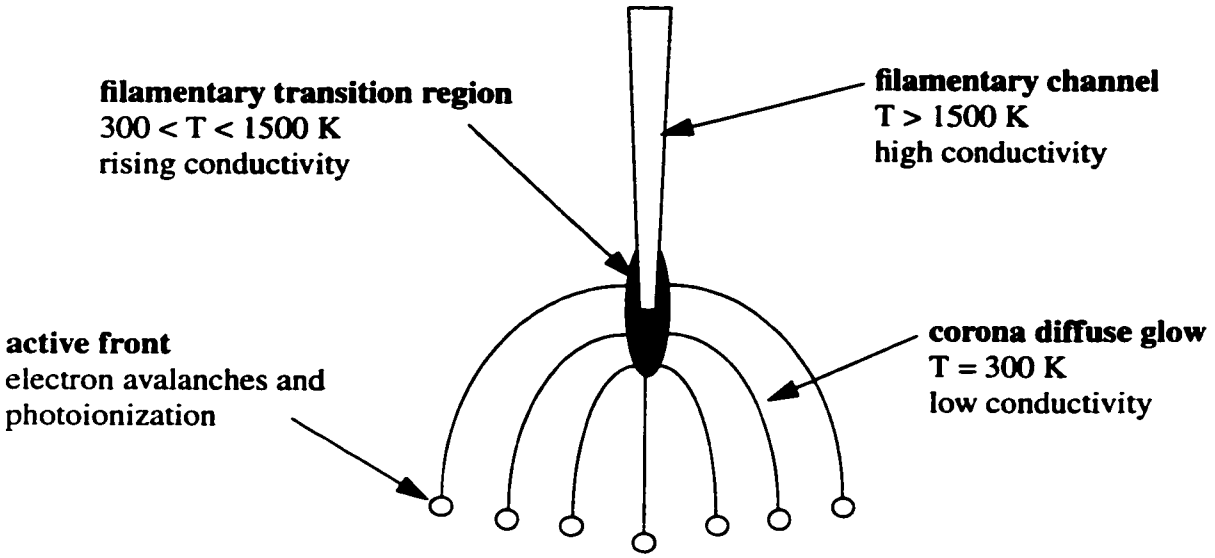

Figure 2.2: Schematic of leader propagation. Adapted from Bondiou and Gallimberti (1994).

2.2.4 Modeling the discharge process

Following the earlier work of Dawson and Winn (1965); Gallimberti (1979) and Bondiou and Gallimberti (1994) we model the positive discharge as a series of electron avalanches.

Consider the E-field near the surface of a drop which is situated in an external E-field, $E_{external}$ (Fig 2.3). Initially, the total E-field at a point a distance r from the drop surface is

$$E(r) = E_g(r) = E_{external} + E_{drop}(r) \tag{2.1}$$

where E_{drop} is the contribution due to charge induced on the drop and $E_g(r)$ is referred to as the geometric E-field.

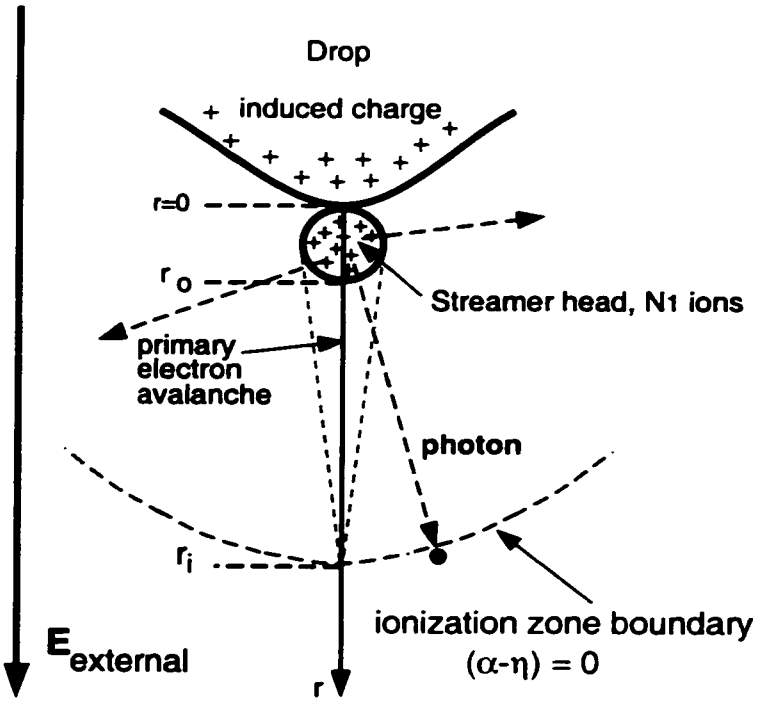

Figure 2.3: Schematic of positive discharge formation near the surface of a drop. Free electrons created by photoionization are accelerated by the E-field and undergo collisions with air molecules. The ionization of molecules within the ionization zone leads to an exponential growth of electrons (avalanche) and the formation of a spherical streamer head. In the above representation a 1-D approximation has been applied, with the electron avalanche occurring along the r-axis.

Free electrons are created in the atmosphere via photoionization induced by cosmic rays and natural radiation (electron production rate $\sim 10^{-7}$ $m^{-3}.s^{-1}$) and by the collisional detachment of negative oxygen ions. In the presence of E, these free electrons are accelerated and undergo collisions with air molecules. At some radial distance from the drop E is such that:

$$\alpha(E/p) = \eta(E/p) \tag{2.2}$$

where α [m^{-1}] and η [m^{-1}] are the ionization and attachment coefficients for electrons in air, respectively, and p is the total air pressure. The surface defined by Eqn (2.2) is the *ionization zone boundary* - inside this boundary $\alpha > \eta$ and there is a net growth of free electrons. At surface pres-

sure the ionization zone boundary is the surface along which $E \sim 2700$ kV/m. The ionization and attachment coefficients are strongly dependent on the ratio of E-field strength to pressure. Figure 2.4 shows α and η as functions of E/p (Harrison and Geballe, 1953; Loeb, 1965; Badaloni and Gallimberti, 1972; Ibrahim and Singer, 1982).

In order to simplify the problem, it is common to replace the three-dimensional problem by a one-dimensional one in which all avalanches occur along the r-axis (Dawson and Winn, 1965; Griffiths and Phelps, 1976b; Gallimberti, 1979). The point r_i marks the intersection of the ionization zone boundary with the r-axis. When a free electron, starting at r_i, accelerates in the E-field towards the drop, the number of electrons grows exponentially with decreasing r. This is referred to as the *primary electron avalanche*. Due to the exponential nature of the growth, most of the ionizing collisions occur near the surface of the drop. The free electrons are then absorbed by the drop, leaving behind a region of low mobility positive ions, modeled as a sphere (Dawson and Winn, 1965; Gallimberti, 1979), and referred to as the *streamer head*.

The number of positive ions formed by the primary avalanche traveling from the ionization zone boundary, r_i, to the drop surface, $r = 0$, is given by:

$$N_1 = \exp\left[\int_{r_i}^{o} (\alpha(r)) - \eta(r))dr\right] \tag{2.3}$$

The radius of the streamer head is approximately:

$$R_s = \left[6\int_{r_i}^{o}\left(\frac{D(r)}{v(r)}dr\right)\right]^{\frac{1}{2}} \tag{2.4}$$

where D and v are the electron diffusivity and drift velocity, respectively. D and v are also functions of the ratio (E/p) and thus depend on r (Healey and Reed, 1941; Ibrahim and Singer, 1982).

The total electric field at r is now given by:

$$E(r) = E_g(r) + \frac{eN_1}{4\pi\varepsilon_0(r - R_s)^2} \tag{2.5}$$

where the second term is E_{sphere}, the E-field due to the spherical charge concentration of the streamer head.

In addition to ionization, collisions between the free electrons and air molecules also result in the excitation of the molecules, which then emit photons on decay. A certain fraction of these photons in

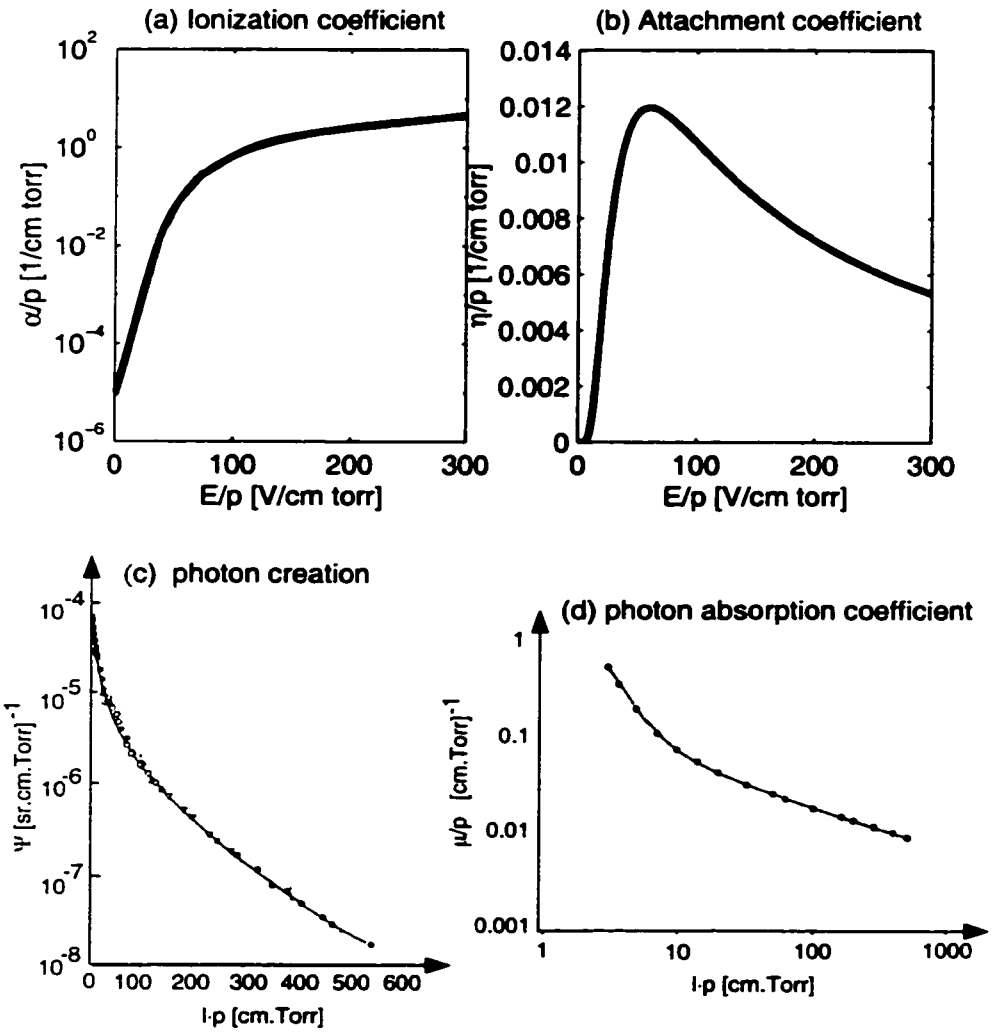

Figure 2.4: (a) Ratio of ionization coefficient to pressure, α/p, for electrons in air Badaloni and Gallimberti (1972); Loeb (1965) (b) Ratio of attachment coefficient to pressure, η/p, for electrons in air Badaloni and Gallimberti (1972); Harrison and Geballe (1953) (c) $\Psi = f_1 \cdot f_2 \cdot \theta$ where f_1 is the number of photons created per ionizing collision, f_2 [m^{-1}] is the number of photoions created per photon per meter and θ is a solid angle = 2π in our calculations Penney and Hummert (1970) (d) Ratio of photon absorption coefficient to pressure, μ/p, in air Penney and Hummert (1970).

turn have sufficient energy to ionize molecules that they encounter, creating *photoelectrons*. These photoelectrons then start a series of *secondary avalanches* which converge on the drop from all directions.

The number of photoelectrons created per meter at a radial distance, l, from the drop surface is given by:

$$P(l) = f_1 N_1 \cdot e^{-\mu l} \cdot f_2 \cdot G \tag{2.6}$$

where f_1 is the number of photons created per ionizing collision

μ [m^{-1}] is the photon absorption coefficient in air

f_2 [m^{-1}] is the number of photoions created per photon per meter

G is a geometric factor to account for the fact that some photons are absorbed by the drop.

Both μ and $(f_1 \cdot f_2)$ are functions of $(l \cdot p)$, the product of the distance from the photon source (the collisions) and air pressure (Penney and Hummert, 1970) - see Fig 2.4.

If one again compresses all activity onto the r-axis, the total number of ions created in the secondary avalanches is given by:

$$N_2 = \int_{r_i}^{r_o} P(l) \cdot \exp\left[\int_{l}^{r_o} (\alpha - \eta)\, dr\right] dl \tag{2.7}$$

where r_o indicates the position of the primary streamer head surface.

We now consider the various initiation conditions. A *burst pulse discharge* is initiated if the number of photoelectrons created along the ionization zone boundary during the growth of the primary avalanche is equivalent to the number of photoelectrons that started the primary avalanche (commonly taken to be one) (Abdel-Salam *et al.*, 1976).

We consider photoelectron production in a region of depth $(1/\mu)$ along the ionization zone boundary and write the above condition as follows:

$$\frac{P(r_i)}{\mu(r_i)} = 1 \tag{2.8}$$

This type of discharge is intermittent since the charge in the primary streamer head is too low to alter the E-field significantly and is thus unable to attract the subsequent avalanches to its surface. Instead, the successor avalanches are directed towards the drop surface - allowing the discharge to

"spread" over the drop surface - and there is no propagation away from the drop. At the minimum inception E-field, this discharge will be intermittent but if the E-field is increased sufficiently a constant glow will be established, though there will still be no propagation away from the drop.

A more stringent initiation condition exists for streamers. In this case the number of positive ions in the primary streamer head must be large enough to attract the secondary avalanches to the streamer head surface. This is achieved when the radial E-field around the streamer head, $E_{sphere} = \frac{eN_1}{4\pi\varepsilon_0(r-R_s)^2} \sim E_g$ (Abdel-Salam *et al.*, 1976). In addition, in order for this process to be completed:

(a) N_2, the number of positive ions in the streamer head that results from the secondary avalanches, must equal N_1, the number of positive ions created by the primary avalanche, and

(b) the radius of the secondary streamer head must equal R_s, the radius of the primary streamer head Dawson and Winn (1965).

These conditions ensure that the initial streamer head charge density is reproduced in the second streamer head. Continued reproduction of the streamer head in subsequent steps results in propagation of the positive streamer away from the drop surface. The distance that the streamer will propagate depends on the magnitude of the applied E-field.

The minimum value of $E_{external}$ necessary to initiate a discharge at pressure p is referred to as $E_{initiation}(p)$ and depends on the type of discharge (*burst pulse* or *continuous streamer*).

2.3 Runaway Electron Breakdown Hypothesis

Wilson (1924) suggested that electrons produced by cosmic ray particles could be accelerated over large distances by the E-fields in thunderstorms. Cosmic rays consist of nuclei and electrons arriving at the earth from outer space. The cosmic nuclei go through a number of interactions with atmospheric nuclei, producing several different kinds of secondary particles, including high energy electrons (see schematic, Fig 2.5). Cosmic ray showers (CRS) - also referred to as extensive air showers - occur less frequently, when ultra high energy cosmic nuclei collide with atmospheric nuclei, producing a large number of secondary particles and thus a more intensive flux of secondary electrons.

To understand the possible connection between these high energy secondary electrons and light-

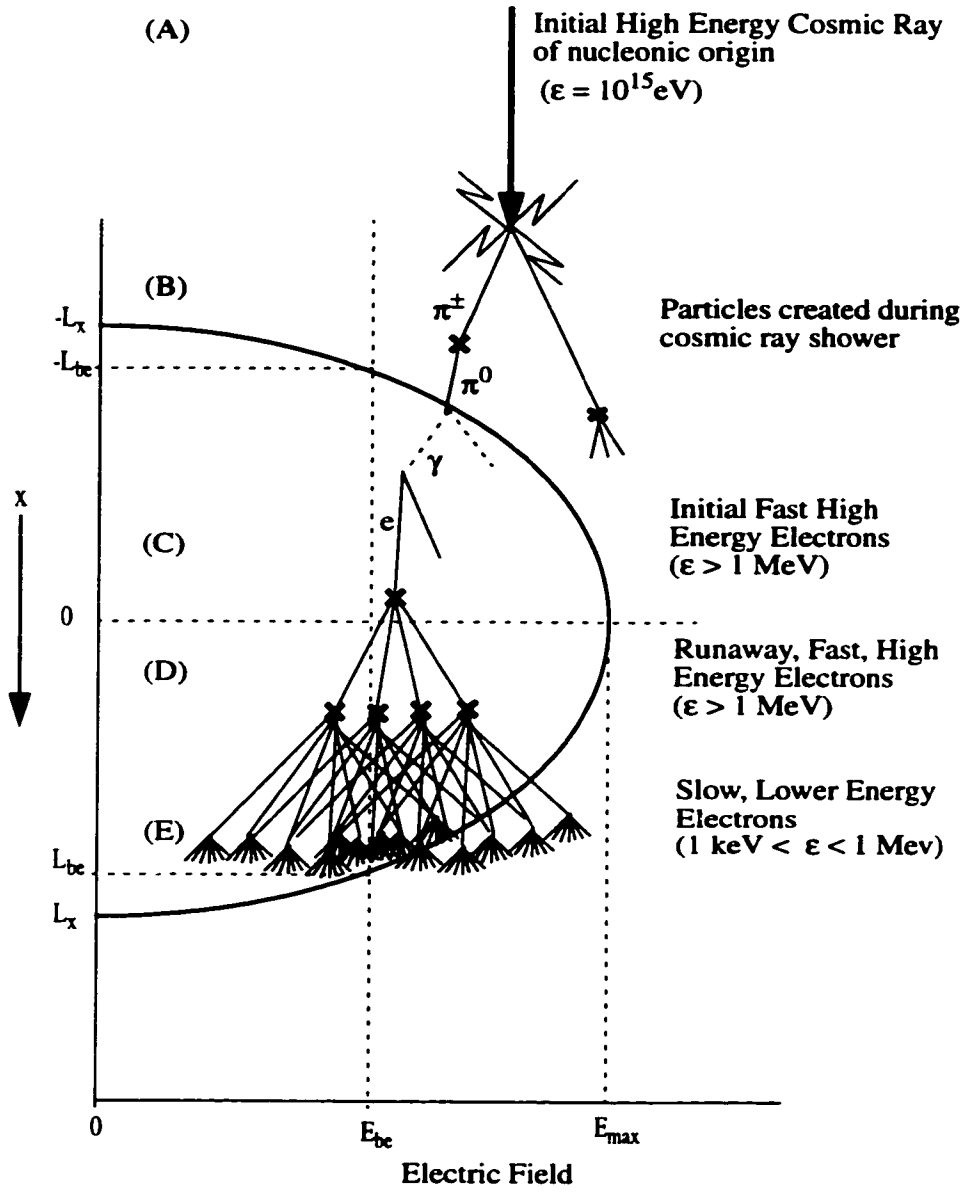

Figure 2.5: Schematic of interactions between an incoming cosmic ray of nucleonic origin and atmospheric nuclei. The subsequent growth of electrons in the thunderstorm E-field is also shown. The origin of the x-axis is located at the altitude of the maximum E-field. $\pm L_{be}$ indicate the x-values where $E = E_{be}$, the minimum E-field needed to produce the runaway breakdown effect.

ning initiation we must consider the dynamics of electrons moving in E-fields. For an electron at altitude z with kinetic energy $K(z)$ moving in the z direction in an electric field $E(z)$ (positive downward),

$$\frac{dK}{dz} = eE(z) - F(K,z) \tag{2.9}$$

where the energy loss due to collisions with air molecules produces an effective dynamical frictional force $F(K,z)$, proportional to the local air density, that decreases with increasing K for $K < 1$ MeV (see Fig 2.6). However, at an energy of approximately 1 MeV the force begins to increase with increasing energy. Thus electrons with kinetic energy K such that $eE(z) \geq F(K,z)$ gain kinetic energy at an ever increasing rate, even while losing energy via ionization and excitation of molecules in the medium. Such electrons are termed *runaways*.

The minimum value of the dynamical frictional force is given by:

$$F_{min} = \left(\frac{1}{4\pi\varepsilon_o}\right)^2 \frac{4\pi Z e^4 N_m}{mc^2}\, a \tag{2.10}$$

where N_m is the molecular density of the air [m^{-3}]

$Z = 14.5$ is the mean molecular charge of air

m = electron mass

$a \approx 11$ is a non-dimensional parameter representing a relativistic correction (Roussel-Dupre *et al.*, 1993).

We can then define a *breakeven* E-field strength $E_{be}(p)$ such that for fields $E \geq E_{be}(p)$, electrons of 1 MeV neither gain nor lose energy as they move and create new lower energy electrons (Gurevich *et al.*, 1992).

The *breakeven* E-field [V/m] for runaway behavior is then derived from Eqn (2.10):

$$\begin{aligned} E_{be} &= \frac{F_{min}}{e} \\ &= \left(\frac{1}{4\pi\varepsilon_o}\right)^2 \frac{4\pi N_m Z e^3 a}{mc^2} \end{aligned} \tag{2.11}$$

This can be approximated by:

$$E_{be} \approx 200\, p \tag{2.12}$$

of these fast electrons. More recent studies by Parks *et al.* (1981) and McCarthy and Parks (1985), making use of x-ray spectrometers aboard aircraft in the vicinity of thunderstorms, clearly show sharp increases in the X-ray flux prior to lightning strikes.

Gurevich *et al.* (1999) propose a mechanism by which the in-cloud E-field can be enhanced to large scale breakdown values ($E \sim$ 1600 kV/m at p = 600 mbar) by these fast electrons. The hypothesis requires a combination of the cosmic ray shower and runaway electron avalanche processes mentioned above. The large number of fast and slow electrons produced during the runaway electron avalanche leads to the establishment of a plasma region. Here the electron density is large enough that the plasma becomes strongly polarized, decreasing the electric field inside the plasma and increasing the electric field at either end of the plasma region.

We will now present the background physics of the various aspects of this hypothesis. The relevance of this process as a mechanism for lightning initiation is discussed in detail, and compared to the hydrometeor hypothesis, in Chapter 4.

2.3.1 Cosmic ray showers

The Gurevich *et al.* (1999) hypothesis begins with a cosmic ray shower. The flux [#/km^2/s] of cosmic ray showers depends on the assumed cosmic ray particle energy, ε_o. Estimates of electronic cosmic ray particle fluxes are shown in Table 2.1 for the ε_o of interest here. At these high energies the flux is independent of latitude, unlike the flux of lower energy cosmic rays.

Table 2.1: Cosmic ray shower flux as a function of cosmic ray particle energy from Gurevich *et al.* (1999).

ε_o [eV]	10^{13}	10^{14}	10^{15}	10^{16}
F [km^{-2}.s^{-1}]	4000	100	2	0.02

2.3.2 *Production of fast electrons by CRS*

The number of fast electrons with $\varepsilon > 1$ MeV produced by each electronic cosmic ray particle with energy ε_o is given in Gurevich *et al.* (1999) as:

$$n_o = \frac{0.3\varepsilon_o}{\beta\sqrt{\ln(\frac{\varepsilon_o}{\beta})}} \tag{2.13}$$

where $\beta \approx 72$MeV for air.

The density of these fast electrons in the plane orthogonal to the axis of propagation is given by the NKG (Nishimura, Ksimata, Greizen) empirical formula, which is valid for electronic cosmic rays. For altitudes between 3 and 10 km the NKG formula yields:

$$\rho_e \approx 0.4 \frac{n_o}{R^2} \left(\frac{R}{r}\right) \frac{1}{\left(1+\frac{r}{R}\right)^{3.5}} \tag{2.14}$$

where r is the radial distance from the axis, and

R is the characteristic scale of cosmic ray showers $\sim$ 100m.

The radial density distribution of nuclear cosmic ray electron secondaries will be slightly different (there is more radial diffusion - see Fig 2.5) and use of this empirical formula will lead to a slight overestimate of the electron density on the axis. However, using an average radial value rather than the axial value gives a reasonable approximation of the electron density.

2.3.3 *Thunderstorm electric fields*

We now consider the E-fields in thunderstorms. Vertical E-field profiles show that there are typically one or more maxima in the E-field. We will examine the propagation of electrons near such a maximum. Let this maximum value be E_m, located at $x = 0$ (see Fig 2.5). Then the E-field in the vicinity of E_{max} can be approximated, as a function of x, by:

$$E = E_{max}\left(1 - \left(\frac{x}{L_x}\right)^2\right) \tag{2.15}$$

where x is directed downwards, and

L_x is a characteristic depth scale of the E-field

The height over which $E(x)$ exceeds E_{be} is:

$$L_{be} = L_x \sqrt{1 - \frac{E_{be}}{E_{max}}} \tag{2.16}$$

Within the region $-L_{be} < x < L_{be}$, where $E > E_{be}$, we can rewrite the E-field as:

$$E = E_{be} + E_o \left(1 - \frac{x^2}{L_{be}^2}\right) \tag{2.17}$$

where $E_o = (E_{max} - E_{be})$. We then make the following transformation:

$$E' \equiv E - E_{be} = E_o \left(1 - \frac{x^2}{L_{be}^2}\right) \tag{2.18}$$

2.3.4 Growth of the fast electron population

Within the $E > E_{be}$ region the fast electrons grow exponentially in number such that their number is given by:

$$n_{fe}(x) = n_{fe}(-L_x) \exp\left[\int_{-L_x}^{x} \lambda_i \, dx\right] \tag{2.19}$$

where λ_i is the average ionization length.

The electrons in this growing population spread out perpendicular to the x-axis with a diffusion coefficient, D, determined by both the production of new fast electrons and the scattering of those already present. Gurevich *et al.* (1999) give the diffusion coefficient as:

$$D = 0.03\, c^2\, t_b + \frac{v^2}{3\nu} \tag{2.20}$$

where $v \approx c$, t_b is the time for an electron to be accelerated to a velocity of v ≈ c by the E-field, and ν is the collisional frequency of runaway electrons with air molecule nuclei. If we assume the initial velocity of the electron is small compared to the speed of light, c, then $v_{final} \approx c \approx a t_b$ or:

$$t_b = \left(\frac{c}{F_{min}/m}\right) = \frac{mc}{eE_{be}} \tag{2.21}$$

$$\nu = \frac{eE_{be}Z\varphi^2}{16mc} = \frac{Z\varphi^2}{16t_b} \tag{2.22}$$

where $0.5 < \varphi < 0.7$ is a shielding factor. This then leads to a simplification of Eqn (2.20):

$$\begin{aligned} D &= c^2 t_b \left[0.03 + \frac{16}{3Z\varphi^2}\right] \\ &\approx c^2 t_b \end{aligned} \tag{2.23}$$

The density of the beam of fast electrons, N_{fe}, in the runaway beam is described by the following equation:

$$\frac{\partial N_{fe}}{\partial t} + \frac{\partial}{\partial x}(v_x N_{fe}) = D\frac{\partial^2 N_{fe}}{\partial r_\perp^2} + \frac{N_{fe}}{\tau_i} \tag{2.24}$$

where $r_\perp$ is the direction perpendicular to x-axis and the drift velocity is:

$$v_x \approx \frac{eE'}{3\nu m} \equiv v_o \frac{E'}{E_{be}} \tag{2.25}$$

For our purposes we use $v_o \approx c$. Using Eqn (2.24) and taking into account the source of fast electrons created by the cosmic ray particles (Eqn 2.13, Gurevich *et al.* (1999)) found that the density of fast electrons (1 keV $< \varepsilon_o <$ 1 MeV) was:

$$\begin{aligned} N_{fe} &= 1.5\,\frac{\rho_e R^2}{\kappa L_o}\, e^{\Lambda_i} \\ \text{where}\quad \kappa &= 2Dt \qquad \sqrt{\kappa} < r \ll R \end{aligned} \tag{2.26}$$

and

$$\Lambda_i = \frac{1}{\tau_i c}\left(x - L_{be}\frac{1+\frac{x}{L_{be}} - (1-\frac{x}{L_{be}})e^{\frac{t}{\tau}}}{1+\frac{x}{L_{be}} + (1-\frac{x}{L_{be}})e^{\frac{t}{\tau}}}\right) \tag{2.27}$$

The quantity τ approximates the time needed for an electron to go from $x = 0$ to $x = L_{be}$ in the E-field and is given by:

$$\tau = \frac{E_{be}L_{be}}{2E_o v_o} \tag{2.28}$$

The average ionization length:

$$\lambda_i = \frac{2amc^2}{eE_{be}} u_{so} \tag{2.29}$$

is derived in Gurevich *et al.* (1992). Here u_{so} represents the dimensionless quantity $u = \frac{v^2}{c^2}$ at an electron trajectory angle $\mu = \cos\theta = 0$. Then the average time between ionization events is given by:

$$\tau_i = \frac{\lambda_i}{c} \tag{2.30}$$

2.3.5 *Production of slow electrons*

In addition to the fast electrons produced under runaway conditions, a large population of slow electrons are also produced. The density of this population will be higher than that of the fast electrons. Gurevich *et al.* (1999) find that at a time $t > \tau$ the maximum electron density of slow electrons can be found near $x = L_{be}$ (i.e. at the bottom of the runaway region) and is given by:

$$\begin{aligned} N_{se}^{max} &= N_{fe}\frac{\tau_{io}v_o}{\lambda_s} \\ &= 1.5\frac{\lambda_i}{\lambda_s}\frac{R^2}{\kappa L_o}e^{\lambda_i}\rho_e \end{aligned} \tag{2.31}$$

where the ionization length for slow electrons, $\lambda_s \approx 6 \times 10^{-6}$m, and

$$\tau_{io} = \frac{E'}{E_{be}}\tau_i \tag{2.32}$$

Gurevich *et al.* (1999) show that for $\varepsilon_o \geq 10^{15}$eV maximum electron growth, achieved near the bottom of the runaway region, gives $N_{se}^{max} \sim 10^{14} - 10^{15}$ m^{-3}.

2.3.6 *Development of high local electric fields in the avalanche*

In principle, there are two regimes possible within the runaway electron avalanche. In the first regime the density of slow electrons and the conductivity (σ) are both relatively low. In this regime the attachment time ($\frac{1}{\nu_a}$) is small compared to the relaxation time for polarization ($\tau_D = \frac{\varepsilon_o}{\sigma}$).

If the conductivity becomes high enough in a small region and τ_D exceeds the attachment time, a plasma forms. In the absence of currents the electric field within this plasma region is zero while the electric field just outside the region becomes very intense. The boundary of the plasma region is defined by the condition $\tau_D = \frac{1}{\nu_a}$.

The conductivity depends on the number density of electrons and under typical conditions $N_e \approx 10^{14}$ m$^{-3} = N_{crit}$ is the critical density required such that $\tau_D > \frac{1}{\nu_a}$. Thus if $N_{se}^{max} \sim 10^{14} - 10^{15}$ m^{-3} at the bottom of the runaway region then N_{crit} is achieved and a plasma region will form. Gurevich *et al.* (1999) calculate that the E-field enhancement outside the plasma region can exceed $E_{breakdown}(p)$ and thus lead to the initiation of a streamer.

We discuss the requirement that this mechanism places on the electric fields needed for lightning initiation in Chapter 4.

Chapter 3

Hydrometeor Discharge Model Results

In this chapter we present the results obtained from our hydrometeor discharge model for both coalesced water drops and ice particles. The discharge model was initiated using conditions taken from the laboratory experiments of Crabb and Latham (1974) and Griffiths and Latham (1974) which are described below.

3.1 Observations

Crabb and Latham (1974) and Griffiths and Latham (1974) (hereafter CL and GL, respectively) obtained very promising results in a set of laboratory experiments in which they measured the E-fields required to initiate a discharge from:

1. the surface of filamentary, coalesced drops created when two water drops collided, and

2. the surfaces of ice particles, respectively.

They observed pulsed, intermittent discharges in a localized region near the surface of the hydrometeors and found that the E-fields for discharge initiation required lay within the range of observed thunderstorm E-fields.

3.1.1 Coalesced drops

Figure 3.1 (a) shows a schematic of the CL experiment - the full details of which can be found in CL. Their chamber, held at surface pressure, had a positive, high voltage upper plate and a grounded lower plate separated by 50mm. Voltages of up to 30 kV could be applied - corresponding to a maximum uniform E-field of 600 kV/m within the chamber. Large water drops (R=2.7mm) were dropped into the chamber and collided with small drops (r=0.65mm) which were ejected vertically

upwards from a small wind tunnel, simulating drops moving in updrafts in thunderclouds. A variety of coalesced drop shapes were observed, depending on the nature of the collision. CL described three basic collision modes: head-on, glancing and intermediate. Glancing and intermediate collisions produced a coalesced drop with a long filament extending from the large drop - see Fig 3.1 (b). Head-on collisions resulted in a flattening of the large drop and did not produce these long filaments. The drops remained in the coalesced state for $\sim$ 1 ms.

In CL's setup, a negative charge was induced on the upper surface of the drop while the lower end had a positive induced charge. In the thundercloud setting these drops would be located above the negative charge center of the cloud. CL recorded the size and shape of the coalesced drops as well as the applied E-fields required to initiate discharges for a large number of coalesced drops. They observed discharges from both ends of the drop but focussed on the positive pulses occurring at the lower surface of the drop. This surface was observed to remain intact. In contrast surface disruption was observed at the upper, negative surface of the drop. CL observed that positive burst pulses occured for values of E between 250 and 500 kV/m, depending on the length of the coalesced drop.

3.1.2 Ice

The GL setup was slightly simpler. Again the chamber contained two electrodes separated by up to 60mm to which voltages of up to 30kV could be applied. The temperature in the chamber was maintained at -12^{o}C and the pressure could be varied between 100 and 1000 mbar. The ice sample was suspended in the center of the chamber on a quartz fiber, diameter 100 μm. The E-field was increased slowly until a burst pulse discharge was initiated. The E-field of initiation was then noted.

GL made their measurements at a temperature of $T = -12^oC$ after observing that for $T \leq -18 \pm 1^oC$ they were unable to produce discharges. The electrical conductivity of ice, σ, is a combination of surface conductivity, σ_s, and bulk conductivity, σ_b. For thin ice crystals, such as needles and prisms, σ dominates and the majority of the current is carried on the surface. As temperature is lowered, σ decreases until at $\sim -18^oC$ it drops below a critical value, resulting in the suppression of discharges.

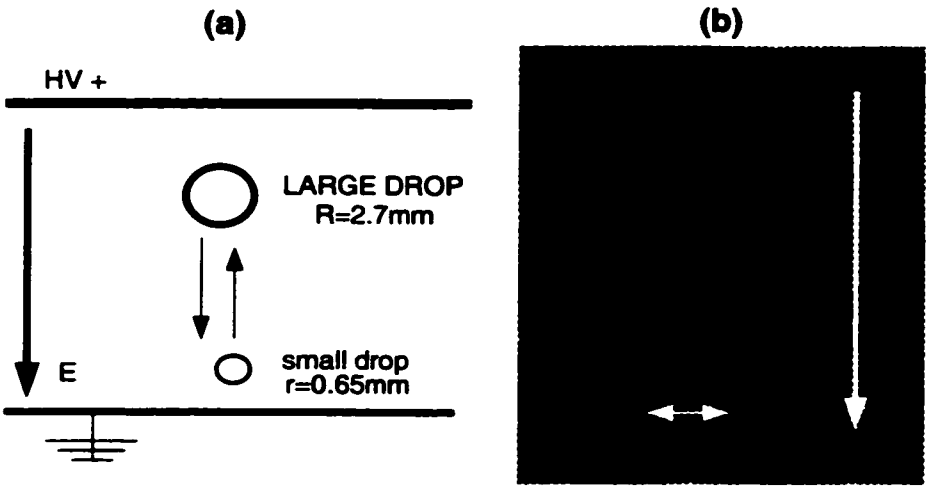

Figure 3.1: (a) Schematic of Crabb & Latham's experimental setup in which two drops (R = 2.7 mm and r = 0.65 mm) collided in the presence of an applied electric field. (b) Photograph of the coalesced drop that formed after the collision (Crabb and Latham, 1974).

3.2 Hydrometeor Discharge Model

We developed two hydrometeor models - one for colliding drops and one for ice particles. We used CL and GL's laboratory conditions, respectively, to initialize a discharge model based on 2.2.4. For the colliding drops we focussed only on the glancing collisions which produced long, filamentary coalesced drops. In the case of the ice particles we were limited due to the geometric constraints of our model (axial symmetry) to considering only the needle shaped ice crystals examined by GL. We varied both the microphysical and environmental conditions to simulate the range of conditions applicable to those found in thunderclouds. Much of the work presented in this Chapter was published in Schroeder *et al.* (1999).

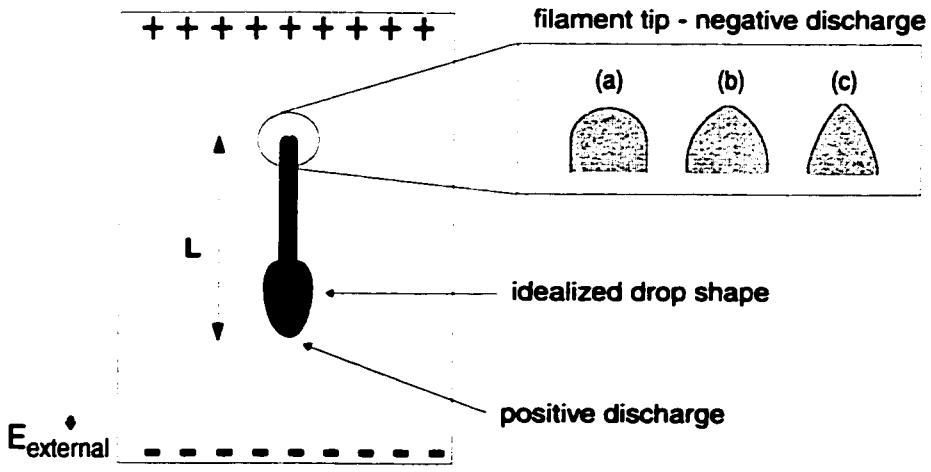

Figure 3.2: Schematic of our idealized coalesced drop shape. The size of the drop is characterized by its total length, L, as indicated. Three different shapes were considered for the upper filament tip and are indicated in the inset (a-c). Negative discharge occured at the upper filament tip with positive discharge occuring at the lower end of the drop. The E-field distribution around the the drop was calculated using a finite element method (Quickfield, 1996).

3.2.1 Procedure

Specifically, our results were obtained using the following procedure. We began by defining the hydrometeor shape and permittivity, ε. The idealized shapes that were used are shown in Fig 3.2 and Fig 3.3. We set the air pressure, p, and applied an E-field $E_{external}$ to the hydrometeor. The E-field distribution around the hydrometeor was calculated using a finite element method based solving routine (Quickfield, 1996). For the coalesced drops, the E-field at the drop's negative surface was then compared to the known surface disruption E-field threshold, $E_{disruption}$ (Dawson, 1969). If $E_{surface} > E_{disruption}$ then various amounts of positive charge, Q_{drop}, were added to the drop. The E-field distribution was recalculated (Quickfield, 1996) and the position of the ionization zone boundary, z_i, was determined. N_1 and R_1 were computed from Eqns (2.3) and (2.4) respectively, and $P(l)$ at z_i from Eqn (2.6). If $\frac{P(z_i)}{\mu(z_i)} = 1$, then $E_{external} = E_{initiation}(p)$ for burst pulse discharges. We then proceeded to calculate N_2 and R_2 from Eqns (2.7) and (2.4) respectively. If $E_c \sim E_g, N_2 = N_1$ and $R_2 = R_1$, then $E_{external} = E_{intiation}(p)$ for streamers. The procedure for the ice particles excludes the

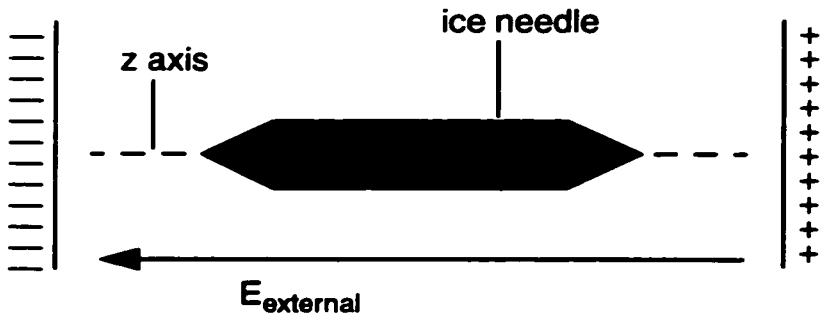

Figure 3.3: Schematic of our idealized modeled ice needle.

surface disruption steps, skipping directly to the determination of the ionization boundary location, z_i, and the first streamer head characteristics, N_1 and R_1.

3.3 Results for Coalesced Drops

3.3.1 Surface disruption

Dawson (1969) found $E_{disruption}$ = 8500 kV/m for a drop of radius r = 0.65mm. We investigated the surface E-fields of a series of filament tip shapes (see Fig 3.2) and calculated the $E_{external}$ required to produce $E_{surface} > E_{disruption}$.

We found that, as expected, $E_{external}$ decreases from a high of 925 kV/m for the hemispherical shape, Fig 3.2(a), to a low of 200 kV/m for the "sharper" shape shown in Fig 3.2(c). Photographs of coalesced drops in CL show that the non-hemispherical shapes are the best representations. The shapes in Fig 3.2(b) and (c) both met the requirement for disruption for $E_{external} < 500$ kV/m and this is consistent with CL's observations that the filament tip disrupted in E-fields of this magnitude.

3.3.2 $E_{initiation}$ vs Q_{drop}

Pulse discharge

Fig 3.4 gives the $E_{initiation}$ values for positive burst pulse discharges from the lower (positive) end of the drop as a function of the charge, Q_{drop}, deposited on the drop by the negative discharge from the

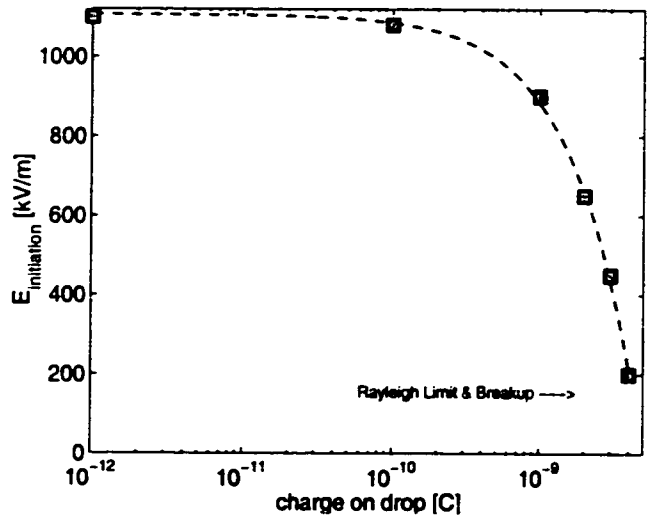

Figure 3.4: $E_{initiation}$ for positive burst pulse discharges from the lower, positive end of the drop as a function of Q_{drop}, the charge deposited on the drop by the negative corona from the upper end. The drop length is held fixed at L = 20mm.

upper end. The drop length is held fixed at L=20mm.

$E_{initiation}$ decreases rapidly once Q_{drop} exceeds 10^{-10} C. The Rayleigh stability criterion gives Q_{RL}, the maximum charge that a sphere of liquid can hold before the electrostatic repulsive force overcomes the surface tension (Rayleigh, 1882; Taylor, 1964). In SI units it is given by:

$$Q_{RL}^2 = 64\pi^2 \varepsilon_o \cdot r^3 \sigma \tag{3.1}$$

where r is the sphere radius and σ is the surface tension.

For our drop dimensions $Q_{RL} \approx 4 \times 10^{-9}$ C. Since CL did not observe disruption of the lower surface of the drop, we limited our calculations to $Q_{drop} < Q_{RL}$. For larger allowed values of Q_{drop}, close to the Rayleigh limit Q_{RL}, the values of $E_{initiation}$ become comparable to CL's experimental values and to those observed in thunderclouds.

Streamers

In addition to the burst pulse discharges we also calculated the fields required to initiate streamers. For Q_{drop} just below the Rayleigh limit, $E_{initiation} \approx 400$ kV/m for streamers, approximately 50%

greater than that required for burst pulse discharges.

3.3.3 $E_{initiation}$ vs drop length, L

Pulse discharge

We now held the charge density, ρ, on the drop fixed and varied the drop length, L. The circles in Fig 3.5 represent CL's measured values. We found that our modeled values of $E_{initiation}$ for the burst pulse discharges decreased with increasing L, consistent with the trend that CL observed. The agreement between the calculated results and observation is promising and offers validation of our model processes.

In an attempt to understand the scatter in CL's data, we considered the effects of both:

1. the amount of positive charge deposited on the drop, and

2. the shape of the lower end of the drop

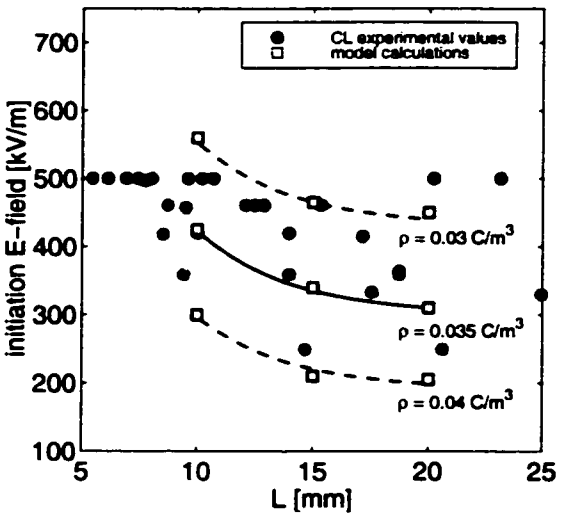

Figure 3.5: $E_{initiation}$ for burst pulse discharge as a function of the drop length L, for fixed charge density. Squares: calculated values of $E_{initiation}$ for burst pulse discharges. Circles: Crabb & Latham's measured values.

The outer curves in Fig 3.5 show that a 0.01 C/m^3 variation in the charge density of the drop is consistent with the variation of the CL data. A gross variation of drop shape - a perfectly spherical lower end - resulted in $E_{initiation}$ = 750 kV/m (ρ = 0.035 C/m^3, L = 20mm). This point lies well out of the range of CL's data and indicates that the observed variation might be due to much subtler shape variations. It is likely that the scatter in the CL data resulted from a combination of charge and shape variations.

Streamers

The same calculations were carried out for streamers and the results are shown in Fig 3.6. $E_{initiation}$ decreased with L in much the same way as for burst pulses. The $E_{initiation}$ values for the streamers were, however, ~ 50% larger than those required for burst pulses.

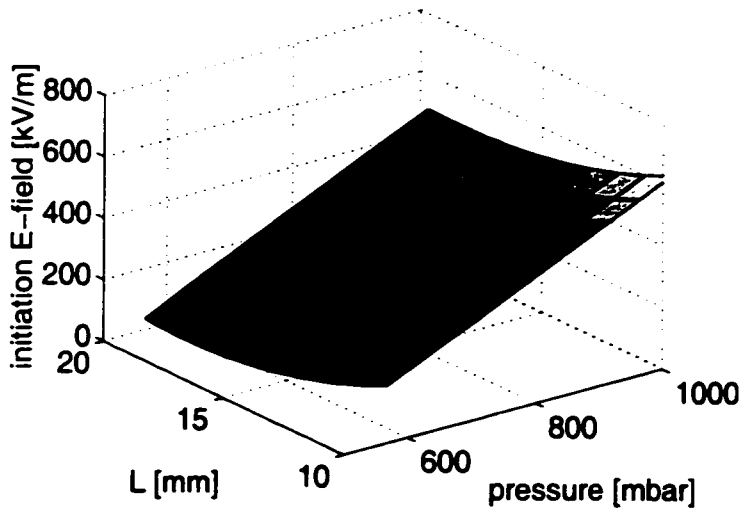

Figure 3.6: $E_{initiation}$ for streamers as a function of both drop length, L [mm], and air pressure, p [mbar]

Discussion

To understand the decrease in $E_{initiation}$ with L we consider two effects (see Fig 3.7):

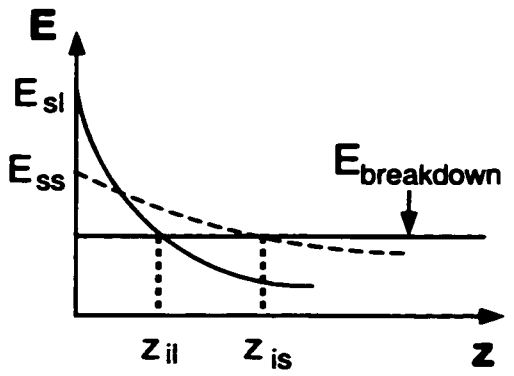

Figure 3.7: Schematic of E-field as a function of distance, z, from the surface of the drop. E_{sl} and E_{ss} are the surface fields for long (20mm) and short (10mm) drops, respectively. The ionization zone boundaries for long and short drops are indicated by z_{il} and z_{is}, respectively.

1. that for a given ambient E-field, the surface field at the tip of the filament increases with increasing L, which lowers $E_{initiation}$, and

2. that as L increases $E_g(z)$ decreases more rapidly with z, the distance from the surface. This reduces the size of the ionization zone and thus increases $E_{initiation}$.

Our results show that the former process dominates; i.e. that the increased average field within the ionization zone compensates for the electron's shortened path - leading to a lowering of $E_{initiation}$ as the drop's length is increased. However, $dE_{initiation}/dL$ decreases as L increases so that the effect of increased length becomes less significant for L > 20 mm.

3.3.4 The pressure effect

All CL's measurements were made at surface pressure (1000 mbar). It is, however, of interest to know what the $E_{initiation}$ values for streamers would be at the lower pressures found in the regions where lightning initiates. We therefore calculated $E_{initiation}$ for streamers over a range of pressures.

The variation of $E_{initiation}$ for streamers with both pressure and drop size is shown in Fig 3.6. The dark region in the lower left corner indicates the region in which initiation is most favorable - large L and low pressure. Over the chosen ranges of pressure and L, pressure has a greater effect on

$E_{initiation}$ than L.

Fig 3.6 indicates that $E_{initiation}$ varies linearly with pressure. The model parameters: α, η, D and v are functions of E/p while μ and $f_1 \cdot f_2$ are functions of $l \cdot p$ (see Fig 2.4). The linear relationship between $E_{initiation}$ and pressure suggests that the terms which depend on E/p dominate and that there is a unique value of the "reduced" E-field, $Y_{initiation} = E_{initiation}/p$ for a particular E and p combination.

3.3.5 Propagation

The E-field necessary to sustain stable streamer propagation, $E_{propagation}(p)$, was measured by Griffiths and Phelps (1976a) as a function of air pressure, p, and absolute humidity. Streamers, once initiated, will continue to propagate provided $E_{initiation} \geq E_{propagation}$. Griffiths and Phelps (1976a) found that $E_{propagation} \sim 400$ kV/m for dry air at $p = 1000$ mbar and that $E_{propagation}(p) \propto p^5$ (Fig 3.8). At $p = 500$ mbar $E_{propagation} \sim 150$ kV/m for dry air. $E_{propagation}$ increases linearly with increasing absolute humidity at a given air pressure.

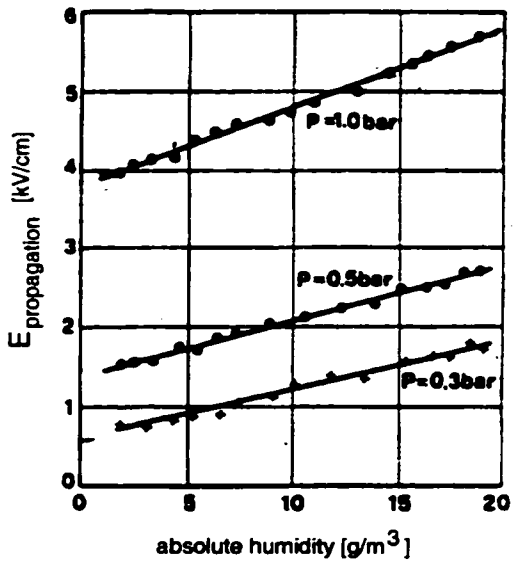

Figure 3.8: $E_{propagation}$ as a function of absolute humidity and pressure, p, (Griffiths and Phelps, 1976a).

For $p = 1000$ mbar, our calculations yield $E_{initiation} > 400$ kV/m $= E_{propagation}(1000$ mbar) for all L (Fig 3.6). Streamers initiated under these conditions will therefore be able to propagate over the entire length of the region in which $E_{external}$ remains constant. In thunderclouds this scale is typically hundreds of meters. At lower pressures, however, $E_{initiation}(p)$ exceeds $E_{propagation}(p)$ over only a small range of drop length, L.

3.4 Results for Ice Particles

3.4.1 $E_{initiation}$ vs crystal length

Griffiths and Latham (1974) grew ice needles of various lengths (L = 4mm, 7mm and 14mm) and measured the the E-fields required to initiate a burst pulse discharge as a function of the pressure in their chamber. Our model ice crystals all had the same aspect ratio (10:1), identical tip shapes, varied in length from L = 4mm to L = 14mm and had no net charge.

Fig 3.9 shows both the experimental and model results of the variation of $E_{initation}$ for burst pulse discharge with varying pressure and crystal length.

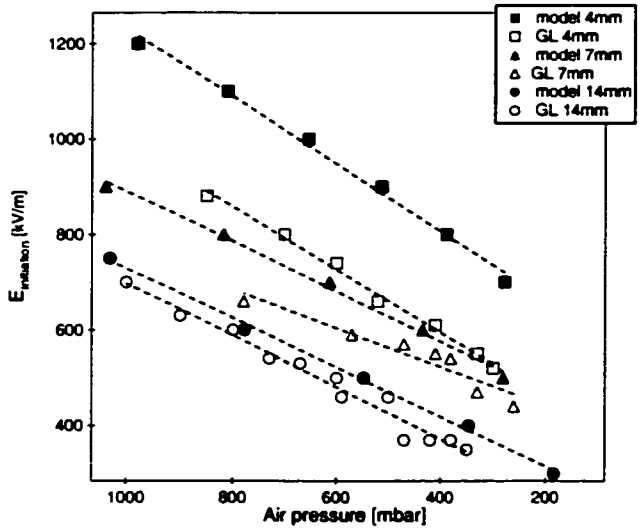

Figure 3.9: Model and observation results of $E_{initation}$ for burst pulse discharge as a function of pressure for ice crystals of lengths L = 4mm, 7mm and 14mm.

GL could not conclusively determine whether there was a correlation between $E_{initiation}$ and the crystal length, L. The ambiguity is likely due to the fact that, while the crystal samples had the same length, they had different aspect ratios and different tip shapes. Our model gave us the advantage of controlling the shape of the crystals and thus isolating the effects on $E_{initation}$ to those caused only by changes in length. We found that $E_{initation}$ was consistently decreased for increasing crystal length.

Our model results matched the general trend of GL's observations (decreasing $E_{initation}$ with decreasing pressure and increasing L) but our values of $E_{initation}$ were consistently higher than the observations. This is most likely due to the fact that our modeled crystal has perfectly smooth surfaces. This is unlikely to be true of the laboratory grown specimens used by GL. Surface irregularities would likely lower $E_{initation}$ because the E-field near these small irregularities will be high. The enhanced $E_{surface}$ will help lower $E_{initiation}$.

3.4.2 $E_{initiation}$ vs crystal shape

Information on the aspect ratio and the exact tip shape of the laboratory grown crystals was not available and we therefore chose to look at the effect of varying these quantities on $E_{initation}$. We found that decreasing the aspect ratio resulted in a lowering of $E_{initiation}$ (Fig 3.10). We chose to keep the angle of the tip, measured from the z-axis, constant while the aspect ratio was varied. This had the effect of shortening the tip when the aspect ratio was decreased. The most significant effect of changing the aspect ratio is the resulting change in crystal volume. As the needles were thinned the volume decreased, resulting in less charge being separated and less E-field intensification at the needle tip. Figure 3.11 shows the effect of volume on the surface E-field, $E_{surface}$, at the tip of the crystal. Thus an increase in either crystal length or radius will result in an increased crystal volume which translates into greater E-field intensification and lower $E_{initiation}$ values.

In Fig 3.12 we see that the relationship between $E_{initiation}$ and tip angle (as measured from the z-axis) is not monotonic. A tip angle $\theta \sim 30^o$ produces the lowest value of $E_{initation}$. This optimal value can be explained by once again considering Fig 3.7. For smaller θ values (more pointed tips) the surface E-field is high but the E-field drops off quickly, reducing the size of the ionization region. For angles greater than $\theta \sim 30^o$ the ionization zone is larger but the surface E-field is now reduced. These are two competing processes which each reach their optimal values when $\theta \sim 30^o$, producing

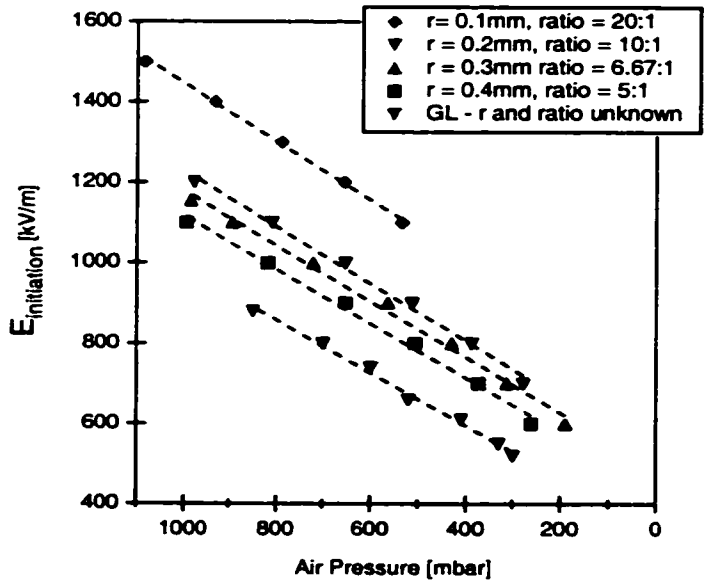

Figure 3.10: Model results of $E_{initation}$ for burst pulse discharge as a function of pressure for ice crystals of varying aspect ratios from 20:1 to 5:1.

the lowest $E_{initiation}$ values for this configuration.

3.4.3 $E_{initiation}$ vs charge on the crystal

The application of charge to the ice crystal in the model produced the largest variation in $E_{initiation}$ within the given limits. GL applied charges of between 30 and 300pC to their ice particles and found a reduction of $\sim$ up to 20% in $E_{initiation}$. In-cloud observations suggest that for ice crystals the charge on these particles rarely exceeded 50pC (Jayaratne, 1999). Fig 3.13 shows both our model results for $E_{initiation}$ as a function of pressure and applied charge.

3.4.4 $E_{initiation}$ for streamers

While GL limited their observations to recording the initiation of burst pulse discharges we could use our discharge model to determine what E-fields would be required for the initiation of propagating streamers. This is the quantity of greater interest as these streamers could potentially give rise to lightning leaders (see section 2.2.3). As with the coalesced drops, we found the initiation fields for

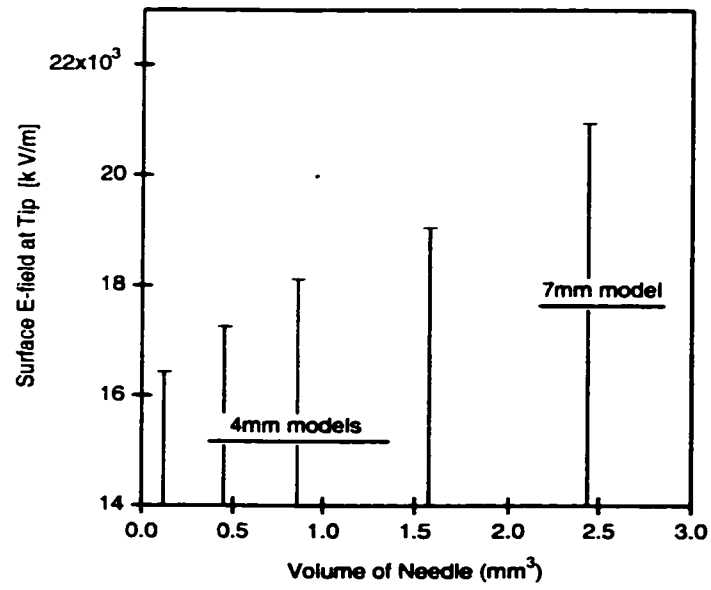

Figure 3.11: Effect of volume changes on the intensification of the E-field at the tip of ice needles.

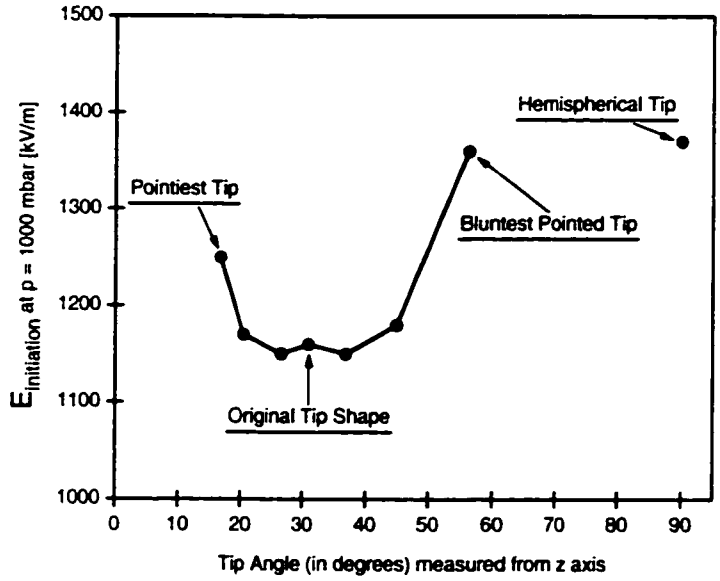

Figure 3.12: $E_{initiation}$ at surface pressure as a function of tip angle for a 4mm needle shaped ice crystal.

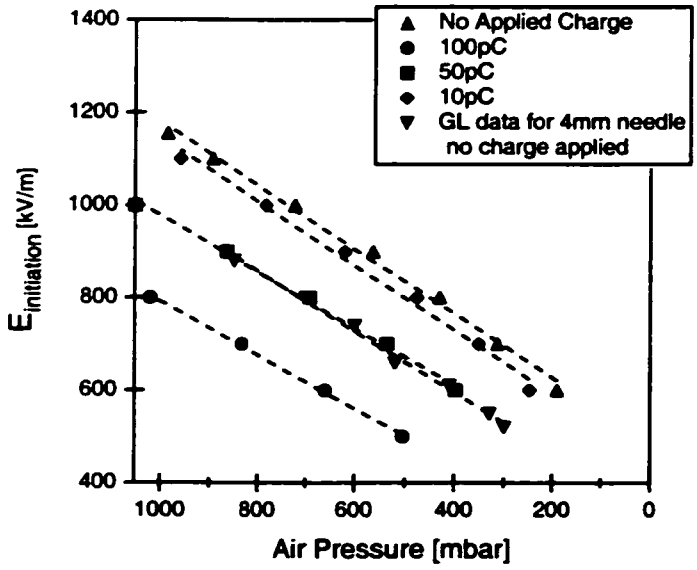

Figure 3.13: Model results of $E_{initation}$ for burst pulse discharge as a function of pressure for ice crystals with applied charge $0 < Q < 100$pC.

streamers, $E_{initiation}$, were consistently higher than for the burst pulses. Fig 3.14 shows our model results for $E_{initiation}$ as a function of pressure and applied charge for an ice crystal with L = 4mm.

3.5 Discussion

In the preceding sections we have shown that propagating streamers can be initiated from water drops at the pressures and E-fields found in thunderstorms. Furthermore, these streamers are capable of propagating over considerable distances - the distances being limited by the size of the region in which $E_{external}$ is greater than $E_{propagation}(p)$. However, the currents carried by individual streamers initiated at the drops are several orders of magnitude too low to produce sufficient Joule heating effects to produce leaders (Bondiou, 1997). These streamers may, however, still eventually lead to leader formation.

The implications of our results regarding the initiation of propagating streamers from ice particles was less promising. From Fig 3.14 we see that even for highly charged ice needles ($Q \sim 200$pC) in E-fields $\sim$ 400 kV/m the ice particles would have to be at altitudes where the pressure was less

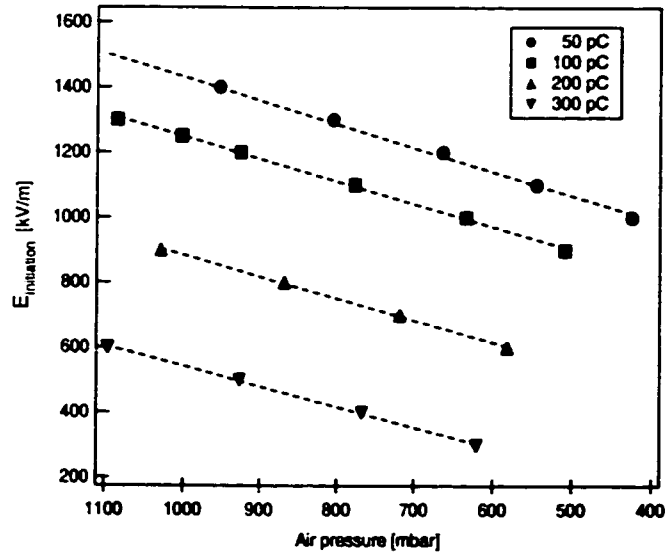

Figure 3.14: Model results of $E_{initation}$ for streamers as a function of pressure for ice crystals of length L=4mm and applied charge $50 < Q < 300$pC.

than 300 mbar (> 9km) in order to initiate a streamer. GL's experiments are only valid for T > 18°C. For lower temperatures the surface conductivity of ice becomes negligible.

GL did make additional measurements for other ice crystal shapes (prisms, plates and hail particles). Due to the geometric constraints of our model we were unable to study non-axially symmetric crystal shapes. However, GL s measurements show that $E_{initiation}$ values for these other crystal shapes were approximately the same as for the needle shaped crystals at a given pressure. Thus, unless ice needles can carry a charge $Q > 300$pC, ice particles do not provide a likely mechanism for the initiation of propagating streamers and subsequent lightning leader formation.

Initiation of streamers from liquid water drops thus looks like the more likely lightning initiation mechanism. However, the currents carried by these streamers are very low. The question of how the initiation of these low current streamers might lead to the formation of lightning leader channels is discussed in Chapter 4.

Chapter 4

Evaluation of the Hydrometeor and Runaway Hypotheses for Lightning Initiation

We now review the results that support the hydrometeor and runaway breakdown hypotheses in order to evaluate whether either of these mechanisms provides a definitive answer to the lightning initiation puzzle.

4.1 Hydrometeor Hypothesis

Tables 4.1 and 4.2 summarize the important observations and model results applicable to the hydrometeor hypothesis.

We found that hydrometeor shape is an important factor in determining initiation E-fields and leads to a large amount of scatter in the E_{init} values (Schroeder *et al.*, 1999). The values presented in Tables 4.1 and 4.2 should thus be considered "best case" values.

Positive discharges are initiated at lower electric fields than negative discharges and as a result most of the hydrometeor investigations have focussed on positive discharges. All E_{init} values in Tables 4.1 & 4.2 are for positive discharges.

Early investigations focussed only on the electric fields necessary to initiate discharges at surface pressure ($p = 1000$ mbar). However, since E_{init} decreases with decreasing pressure it is important to establish the values of E_{init} for pressures at which lightning is typically initiated. We addressed this problem, using numerical calculations to look at E_{init} as a function of pressure. Our results are summarized in Table 4.2 which shows E_{init} at $p = 500$ mbar.

Table 4.1 shows the E_{init} at surface pressure and is cataloged by hydrometeor type. Crabb and Latham (1974) showed that colliding drops had E_{init} as low as 250 kV/m but at this value only burst pulse discharges were initiated. Model results (Schroeder *et al.*, 1999) show that $E_{init} \sim 500$ kV/m

Table 4.1: Experimental and model results showing the electric fields necessary to initiate a discharge at surface pressure (p = 1000 mbar). Charge refers to whether the hydrometeor was charged or not and initiation types are defined in section 2.2.2. References for each of the results shown are: 1. Macky (1931) (M), 2 & 3. Richards and Dawson (1971) (RD), 4. Crabb and Latham (1974) (CL), 5. Schroeder *et al.* (1999) (Sch), 6. Griffiths and Latham (1974) (GL) and 7. previously unpublished result (UnPub).

	Hydrometeor type	Source	Charge	E_{init} [kV/m]	Init. type
1.	falling drops	M (expt)	no	800	burst pulse
2.	falling drops r=2mm	RD (expt)	no	950	burst pulse
3.		RD (expt)	yes	550	burst pulse
4.	colliding drops R=2.7mm, r=0.65mm	CL (expt)	no	250	burst pulse
5.		Sch (model)	no	500	streamer
6.	ice, needle	GL (expt)	no	1000	burst pulse
7.		UnPub (model)	no	1500	streamer

is necessary to initiate a propagating streamer. At $p = 500$ mbar this value drops to $E_{init} \sim 200$ kV/m which is closer to the range of measured electric fields in thunderclouds (Winn *et al.*, 1974; Marshall *et al.*, 1995).

At $p = 500$ mbar we see that the E_{init} for streamers from ice needles is still much greater than measured in-cloud electric fields (Table 4.2). Liquid water drops thus appear to be the more likely hydrometeor initiation mechanism.

4.1.1 Leader formation

As discussed in section 2.2.3, the formation of the leader requires that the temperature in the streamer channel reaches $T = 1500$K and that the linear charge density reaches $\approx 10^{-4}$ C/m. The cosmic ray initiation mechanism creates a large region (length scale of tens of meters) in which $E > E_{breakdown}$. In this region the streamer channel is able to grow and transform into a leader.

Table 4.2: Experimental and model results showing the electric fields necessary to initiate a discharge at p = 500 mbar. References for each of the results shown are: 1. Schroeder *et al.* (1999) (Sch), 2 & 3. Griffiths and Latham (1974) (GL) and 4 & 5. previously unpublished results (UnPub).

	Hydrometeor type	Source	Charge	E_{init} [kV/m]	Init. type
1.	colliding drops R=2.7mm, r=0.65mm	Sch (model)	none	200	streamer
2.	ice, needle	GL (expt)	none	600	burst pulse
3.	ice, needle	GL (expt)	100 pC	500	burst pulse
4.	ice, needle	UnPub (model)	none	1100	streamer
5.	ice, needle	UnPub (model)	100 pC	900	streamer

However, the hydrometeor mechanism only initiates a low current streamer and requires a second step in order to achieve leader status. Possible mechanisms for this second step are discussed below.

Griffiths and Phelps (1976b) considered the role of small scale discharges in thunderclouds, calculating the electric field enhancement due to multiple propagations of positive streamers near an electrode. They developed a model, based on the Dawson and Winn (1965) model, with the goal of finding a mechanism by which the propagation lengths of the streamers could reach several meters. They suggested this might be achieved by a series of streamers propagating one after the other in the same region of space, each benefiting from the space charge left by the previous one and increasing the electric field enhancement at the source. Their model was electrostatic and propagation was based on an energy criterion, such that propagation continued so long as the energy gained by electrons in the increasing electric field was greater than the sum of that lost to ionization and attachment (parameterized by a single number) and that lost to interactions between the space charge and the electrons.

According to their model, a series of three to seven streamers gave rise to an enhanced electric field of up to $\sim$ 1500 kV/m over a region of several meters near the electrode. At p $\sim$ 500 mbar this electric field is large enough to lead to large scale breakdown of the air in this region and give rise to the high current streamer needed for leader formation. Griffiths and Phelps (1976b) found

that the field was intensified on a time scale of $\sim$ 1 ms, which is comparable to the lifetime of the coalesced drops as measured by Crabb and Latham (1974). It is possible that, in this manner, several continuous streamers initiated from drops in the thundercloud could give rise to a leader. Further investigation is required to determine whether a single drop is in fact capable of initiating multiple streamers or whether drops in close proximity to one another could have the same effect.

Another mechanism for leader formation, based on the close proximity of initiating drops, that requires investigation is the merging of several streamers to form a single, more vigorous streamer with a linear charge density $> 10^{-4}$ C/m i.e. to transform the streamer to the warm leader stage. If we think of drops that initiate continuous streamers as "electrodes" then the number of "electrodes" available increases with increasing E because a wider range of drop sizes will initiate streamers at that E value (Schroeder *et al.*, 1999). Thus the likelihood of several streamers initiating in close proximity increases and the chance of leader formation is increased. This is also consistent with the observations of large amounts of corona activity in thunderstorms without lightning; i.e. the "electrode" density must be sufficiently high before streamers are able to merge and form a leader.

The streamers observed by both Crabb and Latham (1974) and examined in our model were all positive, occuring at the lower end of drops. This corresponds to drops located above the negative charge center in clouds. Drops located below the negative charge center have negatively charged lower ends and investigation of this situation will require the modeling of negative streamers which are much more complex in nature than positive streamers (Castellani *et al.*, 1994). No attempt has been made in this study to model these negative processes but future attempts should investigate this phenomenon.

4.2 Runaway Breakdown Hypothesis

As we saw in Chapter 2, the cosmic ray induced runaway breakdown leads to the establishment of a strongly polarized plasma region that creates an enhanced electric field. Since the electric field enhancement takes place at both ends of the polarized region, lightning triggered via this mechanism can propagate upwards or downwards. Table 2.1 shows that during one second approximately two cosmic ray particles with $\varepsilon_o \approx 10^{15}$eV cross a 1 km^2 area. Thus in a cloud with an area of 10 km^2 approximately 20 $\varepsilon_o \approx 10^{15}$eV cosmic rays enter the cloud. This frequency is consistent with

observed lightning frequencies.

It is then of interest to know how sensitive this initiation mechanism is to thundercloud characteristics. We have developed a numerical model based on the equations outlined in section 2.3 (Solomon *et al.*, 2000). This model is used to investigate the thunderstorm conditions that are required to form a plasma region. We find that at an altitude of 6 km a region the in-cloud electric field must exceed the breakeven electric field over a length $2L_{be} \sim 1.5 - 2$ km, is required in order for a plasma region to form. At this altitude $E_{be} \sim 100$ kV/m. As altitude increases the length L_{be} increases while $E_{be}(p)$ decreases.

Analysis of balloon soundings of electric fields in thunderclouds suggests that lengths of $2L_{be} \sim 1.5 - 2$ km are rarely, if ever, reported (Solomon *et al.*, 2000). However, we must consider that observations of in-cloud electric field profiles made via instrumented balloons are not instantaneous snapshots of the vertical field. A typical in-cloud sounding takes about 60 minutes to collect and this factor introduces important errors into the interpretation of the measured electric fields. Since instantaneous profiles of electric fields within thunderstorms are impossible to obtain, we use a numerical thunderstorm model (described in Chapter 5) to study this relationship. We examine the electric field obtained from a New Mexico thunderstorm and simulate what a balloon would observe if it were launched at various times during the model run. We find that the altitude and magnitude of the peak electric fields vary considerably between simulated balloon ascents started at different stages in the cloud's lifetime. However, even with these limitations, neither the model results nor the observations suggest that E exceeds E_{be} over the vertical length required to form a plasma region.

Thus, although the cosmic ray lightning initiation mechanism requires more modest electric fields than the hydrometeor mechanism the requirement that the electric fields must be in excess of E_{be} over lengths greater than those observed decreases the attractiveness of this mechanism.

4.3 Future Work

It appears that neither the hydrometeor nor the runaway breakdown hypothesis provides an obvious solution to the lightning initiation puzzle. Both hypotheses, according to present observations and calculations, require electric fields at the extremes of observed values or moderate electric fields that exist over lengths greater than those observed.

One important advance would be improved electric field measurements in thunderclouds. Until we have some degree of certainty regarding the magnitude and extent of the electric fields in clouds the proposed lightning initiation mechanisms will remain speculative.

Gurevich *et al.* (1999) have also suggested a series of experiments in which they propose to make observations with the goal of recording cosmic ray showers, runaway breakdown and lightning simultaneously. The location in which discharges initiate is in an extremely inhospitable environment but it is clear that more direct measurements of conditions there are necessary to solve the lightning initiation puzzle.

Chapter 5

Thunderstorm Datasets and Numerical Thunderstorm Model

5.1 Introduction

The tools used to study thunderstorms fall into two broad categories: observations and numerical modeling. Here we discuss both the observational and modeling techniques that are used in the work that follows.

The direct measurement of thunderstorm properties is a difficult and dangerous task. The first comprehensive field project that attempted to characterize air motion within thunderstorms was known simply as the "Thunderstorm Project" (Battan, 1964). This field study took place in 1949 and utilized the expertise and bravery of World War II fighter pilot veterans. More modern projects have been limited in the extent to which they can penetrate active thunderstorms. Electric field soundings can be obtained via balloons and some flights do still penetrate thunderstorms, but only before the storm becomes active.

Most data are now obtained via remote sensing techniques. A wide variety of ground based and satellite detectors are currently measuring thunderstorm properties. Satellite data are particularly useful for producing long term global climatologies. We will discuss the availability and collection of thunderstorm data in Section 5.2.

Numerical models of thunderstorms offer an opportunity to improve our understanding of the processes occuring within thunder storms in lieu of effective direct or remotely sensed measurements. Our group has developed a numerical model of the thunderstorm process which captures the major characteristics of thunderclouds and is discussed in detail in section 5.3.

The thunderstorm model allows us to test the sensitivity of lightning production to changes in environmental parameters. Field studies can provide some data on these sorts of sensitivities by

measuring changes in environmental parameters and those properties of the thunderstorms that are currently easily measurable. However, unlike laboratory conditions, the environmental conditions can not be controlled. The numerical model offers the opportunity to "control" the environmental conditions and thus gain insight into how a change in a single parameter may affect the properties of thunderstorms.

5.2 Thunderstorm Data

Thunderstorm data is primarily collected in two ways: (1) case studies that focus on a specific area and time period and, (2) global monitoring on long time scales.

In case studies data are typically collected using surface detectors (electric field mills, radar, CCN counters, etc) and aircraft which sample in-cloud conditions such as drop and ice concentrations, updraft velocities and mass flux. We will make use of data from a number of case studies that have taken place over the last decade around the world. The specifics of data taken during these case studies will be discussed in more detail as they come up in the course of our work in the following Chapters.

The National Lightning Detection Network (NLDN) is a network of antennas that use a combination of time-of-arrival and direction finding techniques to locate the flashes. The database includes the time, polarity, peak current and number of strokes of each detected cloud-to-ground lightning flash over the United States. The detection efficiency is between 80 - 90%. This database provides valuable regional lightning data.

It is, however, not practical to obtain a global dataset of lightning using these types of ground based detectors. Many of the areas in which lightning flash rates are high are remote and these ground based detectors would necessarily exclude detection of oceanic lightning.

There is one type of ground based detection technique that can provide global lightning information. Sferics are the radio-frequency electromagnetic radiation originating in lightning discharges which can be heard as static on AM radios. A VLF radio noise receiver network was established in 1996 to measure the distribution of sferics out to ranges of several thousand km. The network consists of four receivers in the eastern U.S. and employs both arrival time differences measuring techniques and magnetic direction finding at frequencies between 5 and 15 kHz. Sferics can provide

important information about total lightning activity but accurate location of flashes is not possible.

A number of different platforms have thus been developed to make above cloud observations of lightning. These platforms include aircraft (Christian *et al.*, 1983), high altitude balloons (Holzworth and Chiu, 1982) and satellites (Orville and Henderson, 1986). Early satellite measurements of lightning - such as those made by the DMSP satellite - recorded the lightning photographically. These data were thus very limited in that they only showed lightning at night (Orville and Henderson, 1986). In addition the location accuracy was very poor and the detection efficiencies were very low (less than 2%)

Global lightning data are now being acquired by both the Optical Transient Detector (OTD) aboard the Microlab-1 satellite as well as the Lightning Imaging Sensor (LIS) on the Tropical Rainfall Measuring Mission (TRMM) observatory. Both are optical sensors that detect lightning by looking for small changes in light intensity. Thus these detectors are capable of observing lightning during daylight hours.

The OTD was launched in 1995 and was a prototype of the later LIS instrument. It has a 1300km x 1300km footprint and views a particular geographic location for approximately 3 minutes. The spatial resolution is on the the order of 10km. OTD has a detection efficiency of $\sim$ 50% for both intra cloud and cloud to ground lightning. It is in a near polar orbit and views the full diurnal cycle at a particular location approximately every 55 days. Thus, in order to avoid introducing a diurnal bias, data should be summed over this time period. For this reason we make use of seasonal composites of OTD data. OTD covers a large latitudinal range ($\sim$ 80N to 80S) giving close to full global coverage.

The newer LIS instrument, in a tropical orbit, has reduced coverage (35N to 35S) but offers a greatly improved detection efficiency ($\sim$90%) (Christian *et al.*, 1999). It is in a low Earth orbit at an altitude of 350km and has a 600km x 600km footprint. It views individual storms for a duration of approximately 90s. LIS has a spatial resolution of 3 to 6km. The full diurnal cycle is covered every 80 days at each location by LIS. Both detectors record the duration for which a particular location is viewed and it is thus possible to determine the flash rate at each location. Figure 5.1 shows a map of seasonal lightning flashes compiled using LIS data.

The TRMM satellite has 4 other instruments in addition to the LIS each designed to observe different thundercloud properties. In particular we will make use of data from the Visible and Infrared Scanner (VIRS) which collects cloud-top height information.

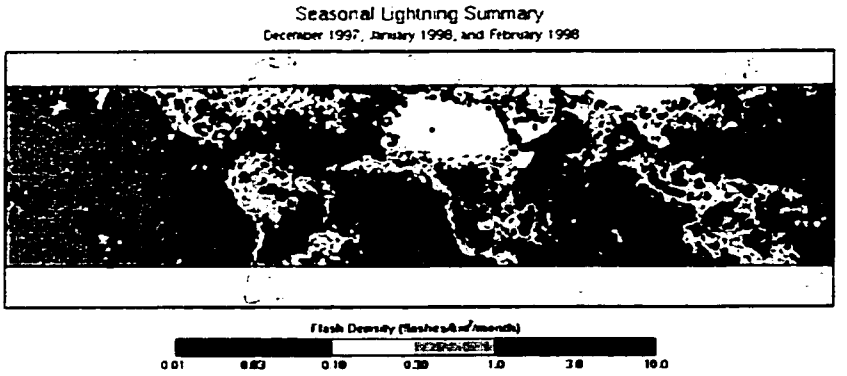

Figure 5.1: Seasonal map of lightning flash density [flashes per km^2 per year] from LIS (Christian *et al.*, 1999).

5.3 Numerical Thunderstorm Model

Our numerical thunderstorm model domain is axially symmetric with high vertical resolution and a very coarse radial resolution. The domain consists of three regions - an inner cloud, outer cloud and cloud-free environment region (see Fig 5.2). This type of geometry is often referred to as 1.5 dimensional. The simple geometry keeps the cloud dynamics calculation time short and allows us to include a simple lightning parameterization. We will refer to the thunderstorm model as TENEBROUS hereafter.

TENEBROUS uses parameterizations in the calculations of the cloud dynamical and lightning processes while the cloud microphysics is modeled explicitly. The explicit microphysics is required in order to include a charge transfer mechanism that is dependent on particle size (Saunders *et al.*, 1991).

TENEBROUS was written and developed by three former graduate students in our group: Greg Taylor (dynamics), Kent Norville (microphysics) and Robert Solomon (lightning parameterization).

What follows is a brief description of the main model components along with references to more detailed information. Special attention is given to model parameters and functions that are referred to in later discussions. A schematic of the various components that make up the model are shown in Fig 5.3.

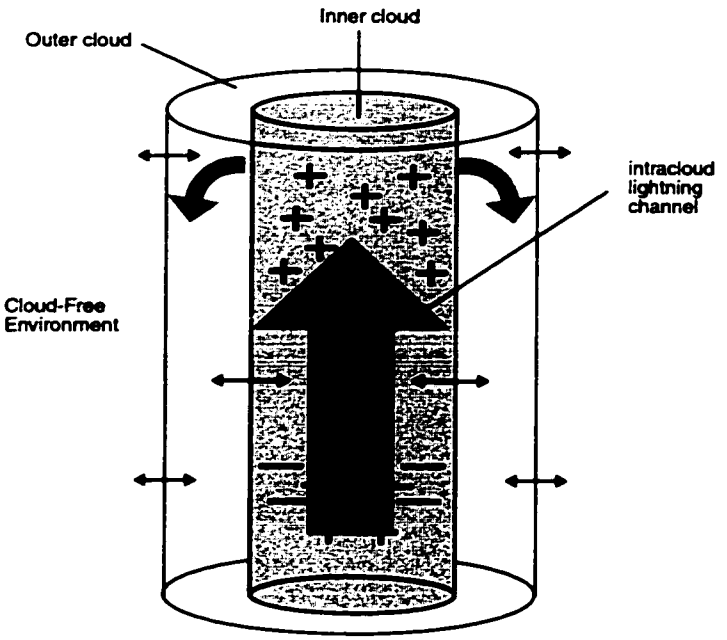

Figure 5.2: Schematic of our 1.5D numerical thunderstorm model. The model consist of 3 cylindrical regions and includes simple dynamics, entrainment, explicit microphysics, electrification and a lightning parameterization.

5.3.1 Inputs

TENEBROUS is initialized with an environmental sounding which includes temperature and dewpoint temperature as functions of pressure. There are a number of additional input parameters that are based on local environmental conditions and are used to initialize the calculations in the various components that make up TENEBROUS. Wherever possible we use observations of local conditions to set these parameters. For example, information on storm duration, cloud radius, cloud base pressure and cloud condensation nucleus concentration may be available from observations.

Input parameters pertinent to the research presented in subsequent Chapters will be discussed in the appropriate sections below.

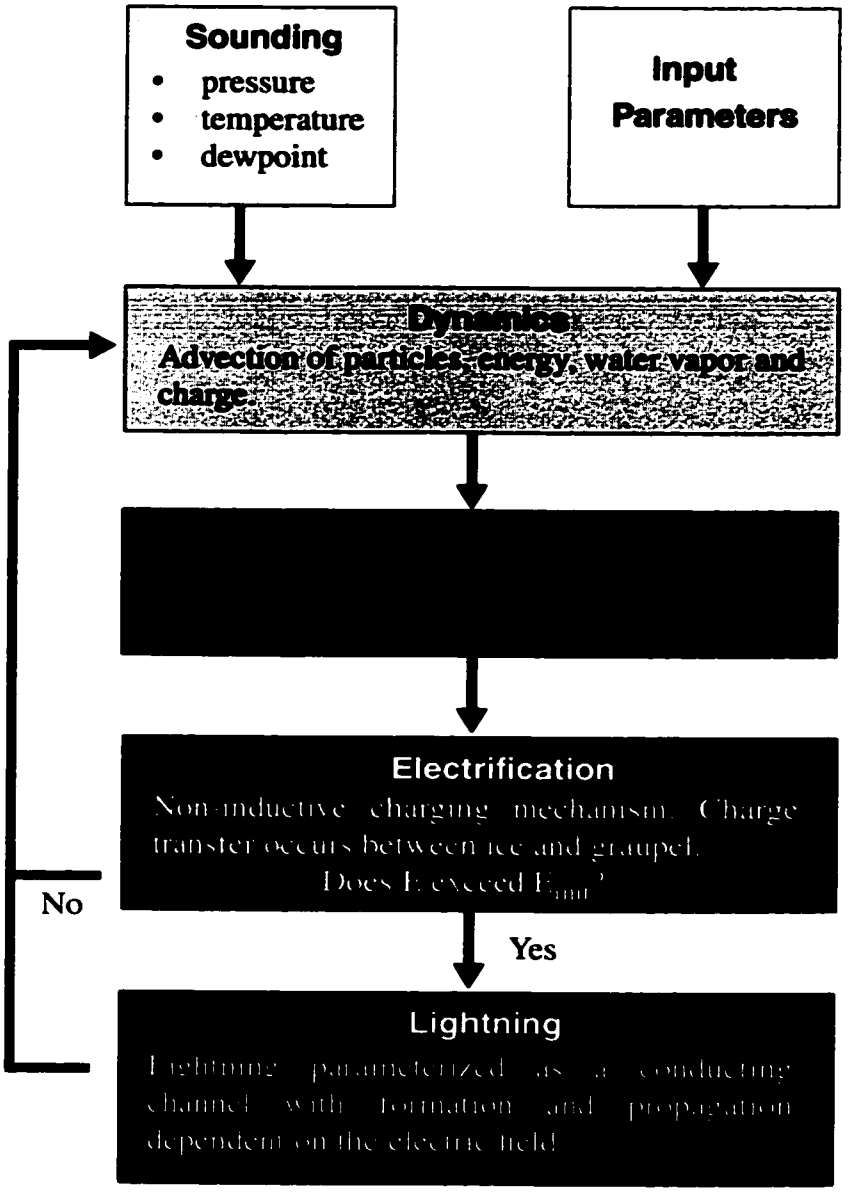

Figure 5.3: Schematic showing the components of our numerical thunderstorm model, TENEBROUS. The model is initialized with an environmental sounding and input parameters whose values are determined by local conditions. In each time step the model calculates the new dynamic, microphysical and electrical quantities. If the E-field exceeds the lightning initialization threshold, the model proceeds to the lightning parameterization component, else it steps forward in time and begins over with the dynamic calculations. Adapted from Solomon (1997).

5.3.2 Dynamics

The dynamic routines calculate the advection of all particles, energy, water vapor and charge. The equations used are described in detail in Taylor (1987) and were based on Asai and Kasahara (1967) and Yau (1980).

An important dynamic parameter is cloud base forcing which results from difference in the temperature and velocity of air entering at the base of the cloud to that of the surrounding environment at cloud base level. Forcing is achieved in two ways in TENEBROUS:

- *kinetic*: an imposed updraft velocity (w_{cb}) at cloud base (representing converging air), or
- *thermal*: an imposed temperature perturbation (ΔT) above the environmental temperature at cloud base level (representing solar heating).

In Nature cloud base forcing is likely a combination of these two forcing types. Solomon and Baker (1994), however, found that in TENEBROUS cloud electrification was not particularly sensitive to the type of forcing that was applied. In the studies that follow we used kinetic cloud base forcing exclusively.

The duration over which the forcing is applied and the "depth" of the kinetic forcing can be adjusted. The value of w_{cb} decreases exponentially above cloud base (see Fig 5.4) and the decay rate can also be set.

Another important dynamical process is the entrainment of dry environmental air into the outer cloud region. Entrainment is parameterized as a function of turbulent kinetic energy (Taylor, 1987). The calculation of turbulent kinetic energy includes a length scale that is the characteristic size of the entrainment events. This characteristic eddy mixing length is an unknown function of cloud and environmental parameters and must be specified by the user. Rodi (1981) observed that the eddy length scale in Montana cumulus clouds was 300 - 800 meters.

5.3.3 Microphysics

Ice and water particles are classified by mass into 80 categories for each phase. The routine accounts for drop formation, vapor growth, collisional growth, evaporation, melting and glaciation. CCN and ice nuclei are assumed to be spherical particles of radius 0.25 μm.

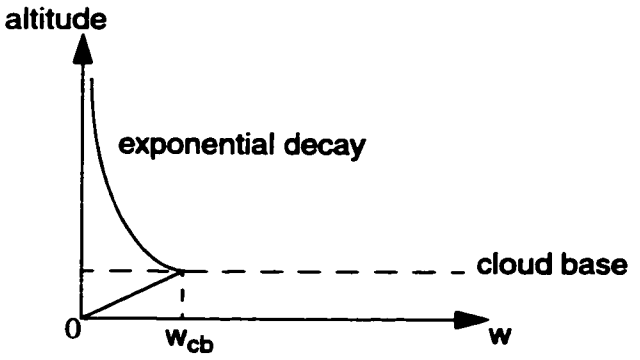

Figure 5.4: Schematic showing kinetic cloud base forcing in TENEBROUS. The updraft velocity at cloud base (w_{cb}) is set by the user. Initial updraft velocity decreases linearly below cloud base to zero at the ground while it decreases exponentially above cloud base. The decay rate is also user defined. At later times, while cloud base forcing is still on, the updraft velocity is a combination of this initial velocity profile and the cloud updraft velocity.

Initial ice crystal concentrations are determined by either the Fletcher (1962) or Meyers *et al.* (1992) parameterizations. The Fletcher parameterization is temperature dependent while Meyers depends on the ice supersaturation. The Fletcher parameterization gives lower estimates for ice nucleus concentration at high temperatures than Meyers, but higher estimates at colder temperatures.

Water and ice particles grow by vapor deposition (Pruppacher and Klett, 1978) and collision and coalescence. The 'continuous collection' approach is used to calculate the collection of droplets by larger drops. Additional ice particles can also be produced by secondary ice production. Experiments by Hallet and Mossop (1974) suggest that under certain conditions ice particles may shatter, ejecting small ice fragments. They found that this secondary ice production occurs in the temperature range $-8^o < T < -3^o$C, peaking at -5^oC.

5.3.4 Electrification

We assume that charge separation only occurs via the non-inductive charge transfer mechanism. Laboratory observations (Takahashi, 1978; Jayaratne *et al.*, 1983; Baker *et al.*, 1987; Saunders *et al.*, 1991)) show that collisions between ice crystals and graupel particles result in the transfer of substantial amounts of charge. Figure 5.5 shows a schematic of a collision between a large graupel

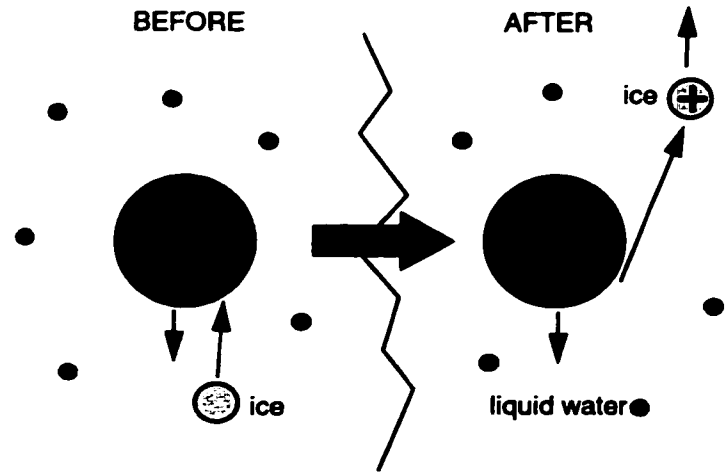

Figure 5.5: Schematic of charge transfer during ice-graupel collisions. The smaller ice particles are carried upward in the cloud while the graupel settles slowly.

particle and a smaller ice particle. A typical collision results in a charge transfer of $\Delta Q \sim 10$ fC. The exact amount of charge transferred depends on temperature, liquid water content and the size of the particles involved in the collision.

Figure 5.6 shows the sign of charge received by graupel particles during ice-graupel collisions as a function of liquid water content and temperature. Temperature and liquid water content in the charging zone are generally such that the graupel is negatively charged.

The smaller ice particles have fall speeds that are typically less than in-cloud updraft velocities and are carried upward in the cloud while the graupel remains suspended in the charging zone. As more charge is separated, the in-cloud E-field grows. When the E-field exceeds a certain threshold a lightning channel will be initiated in TENEBROUS. The E-field threshold ($E_{threshold}$) is prescribed by the user. We typically use a value of $E_{threshold} = 250$ kV/m which represents the E-field required to sustain streamer propagation at pressures of ~ 500 mbar (Fig 3.8).

5.3.5 Lightning parameterization

The lightning channel is modeled as an ellipsoidal conductor (Helsdon *et al.*, 1992; Solomon and Baker, 1998) lying along the z-axis. A channel of initial length, $L = 3dz$ (where dz is the model's

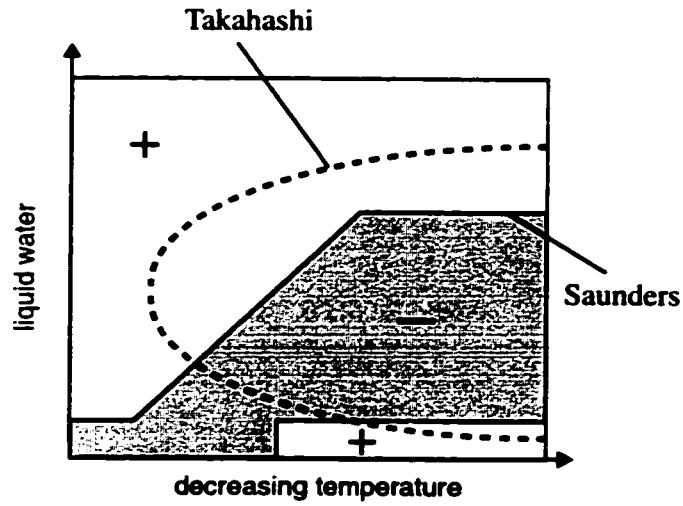

Figure 5.6: Schematic of the sign of charge transferred to graupel during ice-graupel collisions as a function of liquid water content and temperature. In TENEBROUS the Saunders *et al.* (1991) parameterization is used. Adapted from Solomon (1997).

vertical resolution), and radius, $R = 10$m, is initiated if $E > E_{init}$. Its length increases by dz on each end provided that the charge induced (Q_{ind}) on the ends of the channel by the in-cloud E-field is such that the linear charge density, $\frac{Q_{ind}}{dz} > 10^{-4}$ C/m (Bondiou, 1997). An additional propagation criterion is that the Q_{ind} at each tip must not change sign between successive steps in the propagation. If the induced charge switches sign propagation is terminated.

A more detailed description of this lightning parameterization can be found in Solomon and Baker (1998).

Chapter 6

CCN Concentration and Lightning Flash Rate

In this Chapter we investigate the sensitivity of lightning flash rate to cloud condensation nucleus (CCN) concentration. We make use of our numerical thunderstorm model together with *in-situ* and remotely sensed observations.

6.1 Background

In the last two decades there have been a number of studies that suggest that aerosol concentration may affect lightning flash rates as well as other lightning properties, such as polarity. One hypothesis (Rosenfeld and Lensky, 1998) is that the concentration of a particular aerosol type — cloud condensation nuclei — has a strong affect on the cloud droplet size distribution and thus on the cloud electrification process. Aerosol type and concentration also affects the chemistry of the charge transfer process and the ice nuclei concentration. We focus on cloud condensation nuclei in this discussion.

Optical observations of lightning from space indicate that, in general, lightning flash numbers are an order of magnitude greater over land than over oceans (Orville and Henderson, 1986; Christian and Latham, 1998). This pattern had been suspected previously but due to the lack of in situ data over the oceans quantitative information only became apparent with the advent of satellite lightning observations.

Traditional explanations for this contrast focus on the differences in Convective Available Potential Energy (CAPE) and updraft velocities in land and ocean storms, largely resulting from differences in surface temperatures. CAPE gives the potential energy available for conversion to updraft kinetic energy and can be defined as the area between the curve for a parcel rising, from cloud base,

along a moist adiabat and the environmental sounding.

$$CAPE = \int_{z_{cb}}^{z_{ct}} \frac{T_{v,ad} - T_{v,env}}{T_{v,ad}} \, dz \tag{6.1}$$

where z_{ct} and z_{cb} are the altitudes of cloud top and base, respectively. $T_{v,ad}$ and $T_{v,env}$ are the virtual temperatures on the moist adiabat through cloud base and the environmental sounding, respectively. Higher updraft velocities tend to lead to more charge separation within the cloud and thus more lightning (Solomon *et al.*, 1996; Schroeder and Baker, 1999). There are, however, problems with these traditional explanations. For instance, the land/ocean lightning contrast is also observed at local midnight when surface land heating is not as important a factor and, many oceanic storms which do have large CAPE values do not exhibit the high lightning activity that this explanation predicts (Molinie and Pontikis, 1995). Lucas *et al.* (1994) suggest that the more important factor is the shape of the 'area' on the sounding which determines the CAPE values. In oceanic soundings Lucas *et al.* (1994) found that this area tends to be 'skinny' while in a continental sounding, with the same CAPE value, this area is 'fat'. They found that the continental sounding achieved a higher maximum virtual temperature and a higher updraft velocity.

Rosenfeld and Lensky (1998) suggest an alternate explanation which relies on the differences in cloud condensation nuclei concentration (N_{CCN}) over land and ocean regions. Dirty (high N_{CCN}) air over the continents contains many nucleation sites and thus many small drops form under these conditions. These small drops have a better chance than larger drops of reaching the mixed phase region of the cloud where they can contribute to the separation of electric charge. In clean oceanic conditions drops are larger and are more likely to precipitate out before they reach the mixed phase region.

Between April and June of 1998 smoke from forest fires in southern Mexico was advected into the southern and central regions of the United States. Analysis of National Lightning Detection Network (NLDN) cloud-to-ground data (Lyons *et al.*, 1998) shows that the percentage of positive cloud-to-ground flashes tripled in the southern plains region of the U.S. during this period. The total number of cloud-to-ground flashes in the entire U.S. did not change significantly when compared to the same period during 1996 and 1997. Interestingly the total number of cloud-to-ground flashes in the southern plans region during this period was actually lower than in previous years.

However, Williams *et al.* (1999) reported that variations in peak lightning flash rates were ob-

served when N_{CCN} changes were measured during a field project in Brazil. These data were obtained over a 35 day period during January and February of 1999 and showed a trend of increasing peak flash rate with increasing N_{CCN}.

Westcott (1995) analyzed NLDN lightning in and around 16 U.S. cities during a three year period. Westcott (1995) found that lightning frequency was enhanced by $40\% - 85\%$ over and downwind of these cities. There is also anecdotal evidence from Mexico City that suggests that lightning activity in and around the city has increased over the years along with the pollution levels though it is hard to separate out other effects, such as the urban heat island effect.

Finally, additional motivation for this study was provided by optical satellite observations that show areas of anomalously high lightning activity in oceanic regions east of Southern Africa, Australia and North America. Until recently lightning data for all oceanic regions was extremely limited. Unlike the majority of oceanic regions, the above regions are conspicuous on global lightning maps, having flash densities comparable to neighboring continental regions.

In this Chapter we will explore the use of two approaches to study the link between N_{CCN} and lighting flash rates:

1. Case Study I: Using observational data (Williams *et al.*, 1999) and a numerical model (see Chapter 5) we investigate the conditions under which lightning frequency is sensitive to N_{CCN} in Brazilian thunderstorms.

2. Case Study II: In this case study we combine meteorological and lightning data from the oceanic region east of Southern Africa to constrain the process that might be responsible for the high lightning flash rate observed there, focusing on the possible role of N_{CCN}.

6.2 Case Study I: Brazil

Williams *et al.* (1999) carried out a field program in Rondonia province, Brazil (southern Amazon basin, see Fig 6.1) in early 1999 to investigate the influence of N_{CCN} on vertical development and electrical activity in tropical convection.

Radar measurements were made using a C-band Doppler radar. Lightning activity within a 50km range was detected by an electric field mill and two slow antennas (New Mexico Tech design). N_{CCN} was measured at the surface every 4 minutes using a M1 Cloud Condensation Nucleus Counter at

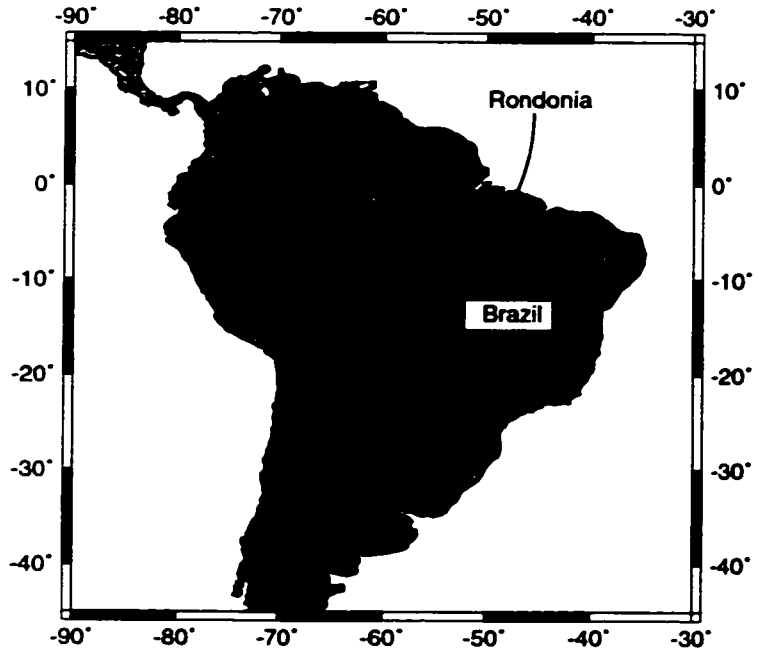

Figure 6.1: Map of South America showing the location of Rondonia province, Brazil where the Williams *et al.* (1999) study took place.

1% supersaturation.

The two basic weather conditions during the campaign can be characterized as *break period* and *monsoon* - as defined by Rutledge *et al.* (1992). These can be loosely equated to *continental* and *maritime* conditions, respectively, with regard to both environmental soundings and N_{CCN} values. The monsoon period occurs when the inter-tropical convergence zone is over South America and is characterized by widespread cloudiness, high rainfall, lower lightning flash rates and lower air temperatures at the surface. The break period, by contrast, is marked by higher surface air temperature and isolated thunderstorms with higher lightning flash rates.

Measurements by Williams *et al.* (1999) indicate that another important distinction exists between these two periods. During the monsoon periods N_{CCN} lay largely between 200 and 600 cm^{-3} while the break periods were characterized by higher concentrations between 600 and 1000 cm^{-3}.

6.2.1 Method

We used soundings from two break period days (13 & 19 January) and one monsoon day (18 January) during the Brazil campaign to initialize a numerical thunderstorm model (described in Chapter 5). The sounding for 13 January and 18 January are plotted in Figure 6.2.

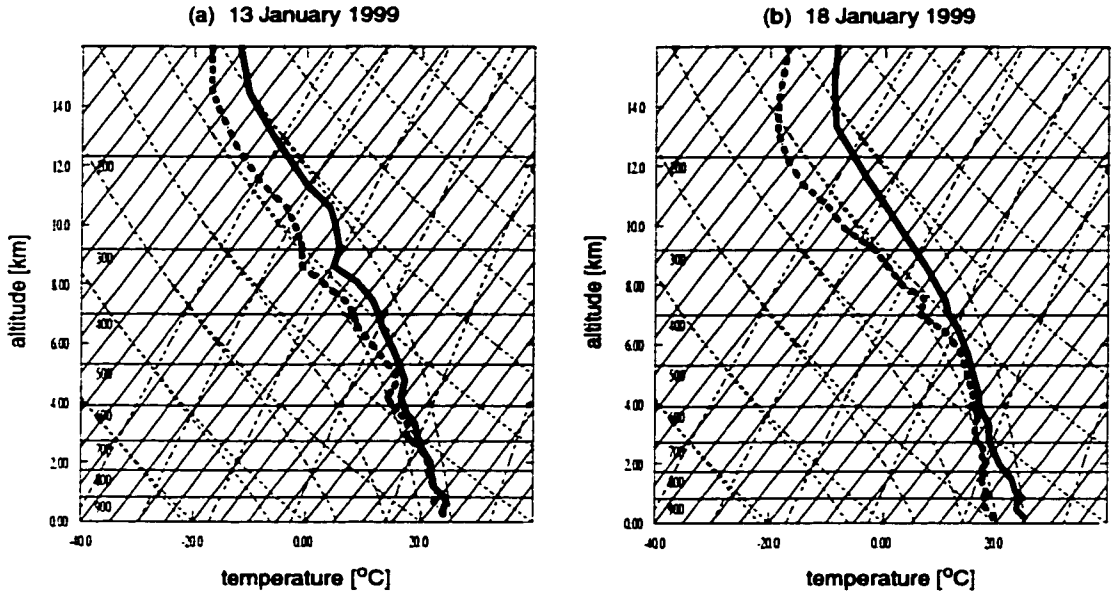

Figure 6.2: Sounding for (a) 13 January 1999 (break) and (b) 18 January 1999 (monsoon) measured and provided by Williams (2000).

In the initial model runs we limited N_{CCN} to the ranges given in Table 6.1 and assumed that all particles activated.

We then:

1. compared the model computed relationship between total lightning flash rate and N_{CCN} with that reported in Williams *et al.* (1999), and

2. used the model output to study the sensitivity of flash rate to N_{CCN}, cloud base forcing and glaciation parameterization.

Table 6.1: The sounding type, observed CCN range and Convective Available Potential Energy (as defined in Houze (1993)) for each day in our study are shown above. These soundings were used as inputs for the numerical model.

Day	type	CCN range[cm^3]	CAPE [J/kg]
13 Jan	break	600 - 1000	1210
18 Jan	monsoon	200 - 600	570
19 Jan	break	600 - 1000	1070

6.2.2 *Model verification*

Unfortunately data from the Brazil field project were very limited. We were able to obtain soundings, daily N_{CCN} data and some radar data. Williams *et al.* (1999) analyzed the limited radar data from the Brazil field project to determine the heights of the first detection of radar echos in cells within the observation range. The first echo threshold was set at 10 dBZ. Histograms of first echo height (FEH) were produced for each day. Fig 6.3 shows an example of one such day.

Fig 6.3 shows observed and model results for 18 January. The first echo heights are for model results in which N_{CCN} and cloud base forcing were varied. The most commonly occuring FEH for cells on 18 January was in the range 3 - 4 km which is also true for the model results in Fig 6.3.

6.2.3 *Results*

Fig 6.4a is a comparison of observed daily peak flash rate (F_{peak}) to daily mean N_{CCN} for 35 days during January and February 1999 (Williams *et al.*, 1999). It shows that there is a tendency for higher F_{peak} values on days with high N_{CCN}. The model results shown in Fig 6.4b compare very favorably with the observational data. The model produced slightly higher F_{peak} values than those observed by Williams *et al.* (1999), but it shows the same overall trend; increasing F_{peak} with increasing N_{CCN}. There is considerable scatter in both observations and model results but as a crude estimate a linear fit of the model results gives:

$$\frac{dF_{peak}}{dN_{CCN}} = 0.05 \tag{6.2}$$

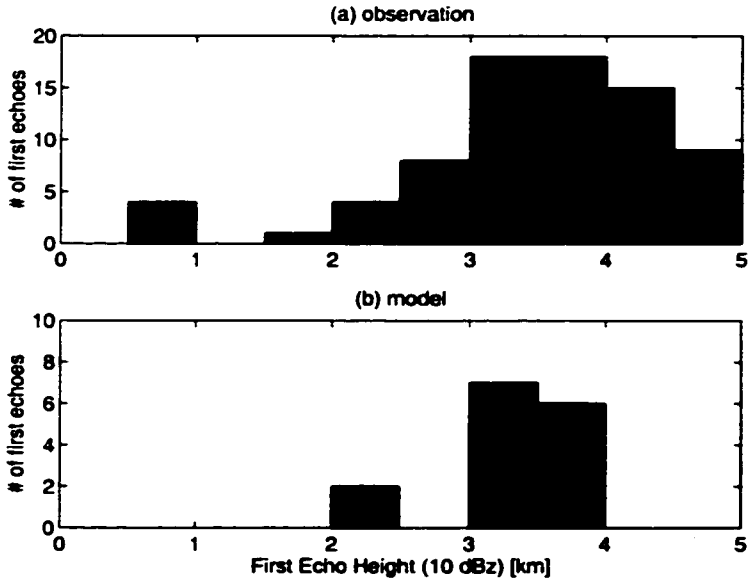

Figure 6.3: (a) Frequency of occurrence of first echo heights (10 dBZ) measured for storms occuring on 18 January 1999 in Brazil. This was a monsoon day. Data courtesy of Williams (2000). Figure (b) shows first echo heights (FEH) for model runs initialized with the 18 January sounding but with varying N_{CCN} and cloud base forcing values. While there are only 15 model storms to compare with 77 measured storms we can see that the model runs produced FEH's primarily between 3 and 4 km which is also the altitude range of the peak occurrence in the observations.

for $N_{CCN} > 200$ cm^3. The correlation coefficient $= 0.57$; high enough to indicate a significant correlation. However, since N_{CCN} is not the only variable controlling F_{peak} it is not possible to attribute the correlation solely to N_{CCN}. Thus this relationship should be used with caution and we do not believe that Eqn 6.2 should be used in global models as it stands.

Separating the effects of CAPE and N_{CCN} on flash rate

In an attempt to separate the effects of Convective Available Potential Energy (CAPE) from those of N_{CCN} on 13 January and 18 January we ran the numerical model using N_{CCN} values outside the ranges shown in Table 6.1, i.e. low N_{CCN} combined with break conditions and high N_{CCN} with monsoon conditions. The results in Figure 6.5 show that when N_{CCN} dropped below 500 cm^3 in runs initialized with break conditions, lightning ceased despite the high CAPE value associated with this

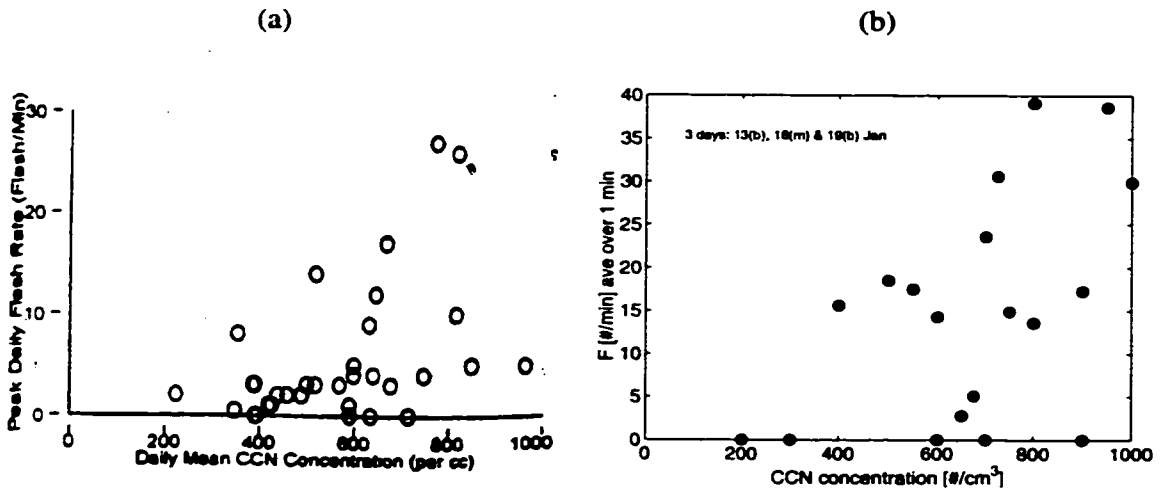

Figure 6.4: (a) Observations of daily maximum flash rate as a function of daily mean N_{CCN}. From Williams *et al.* (1999). (b) Model results of maximum storm flash rate vs N_{CCN}. Flash rates were computed by averaging over 1 minute intervals. Model runs were initialized from 3 separate soundings; one representing a monsoon (m) weather period, the remaining two were from break period (b) regimes. Each sounding was used in several model runs, each with a different N_{CCN} value.

sounding. Likewise, increasing N_{CCN} in monsoon (low CAPE) runs resulted in increased lightning activity.

Figure 6.6 shows that though w_{peak}^{break} always exceeds $w_{peak}^{monsoon}$ for a particular value of N_{CCN}, the break storm did not always produce more lightning (Fig 6.5). This suggests that in these cases w_{peak} cannot be used on its own as a predictor of lightning activity.

The variation in precipitation with N_{CCN} (Fig 6.6, lower panel) for the monsoon run is consistent with the idea that as N_{CCN} increases, drop size decreases and precipitation decreases. In the break case, on the other hand, the precipitation increased for $N_{CCN} > 600\text{cm}^3$ before decreasing again. The increase in precipitation correlates with a decrease in w_{peak}, suggesting that while the drops may have become smaller in size, the decreased updraft was unable to suspend them. As N_{CCN} increases further, w_{peak} increases sharply and precipitation decreases strongly. The dependence of w_{peak} on N_{CCN} is discussed in the following section.

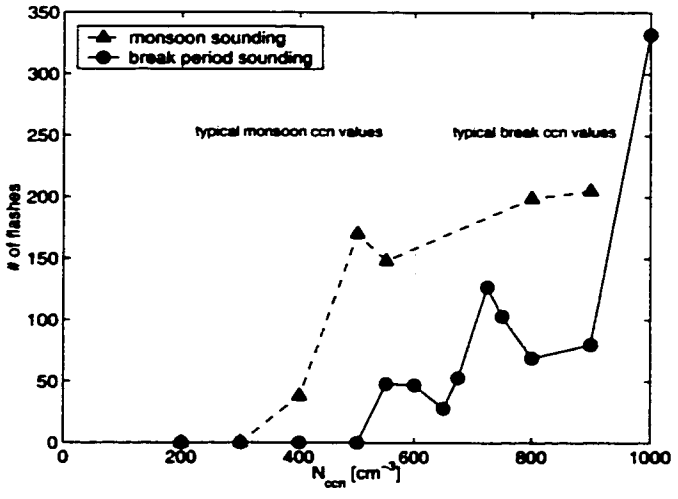

Figure 6.5: Model results of the total number of lightning flashes as a function of N_{CCN}. In these model runs soundings of monsoon and break type were combined with N_{CCN} values more typical of break and monsoon storms, respectively.

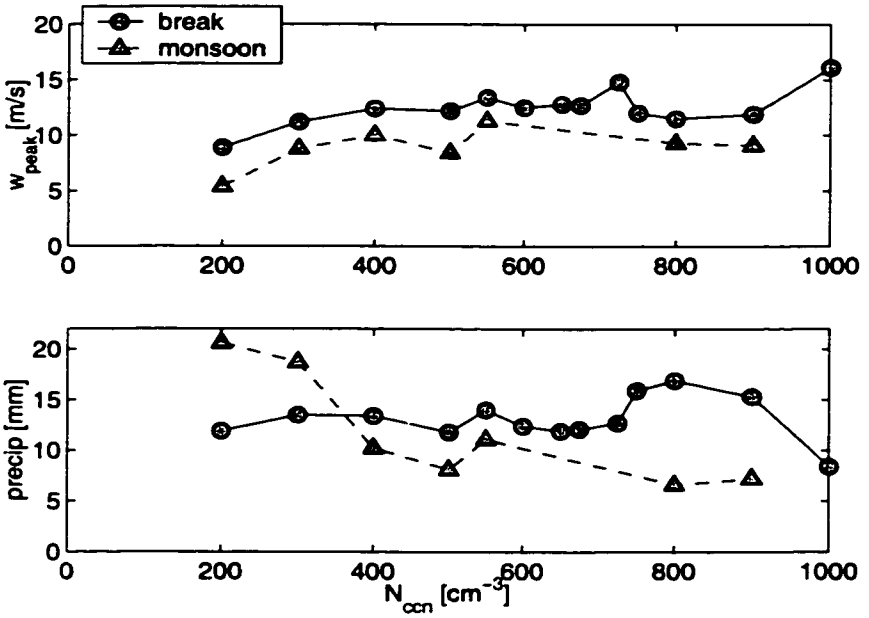

Figure 6.6: Model results of peak updraft velocity at the -10°C level (upper) and precipitation at cloud base (lower) as a function of N_{CCN} for monsoon and break model runs with a full range of N_{CCN}.

Separating the effects of cloud base forcing and N_{CCN} on flash rate

We have hitherto only considered the effect of N_{CCN} on lightning flash rate. However, there are a large number of other cloud parameters that directly or indirectly affect lightning flash rates.

In addition to N_{CCN}, cloud base forcing (w_{cb}) has an important indirect effect on lightning flash rates and should also be considered. Due to the limited observations available from the Brazil field study we have no information regarding the cloud base forcing there. The Williams *et al.* (1999) results in Fig 6.4a show a large amount of scatter and we speculate that variations in w_{cb} may account in large part for this scatter.

Dimensional analysis by Baker *et al.* (1995), indicate that lightning flash rate F is dependent on:

$$F \propto w_{peak}^{6} \tag{6.3}$$

and Solomon (1997) found that F depended on ice and water concentrations in the charging zone. In order to understand variations in flash rate we must then consider how changes in both N_{CCN} and w_{cb} affect peak updraft velocity (w_{peak}) and ice and water mixing ratio ($q_{water+ice}$) in the charging zone. The interactions between these various parameters are complex and will be discussed in the remainder of this section.

First we consider the availability of water in the charging zone. In the low N_{CCN} environments there are fewer condensation sites and the droplet size distribution is dominated by larger drops. Under these conditions much of the water rains out of these clouds before it reaches the charging zone (see Fig 6.7a). This then contributes to a reduction in cloud electrification and a resultant decrease in lightning flash rate. In the higher N_{CCN} environments, by contrast, the liquid water is shared among a large number of drops. These small drops are then able to reach the mixed phase region more easily, resulting in greater ice concentrations higher in the cloud and contribute to the cloud electrification process (see Fig 6.7b). We note that the ice formation process was dominated by primary ice nucleation (see section 6.2.3).

Increasing w_{cb} generally leads to higher updraft velocities in the cloud. These higher updrafts are capable of suspending larger drops and once again more water reaches the charging zone. Thus as both N_{CCN} and w_{cb} increase, according to the above, we expect to see increases in lightning flash rates.

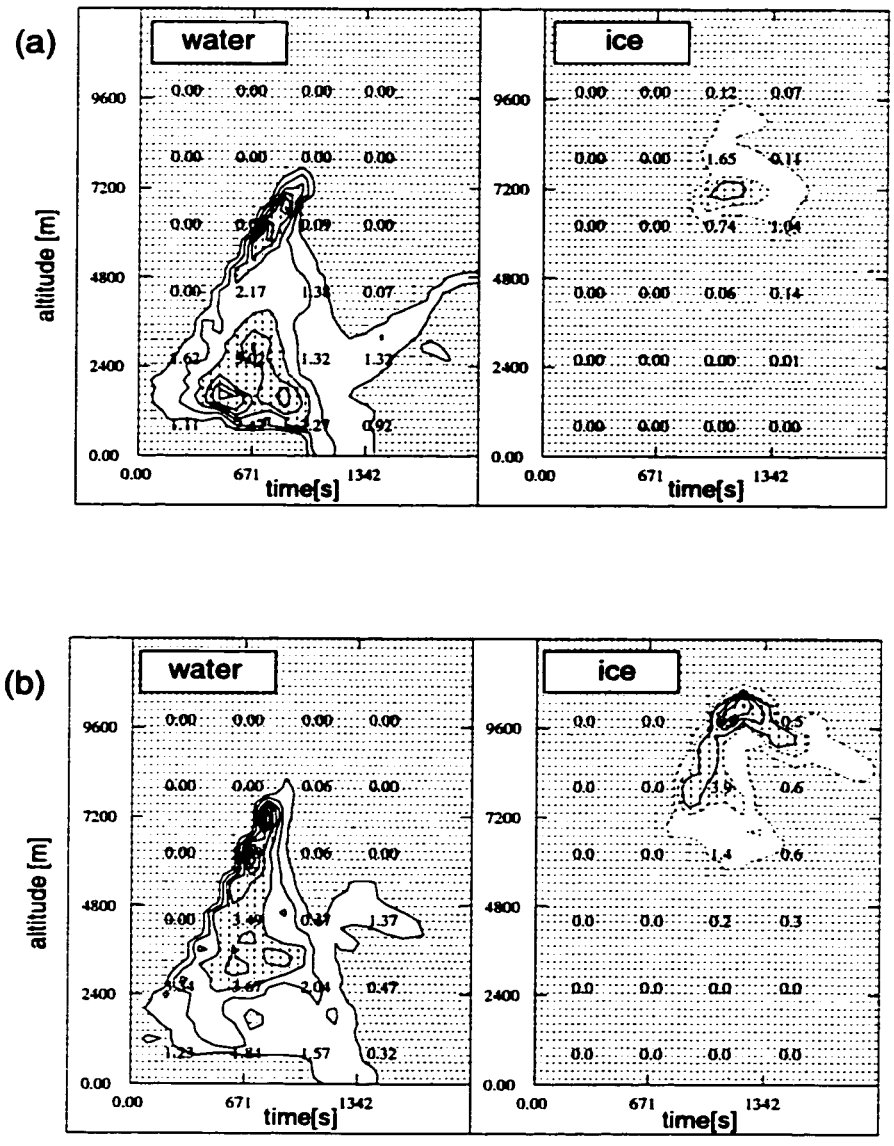

Figure 6.7: Water (left) and ice (right) concentrations [g/kg] as a function of model time [sec] and altitude [m]. The contour interval is 1 g/kg for the water plots and 5 g/kg for the ice plots. Contours above 3 g/kg are shaded (vertical hatching) in both water and ice plots. Both results used the 13 January 1999 environmental soundings as input. The upper figure (a) has $N_{CCN} = 600$ cm^{-3} while the lower figure (b) has $N_{CCN} = 1000$ cm^{-3}. It is clear that the lower N_{CCN} case (a) has higher water concentrations at lower altitudes than the high N_{CCN} case (b). By contrast, the high N_{CCN} case has more water in the mixed phase region (5000-8000m) and a significantly higher peak ice concentration (> 15 g/kg) than the low N_{CCN} case (~ 5 g/kg).

Fig 6.8 shows model results for lightning flash rate as a function of both N_{CCN} and w_{cb} for 13 January (break) and 18 January (monsoon). The peak flash rates (F_{peak}) are categorized as low (< 15 /min), medium ($15 - 25$ /min) and high (> 25 /min).

In the monsoon case increasing N_{CCN} for a fixed w_{cb} generally does lead to an increase in F_{peak} (Fig 6.8a). Likewise increasing w_{cb}, with N_{CCN} now fixed, also results in higher F_{peak} values. This same trend is also true in the break case at low and medium break values of N_{CCN} and w_{cb} (Fig 6.8b).

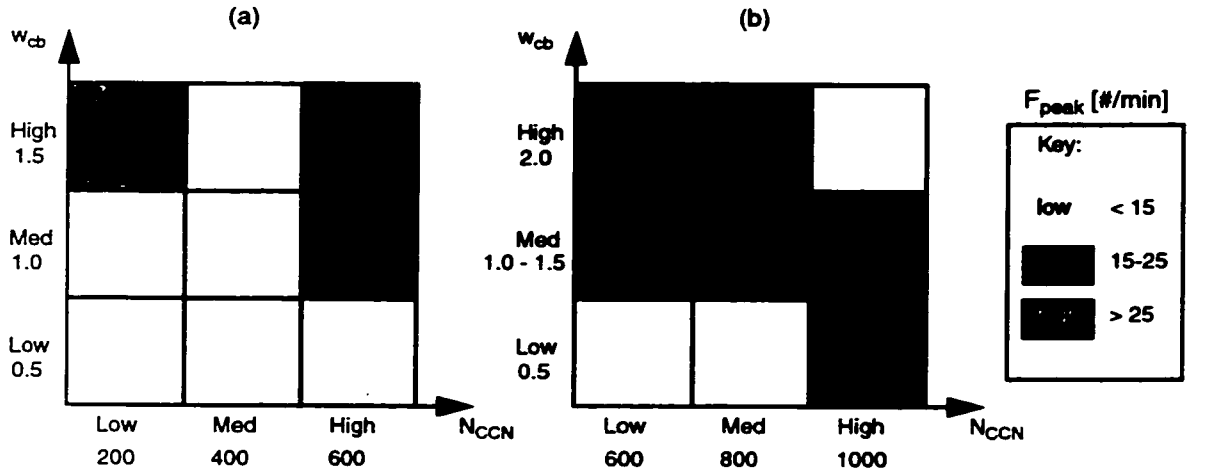

Figure 6.8: Peak lightning flash rate (F_{peak}) as a function of cloud base forcing (w_{cb}) [m.s^{-1}] and CCN concentration [cm^{-3}] for (a) 18 January (monsoon) and (b) 13 January (break) model runs.

However, there were some exceptions to these trends. At the higher N_{CCN} encountered in the break case we see that F_{peak} decreases sharply when w_{cb} is increased from medium to high values (Fig 6.8b). Likewise with w_{cb} held fixed at 2 m.s^{-1} an increase in N_{CCN} from 800 to 1000 cm^{-3} leads to a reduction in F_{peak}.

In order to understand this drop in F_{peak} we consider the peak updraft velocities in the charging zone (i.e. at the -10°C level). Fig 6.9 is similar to Fig 6.8 where the shading now represents $w_{peak}(-10°\text{C})$.

At first glance it would seem that increased w_{cb} should lead to increased w_{peak} values. This trend is true for the medium N_{CCN} case in Fig 6.9. However, in the low and high N_{CCN} cases we see that w_{peak} decreases at high w_{cb} values. We believe that this trend can be explained by including two

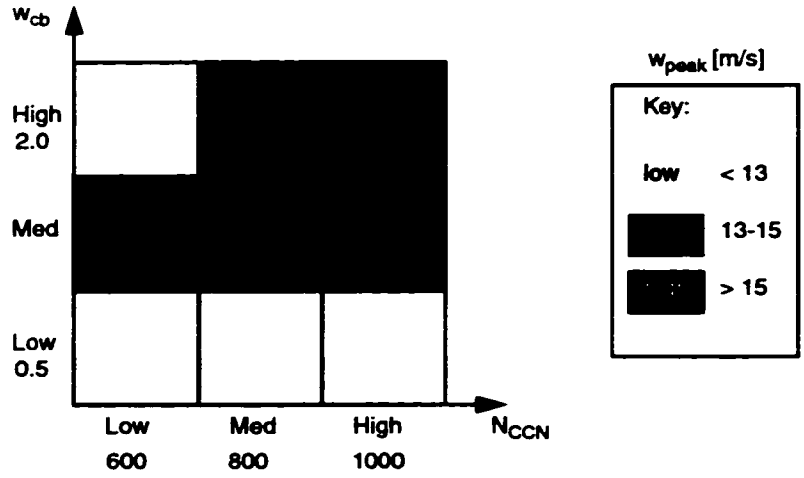

Figure 6.9: Peak updraft velocity (w_{peak}) in the charging zone as a function of cloud base forcing [m.s^{-1}] and CCN concentration [cm^{-3}] for 13 January model runs.

additional effects on the cloud dynamics: precipitation loading and entrainment.

For low N_{CCN} the lack of condensation sites leads to more large precipitation particles. The updraft is then unable to support these drops and as they fall out of the cloud they cause a drag which reduces the updraft. The friction drag by the hydrometeors results in a negative acceleration of $-gq_h$ where q_h is the total mixing ration of all hydrometeors (water and ice).

The reduction in $w_{peak}(-10^oC)$ is not as visible at lower w_{cb} values because large particles fall out before reaching the charging zone and most of the resultant drag occurs below the level of the charging zone. This has a less direct effect on the updraft velocity in the charging zone.

At higher values of N_{CCN} the drop size distribution is dominated by smaller drops and precipitation loading becomes a less important factor. Fig 6.10 shows the time integrated precipitation [mm] at cloud base with $w_{cb} = 2$ m.s^{-1} and increasing N_{CCN}. We notice that the curve is steepest for the $N_{CCN} = 600$cm^{-3} case with the slope decreasing as N_{CCN} increases (Fig 6.10a-c). A steep curve indicates that the accumulated precipitation at cloud base increased rapidly within a short time period. Thus the precipitation loading effect is compressed into a short time and in this case the vertical velocity is reduced significantly during the growth phase of the cloud. A more constant accumulation of precipitation (Fig 6.10c) does not have the same dramatic effect on vertical veloc-

ity. Vertical velocity is reduced more uniformly throughout the lifetime of the storm and thus there is less reduction during the growth phase.

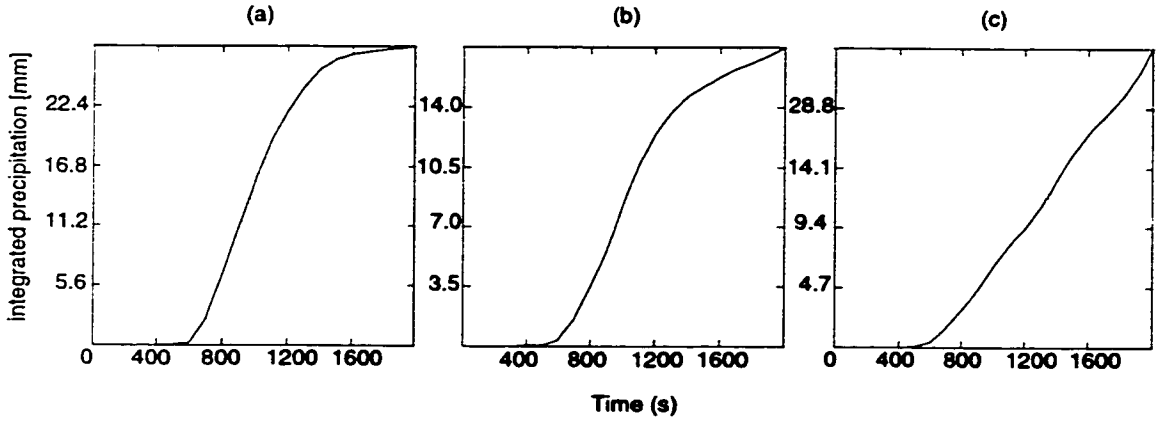

Figure 6.10: Time integrated precipitation [mm] at cloud base in 13 January (break) runs with $w_{cb} = 2\text{m.s}^{-1}$ and (a) $N_{CCN} = 600\text{cm}^{-3}$, (b) $N_{CCN} = 800\text{cm}^{-3}$, and (c) $N_{CCN} = 1000\text{cm}^{-3}$.

This leaves the question of why w_{peak} decreases at high values of N_{CCN} and w_{cb} (Fig 6.9). We speculate that in this case the increase in entrainment associated with the high w_{cb} value leads to increased evaporation. Note the decrease in the water and ice concentration in Fig 6.11(b) as compared to Fig 6.11(a). The evaporation results in cooling which decreases the buoyancy. The evaporation rate is faster at high N_{CCN} values where the drop size distribution is dominated by small drops which evaporate more rapidly than large drops. In addition, small drops are more likely to evaporate completely. This loss of water in the charging zone also contributes to reduced charging. The lower F_{peak} we see at high N_{CCN} and w_{cb} in Fig 6.8a is thus consistent with the decrease in both w_{peak} and water and ice concentrations that we see in the model results in Fig 6.11.

Glaciation parameterization sensitivity

The model includes a number of different glaciation mechanisms (see Section 5.3.3). We tested the sensitivity of the modeled flash rates to differences in both the primary and secondary ice production parameterizations.

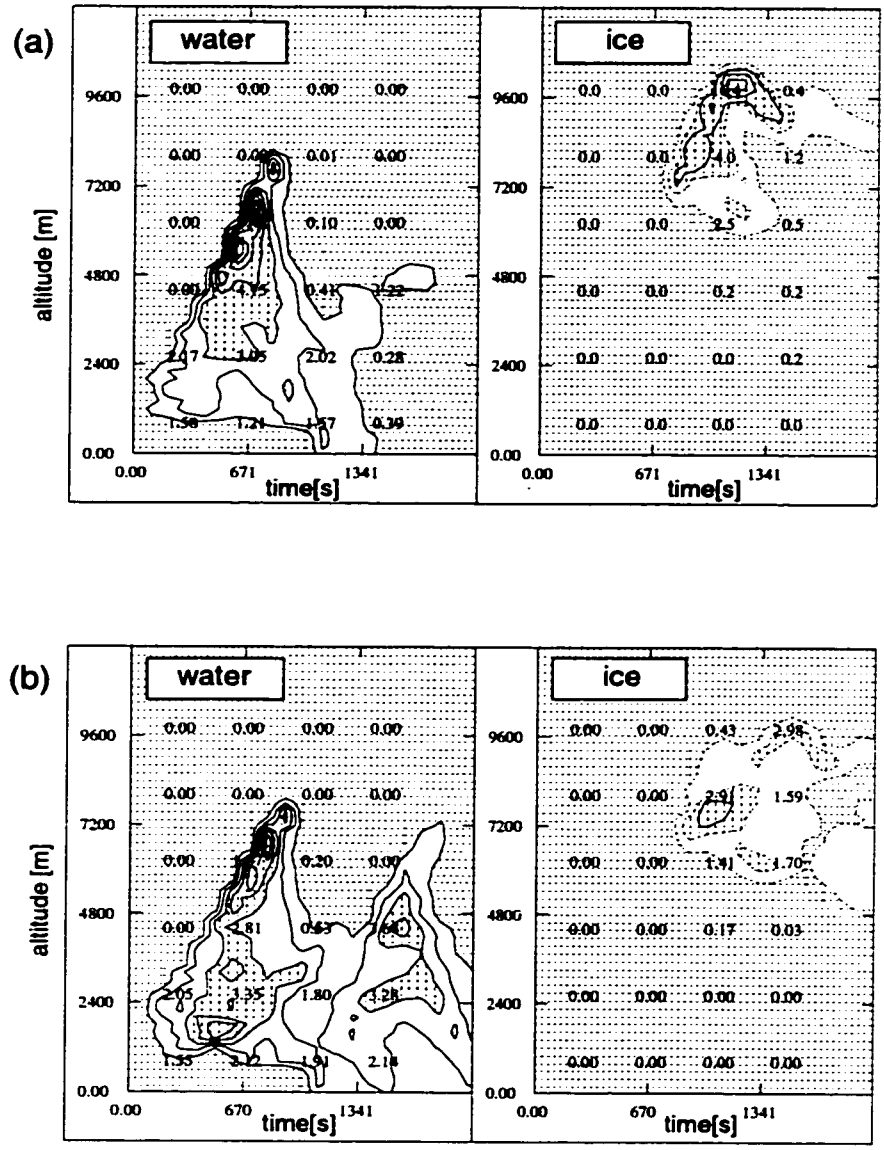

Figure 6.11: Water (left) and ice (right) concentrations [g/kg] as a function of model time [sec] and altitude [m]. The contour interval is 1 g/kg for the water plots and 5 g/kg for the ice plots. Contours above 3 g/kg are shaded (vertical hatching) in both water and ice plots. Both results used the 13 January 1999 environmental soundings as input. The upper figure (a) has $w_{cb} = 1.5$ m.s^{-1} while the lower figure (b) has $w_{cb} = 2.0$ m.s^{-1}. Case (b) has lower liquid water content in the mixed phase region (5000-8000m) and also significantly lower peak ice concentration than case (a).

Fletcher (1962) and Meyers *et al.* (1992) are the two primary glaciation parameterizations available for use by the model (see Chapter 5). For the majority of the model results in this Chapter the glaciation parameterization was set to Fletcher. We did, however, consider the effects of the Meyers parameterizations on flash rates. In general, we found that using the Meyers parameterizations led to more lightning and higher ice concentrations at lower altitudes. The increased lightning production is consistent with the enhanced ice concentration in the mixed phase region. Variations in lightning flash rate as a function of w_{cb} and N_{CCN}, however, followed the same trends regardless of which glaciation parameterization was used.

In addition, we tested the effect that secondary ice production (Hallett-Mossop mechanism, see Chapter 5) had on flash rates. Solomon (1997) found that when the Hallett-Mossop mechanism was activated the number of lightning flashes increased by $\approx$ 10-20% in storms where conditions were favorable for the formation of secondary ice particles by this mechanism. For the Brazil storms we found that the flash rates did not differ markedly between model runs in which Hallett-Mossop secondary ice production was active and in those for which it was turned off. Water and ice concentration profiles also showed little change when secondary ice production was turned off. This indicates that in the Brazil conditions secondary ice production is not a significant source of ice. The Hallett-Mossop mechanism is active between temperatures of -3^o and -8^oC and requires the presence of rimed ice particles (Hallet and Mossop, 1974). In the Brazil storms modeled here the -8^oC isotherm is located at approximately 6000m in altitude. As illustrated by Figures 6.7 and 6.11 the Brazil storms produced little or no ice below 6000m.

6.2.4 Summary of Brazil–N_{CCN} study

We briefly summarize the results of our Brazil-CCN study.

- Both the Williams *et al.* (1999) observations and our model studies show that F_{peak} is sensitive to N_{CCN} and in general increased with increasing N_{CCN} but with considerable scatter. This result suggests that flash rate parameterizations should include a N_{CCN} dependence.

- We found, in agreement with Molinie and Pontikis (1995), that the magnitude of CAPE alone cannot be used to predict lightning activity. In section 6.2.3 we saw that low CAPE and high

N_{CCN} can produce more lightning than high CAPE and low N_{CCN}. Thus our results suggest that N_{CCN} should be considered when attempting to predict lightning activity.

- Cloud base forcing is another important parameter. For the ranges of w_{cb} and N_{CCN} used in this model study, w_{cb} is the slightly dominant parameter of the two. The respective sensitivities of F_{peak} to w_{cb} and N_{CCN} are:

$$\frac{d\,ln(F_{peak})}{d\,ln(w_{cb})} = 0.64 \qquad \frac{d\,ln(F_{peak})}{d\,ln(N_{CCN})} = 0.59 \tag{6.4}$$

- secondary ice production was not an important source of ice production in these storms

The observational data in the Brazil study were quite limited. We would have benefited greatly from additional data such as in-situ observations of water and ice concentrations and electric fields. Dual Doppler radar data, which can be analyzed to obtain vertical velocities, would also have been very useful, enabling us to verify the model w_{peak} values.

6.3 Case Study II: Southern African Oceanic Lightning

As discussed in section 6.1 there are some notable exceptions to the high land/low ocean lightning activity contrast. Areas with anomalously high lightning activity have been observed, via satellite, in the oceans east of Southern Africa, Australia and North America (Fig 6.12). Due to the inaccessibility of these regions most of the data is acquired remotely via satellite. We have attempted to put together several datasets to explore the region off Southern Africa (see Fig 6.13).

The Southern African region lies directly in the path of the *Natal plume* which transports particle laden air off the continent and eastwards out across the Indian Ocean. The Natal plume activity is largely associated with the occurrence of semi-permanent subtropical anticyclones (continental highs) situated over the Southern African interior (Tyson *et al.*, 1996). During anticyclonic conditions 75 % of the air in the 1000 to 500 mbar layer over Southern Africa exits over the Indian Ocean while the remaining 25 % exits over the Atlantic. Over the Indian Ocean (at a longitude of 35°E) the Natal plume is located at a latitude of approximately 31°S and pressure $\approx$ 700 mb (Tyson and D'Abreton, 1998). Figure 6.14 is a schematic showing the approximate height of the plume as it moves off the coast and out over the Indian ocean. The air spends an average of about 4 days over

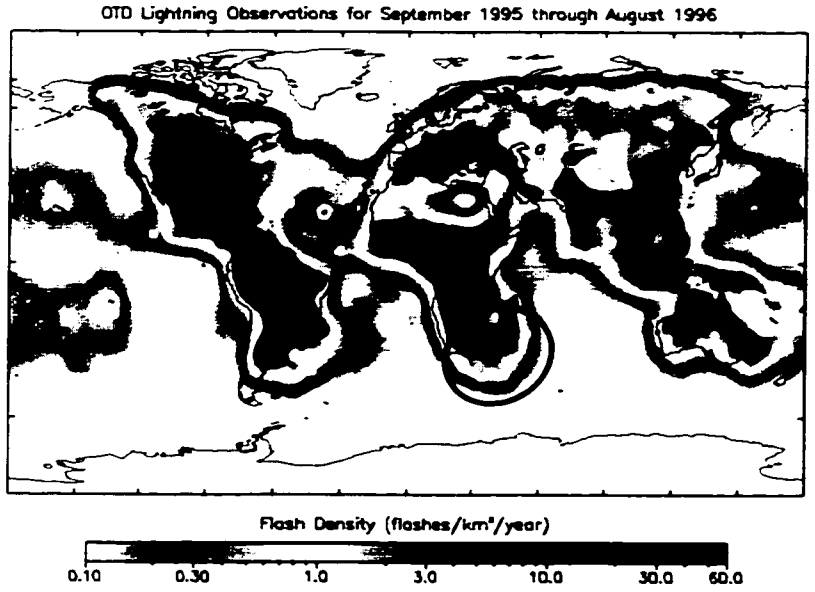

Figure 6.12: Optical Transient Detector lightning data showing several oceanic areas that exhibit anomalously high lightning activity. The map shows the flash density [#/km^2/year] for a one year period. The Southern African region, on which our study focuses, is indicated. Here the flash density exceeds 3 flashes/km^2/year. Data obtained from http://thunder.msfc.nasa.gov/

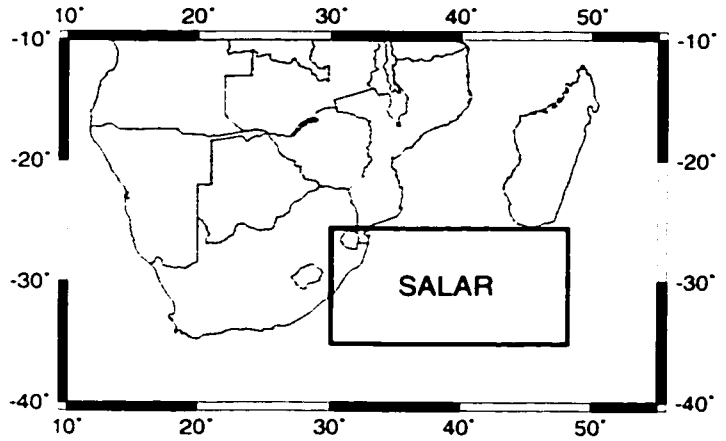

Figure 6.13: Map of southern Africa. The region in which anomalously high lightning activity is observed is indicated. This region will be referred to as the Southern African Lightning Anomaly Region (SALAR).

land before crossing the coast and heading eastwards. The air rises as it moves eastwards reaching a level of 500 - 400 mbar at 70°E.

The Natal plume is homogeneous, approximately 1500km in width and several kilometers deep. The main source is the African haze layer over the southern African plateau where aerosol concentration can reach very high values (up to $\approx$ 10000 cm^{-3}, Tyson and D'Abreton (1998)). During continental high conditions there is little precipitation and thus no wet deposition of aerosols occurs. Unfortunately little is known about the seasonal migration of the plume pathways.

The volume flux of the Natal plume is approximately 7.3×10^5 m^3/day. Combining this with the mean aerosol mass concentration, based on measurements made during the Southern African Fire Atmosphere Research Initiative (FIRE), Tyson *et al.* (1996) estimate the annual mean mass flux through 35°E as a function of circulation type (Fig 6.15a). The largest mass flux (32 Mtons/year) occurs when continental high pressure systems prevail, with this circulation type dominating over the others (ridging highs, easterlies and westerlies). The total mass flux (45 Mtons) is approximately one third of the North African plume's mass flux into the North Atlantic.

The frequency of occurrence of these continental high pressure systems peaks during Southern winter and has its minimum during Southern summer (Fig 6.15b). In winter plumes are likely to occur on more than 70% of days while in summer plumes occur on less than 20% of days (Tyson *et al.*, 1996). Satellite observations in this region show that the lightning activity follows the same pattern (see Fig 6.15c).

The object of this study is to determine which environmental properties may account for the anomalously high lightning activity (> 3 flashes/km^2/year) in the ocean off the east coast of Southern Africa. For the remainder of this Chapter we will refer to this area as the Southern African Lightning Anomaly Region (SALAR) and define it as the area of ocean encompassed by $25^o - 35^o$S and $30^o - 48^o$E.

We have compiled satellite data from a number of sources to look at:

- details of lightning activity within the region,
- sea surface temperature,
- cloud fraction, and
- cloud top temperature

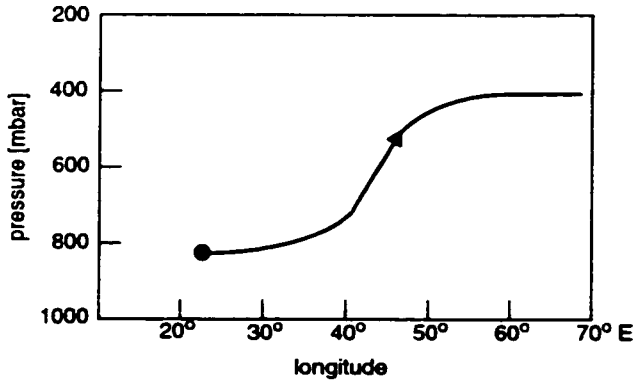

Figure 6.14: Schematic showing the vertical development of the Natal plume as it moves away from the east coast of South Africa. The coast lies at approximately 30°E. From Tyson and D'Abreton (1998).

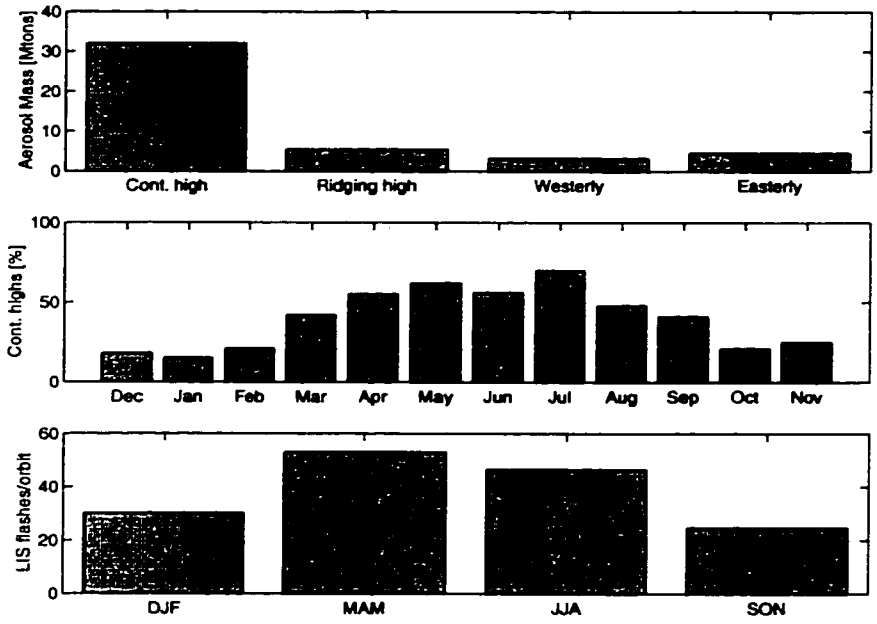

Figure 6.15: (a) Mean annual mass flux through 35°E as a function of weather systems over the southern African continent (Tyson *et al.*, 1996), (b) Frequency of occurrence of continental highs as a function of month (Tyson *et al.*, 1996), (c) LIS lightning data (flashes per orbit) as a function of season. Data obtained from http://thunder.msfc.nasa.gov/. The LIS lightning activity follows the same seasonal pattern as the occurrence of continental highs.

in additional to the suggested aerosol concentration information that we have from the Natal plume studies discussed above.

6.3.1 Satellite data analysis

LIS data

Lightning Imaging Sensor (LIS) data for a one year period (Dec 1997 - Nov 1998) were analyzed within the SALAR to show the average number of flashes per observed storm (Fig 6.16). The LIS lightning data were compiled from 361 separate orbits with the TRMM satellite, on which the LIS instrument is mounted, passing over the SALAR approximately once a day. See section 5.2 for instrument details.

LIS data contains a data field known as 'areas' which groups together one or more flashes into an area that roughly correspond to an individual thunderstorm. The number of flashes recorded within each 'area' or storm is recorded. We then compiled this information as a function of latitude and longitude (using a resolution of $2^{o} \times 2^{o}$) for each season. The seasonal timescale was chosen to avoid introducing any diurnal bias (see Chapter 5).

We found a region south of Madagascar that had distinctly higher numbers of flashes per storm than any of the surrounding areas. The region is roughly defined by a $5^{o} \times 7^{o}$ area bounded by 27°S - 32°S and 41°E - 48°E and will be referred to as the high flash region (HFR) hereafter (see Fig 6.16). In the HFR the number of flashes per storm exceeds 10 while in the surrounding regions values of $4 - 9$ are more typical. The high lightning activity in this region has been present in each year of the satellite lightning data (since 1996).

Sea surface temperature

Sea surface temperature (SST) data are available from the NOAA/NASA AVHRR Pathfinder project which consists of 5-channel Advanced Very High Resolution Radiometers on 4 polar orbiting satellites. The detectors have 9 km resolution. We examined SST data in the SALAR during a one year period. Sea surface temperatures are relatively uniform along east-west transects (within a couple of °C) but there is a reasonably sharp latitudinal gradient in SST, $\sim 4 - 5^{o}$C over $1 - 2^{o}$ latitude, that moves in a north-south sense with the seasons. The gradient retreats north to the latitudes of

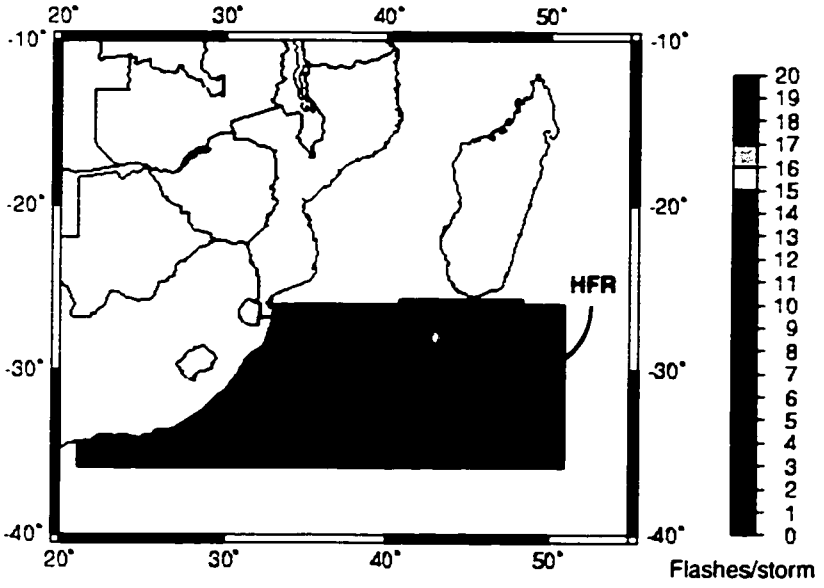

Figure 6.16: LIS data for a one year period (Dec 1997 - Nov 1998) in the South African Lightning Anomaly Region (SALAR). The data show the average number of lightning flashes per storm measured by the LIS detector. Within SALAR there is an area with flashes/storm > 10, indicated by the red box and referred to as the HFR or high flash region.

southern Madagascar during southern winter and moves as far south as the southern coast of South Africa during southern summer (Fig 6.17). These data suggest then that the high winter time lightning activity cannot be attributed to high SST in the SALAR. In particular, the HFR (Fig 6.16) also cannot be attributed to a localized region of high SST.

Cloud fraction

We next considered cloud fraction in this region. We obtained monthly cloud fraction data from the International Satellite Cloud Climatology Project (ISCCP). ISCCP compiles data from radiometers on a large number of satellites and process this data to give more useful products such as estimates of total cloud fraction as well as high cloud fraction with a 2.5° × 2.5° resolution. Details on the algorithms used to process the raw data can be found at:
http://www2.ncdc.noaa.gov/docs/isccp/cover.htm.

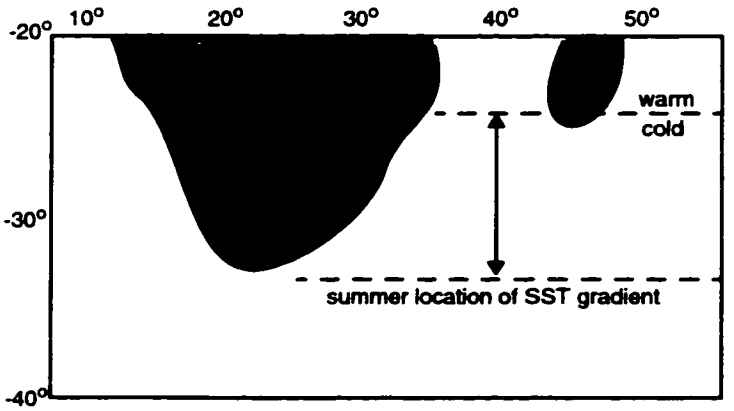

Figure 6.17: Schematic showing the seasonal movement of the latitudinal SST gradient off eastern South Africa. Based on monthly SST data from the AVHRR Pathfinder detector.

We studied the monthly variations in total, and high, cloud fraction over a 3 year period in the SALAR. Again we found that the SALAR could not be clearly distinguished from the surrounding areas based on either total or high cloud fraction. This was also true for the HFR.

In southern summer the high cloud fraction in SALAR reaches values of $30\% - 40\%$ while during winter values are typically lower at $0\% - 20\%$. Thus the high cloud fraction is low when lightning activity is high.

Cloud top height

We then examined the hypothesis that cloud tops might be higher in the study region since Price and Rind (1992) reported a correlation between cloud top height and lightning flash rates. Fig 6.18 shows data taken by the Visible Infrared Radiation Scanner (VIRS) on the TRMM satellite of the annual averaged mean cloud top height along with the standard deviation from the mean during 1998. Since both the LIS and VIRS detectors are aboard the TRMM satellite, the cloud data and lightning data are recorded simultaneously. In Fig 6.18 we see that cloud top heights were not, on average, very high in the SALAR and that the deviation from the mean was not large. There is also no indication that cloud top height was different in the HFR.

Monthly mean cloud top data also showed no evidence that there was a strong correlation be-

tween cloud top height and lightning flash rate. While the number of LIS observations is limited the HFR was a consistent feature and was present during three of the four seasons in 1998. If the cloud top heights were consistently high in the HFR we believe that monthly cloud top height data (covering the same period) together with the deviation from the mean would show evidence of these high cloud tops.

6.3.2 Summary of the SALAR study

- Based on the information presented above we thus speculate that the enhanced lightning activity in the SALAR may be in part the result of enhanced N_{CCN} values brought to this region during the winter months by the Natal plume. Ideally we would like in the future to correlate weather patterns and Natal plume activity in this region more directly with lightning activity.

- We have not been able to discover what causes of the high lightning flash rates within the HFR. It is possible that this is a region directly in the path of the plume at a time when it is moving to higher levels (Fig 6.14). This could result in more CCN being available within the cloud. It is also important to establish whether this feature is persistent from year to year. LIS data from 1999 are now available and should be analyzed in the future.

6.4 Discussion

The results from the Brazil and Southern Africa studies both suggest that N_{CCN} is a non-negligible factor in controlling lightning flash rates. It is possible that the disparity between ocean and land lightning activity may, at least in part, be a result of differing CCN concentrations in these two regimes rather than a specifically marine/continental effect. Thus when 'clean' air over oceans is polluted and CCN concentration is increased, lightning activity over these regions is enhanced. It is also possible that increased N_{CCN} due to urban pollution may lead to increased lightning activity.

The model results in Section 6.2 indicate that increasing N_{CCN} in 'clean' environments leads to enhanced lightning activity but that further increases in N_{CCN} in already 'dirty' environments in which large cloud base forcing is present could, in fact, lead to a decrease in lightning flash rates. This may explain the observed decrease in cloud-to-ground lightning in the U.S. southern plains

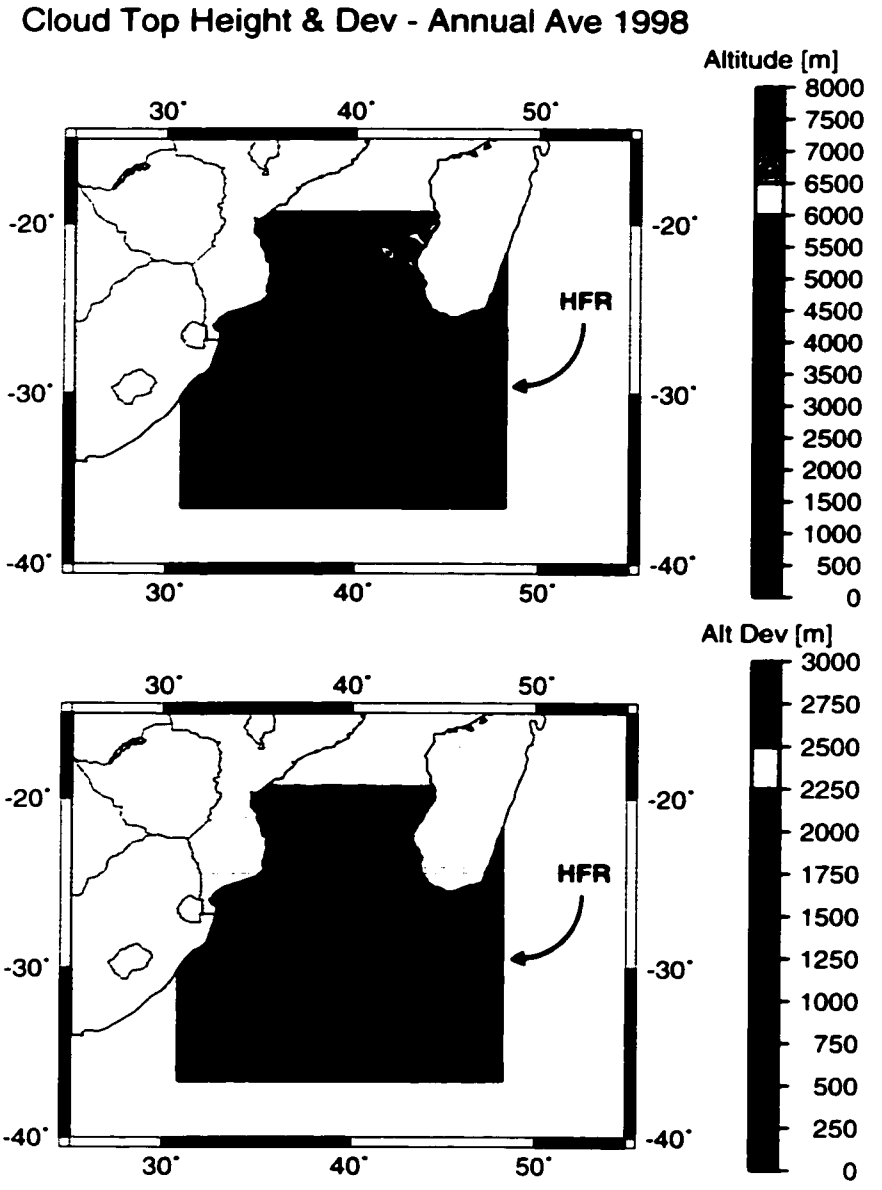

Figure 6.18: VIRS cloud top height data from the TRMM satellite. The top panel shows the annual mean cloud top height [m] off the coast of Southern Africa for 1998. The bottom panel shows the standard deviation from the mean [m]. The HFR is not apparent as a distinct region in the cloud top height data.

during the 1998 smoke intrusion (see section 6.1).

It is clear that this subject would benefit greatly from additional, detailed observational data. In the Brazil case study we had to rely on limited data and model runs in an attempt to establish the importance of the N_{CCN} influence on F_{peak}. Ideally such a study would compare thunderclouds in a given region before and during the intrusion of pollutants using remotely sensed flash rate, N_{CCN}, cloud base forcing, cloud updraft velocity and radar data that would allow us to confirm the validity of the trends we have determined from the model results. In-situ data such as electric field soundings and water and ice concentration would also be very useful.

In the Southern African case study we could only eliminate certain causes of the high lightning activity. While this implies that N_{CCN} is an important factor it is not conclusive proof. In this region we would certainly benefit from environmental soundings, *in-situ* N_{CCN} measurements, radar reflectivity and updraft data.

Chapter 7

Feasibility Study for Inferring Selected Thundercloud Properties from Satellite Lightning Data

7.1 Introduction

With the advent of new satellite lightning detection platforms it is important to investigate the potential use of the lightning data to provide information about other, hard to measure, cloud properties. In this study we have made use of *in-situ* observations together with numerical model studies to investigate correlations between:

1. lightning flash rate and updraft velocities in clouds, and

2. flash rate and convective water transport

The physical basis for the relationship between updraft velocity, condensate and lightning flash rate results from the charging process which takes place within the thundercloud (see Chapter 1).

In addition to a fundamental interest in knowing the nature of such relationships both these relationships have applications in other areas of atmospheric research. Flash rate - updraft relationships are used in atmospheric chemistry models in order to estimate the lightning source term of NO_x gases (Kraus *et al.*, 1996; Wang *et al.*, 1998; Lawrence *et al.*, 1995). Lightning is a non-negligible source term in the NO_x cycle and thus the global distribution of NO_x is controlled, in part, by the distribution of lightning. Atmospheric chemistry models do not include detailed lightning parameterizations and thus rely on using the magnitudes of vertical velocities in their models to predict lightning flash rates.

The ability to estimate the amount of water transported upward by large convective clouds might provide a missing piece in models of convective system water budgets (Gamache and Houze, 1983). Stratiform cloud regions are largely supplied by water from the upper reaches of convective clouds

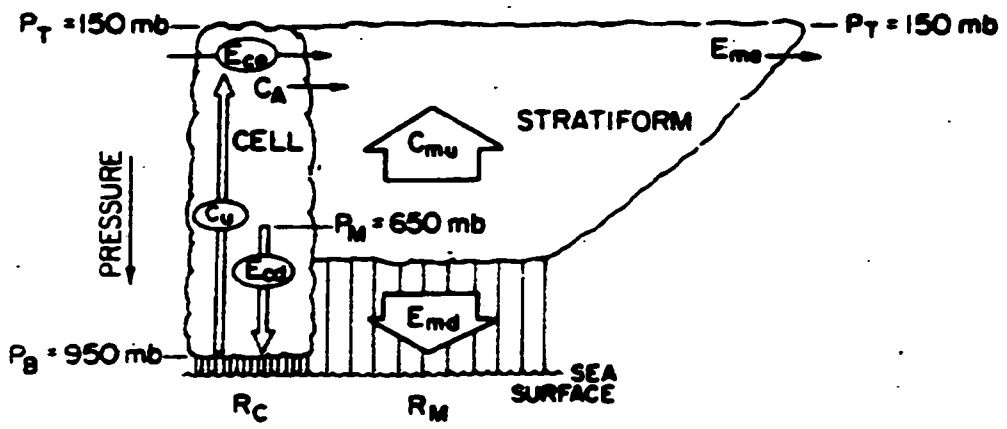

Figure 7.1: Schematic of convective and stratiform cloud water budget. From Gamache and Houze (1983).

(Fig 7.1) and thus knowledge of convective water transport would improve estimates of this source term.

7.2 Case Studies

We chose to focus on three climatic regimes with observational data provided from the following field projects:

- *tropical*: CaPE, Florida, 1991 (Bringi *et al.*, 1997)
- *island*: MCTEX, Tiwi Islands, Australia, 1995 (BMRC, 1995)
- *mid-latitude continental*: New Mexico, 1984 (Dye *et al.*, 1989)

All of these campaigns provide soundings that we could use for model input along with radar reflectivity and lightning data for model verification. In addition, mass flux analysis (Raymond *et al.*, 1991) is available for the New Mexico campaign and dual Doppler vertical velocities are available for the CaPE project - enabling improved assessment of the numerical model's performance.

Figure 7.2 provides a summary of cloud properties in the various regions. The average location of the -10°C isotherm - which marks the approximate base of the charging zone - is found between

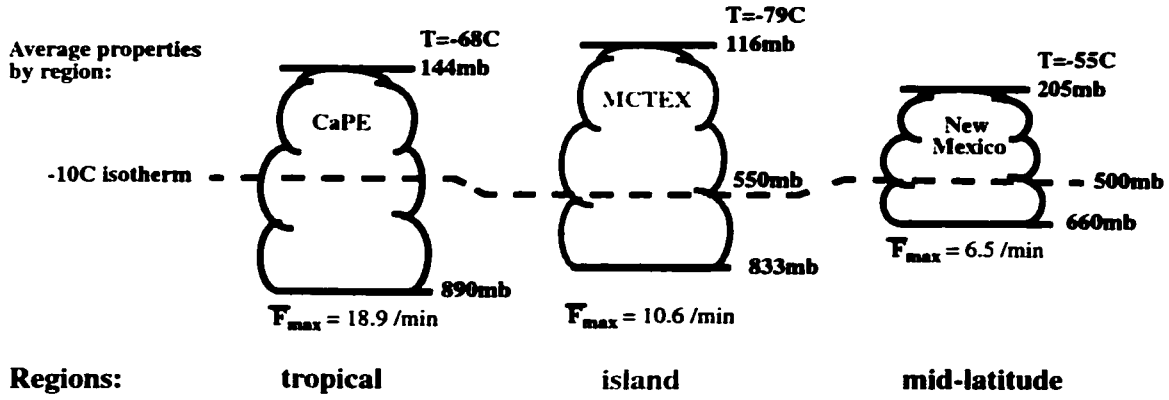

Figure 7.2: Schematic of case studies and average cloud properties in each region.

500 and 550 mbar in all three regions. However, it should be noted that the volume of cloud below the -10°C isotherm varies greatly, with the volume for the CaPE cases being the largest.

7.3 Model Validation

For each numerical thunderstorm model run we went through a verification process in order to ensure that the model was faithfully reproducing the main aspects of storms in that region. We considered various aspects of cloud development in an attempt to assess the model performance. Comparisons varied depending on the available observational data. In Table 7.1 we show a comparison of model and observations for a New Mexico storm. Here modeled maximum radar reflectivity at an altitude of 6km (MSL) at the time of cloud electrification compares well to the observed value as does the altitude of the 0 dBZ contour at this time. In addition, the total number of lightning flashes produced by the model storm is similar to the observed value.

The New Mexico storms had an additional set of observations that proved to be useful in assessing the model's performance. Raymond *et al.* (1991) made observations to determine the upward flux of air mass in several of the New Mexico storms. Figure 7.3 is a comparison of observed and modeled upward mass flux in altitude-time space for 3 August 1984. The model captures both the spatial and temporal developments of the storm well. The peak air mass flux occurs at an altitude of

Table 7.1: Comparison of model results to observational data for a storm observed on 3 August 1984 in New Mexico (IE = initial electrification).

	radar reflectivity IE, Z_{6km} [dBZ]	Z_{6km}(max) [dBZ]	# of flashes	z (MSL) of 0dBZ @ IE [km]	z_{max} of 0dBZ [km]
Obs.	40	43	6	9.5	12
Model	35-40	40-45	8	8.5	11

6km in both the model and observations. The model gives a maximum flux of 5 $kg.m^{-2}.s^{-1}$ after approximately 20 minutes as compared to an observed maximum of 6 $kg.m^{-2}.s^{-1}$ at about 1245. Time zero in the model roughly corresponds to 1230 in the observation time. Thus the peak flux in the observations occurs at approximately the same time as in the model.

The liquid water flux through the charging zone is an important parameter in the charge transfer process. Dye *et al.* (1989) made liquid water content (LWC) measurements at the altitude of the -12°C isotherm during the 3 August storm. They measured a LWC = 1 g/m^3 in the core of the storm's updraft. Combining this with the measured average air mass flux during the correspondence time period we obtain a liquid water flux of 4.6×10^4 kg/s. This compares well with a liquid water flux of 4.7×10^4 kg/s calculated by the model over an equivalent time period.

7.4 Results

7.4.1 Lightning and convective updraft velocities

Zipser (1994) hypothesizes that a threshold value for updraft velocities in convective storms exists, below which cloud electrification is too weak to produce lightning. He estimated that the threshold value for peak updraft velocity in the charging zone is $w_{peak} \sim 10$ $m.s^{-1}$. This was derived from the fall speeds of water and ice particles and the need for these particles to reach the charging zone. Detailed lightning flash rate and vertical velocity data were not available in the dataset that was utilized in this study.

The idea of a threshold is further supported by a dimensional analysis study by Baker *et al.*

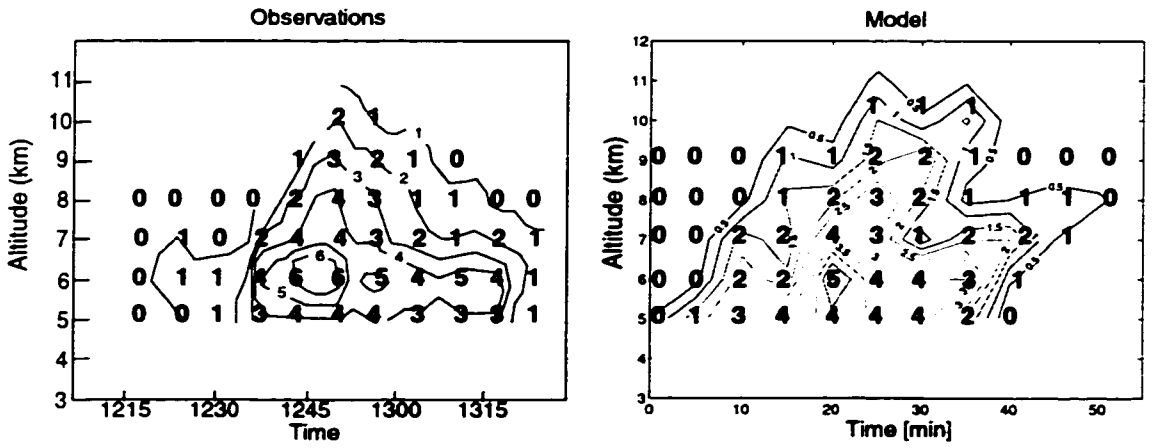

Figure 7.3: Air mass flux observations (left) from Raymond *et al.* (1991) for a 3 August 1984 New Mexico thunderstorm shown as a function of altitude (MSL) and time. On the right are the model results of air mass flux [kg.m^{-2}.s^{-1}] for a modeled storm initialized to the atmospheric conditions of 3 August 1984. The model captures both the spatial and temporal development of the storm reasonably well.

(1995) in which they found a high order dependence of flash rate (F) on updraft velocity (w) in the charging zone:

$$F \propto w^6 \tag{7.1}$$

This equation predicts an onset of lightning at roughly $w \sim 7 - 9$ m.s^{-1}.

Price and Rind (1992) (hereafter P&R) compiled data from a wide variety of sources to establish a relationship between cloud top height and the peak updraft velocities measured in continental storms. This relationship, together with previous data relating cloud top height and total lightning flash rate by Williams (1985), gave P&R the following relationship between total flash rate and w_{peak}:

$$F = 5.65 \times 10^{-6}\, w_{peak}^{4.5} \tag{7.2}$$

This relationship again suggests that a threshold value of $5 < w_{peak} < 10$ m.s^{-1} exists, above which the lightning flash rate increases rapidly.

Following the studies cited above, we made use of more direct measurements of vertical velocity and observed CG lightning made during the CaPE field campaign in Florida 1991 to determine the

relationship between these quantities. Figure 7.4 shows a cross-section, at 6km altitude, through a series of thunderstorm cells with vertical velocity contours shown. Superimposed on the velocity contours are the locations of CG lightning strikes. The vertical velocities were derived from dual Doppler radar data.

We defined the core of the cell as the region in which the vertical velocity was greater than +5 $m.s^{-1}$. The maximum updraft velocity within the core of each cell was determined for each time step. We then counted the number of lightning flashes that occured within each cell during the following 5 minutes. The results of this study are presented in Fig 7.5. Observations from the CaPE field project were augmented with results from our numerical thunderstorm model, based on a case study of a storm during the TOGA COARE project (Solomon and Baker, 1996). The CG flash rates in Fig 7.5 suggest the same high order dependence on updraft velocity as the P&R relationship (Eqn 7.2) - which is for total (CG + IC) flash rate - and seem to concur with Zipser's hypothesis of a threshold value in updraft velocity below which no, or very little, lightning is produced.

The lack of high flash rate data and the number of observations that have high updraft velocities but for which the CG flash rates are low or zero are probably a result of the fact that our data only included CG flashes. These cells may have had many IC flashes and thus looking at the total flash rate would give a more accurate picture. Furthermore, the satellite lightning detectors sample both IC and CG lightning. Much of the available lightning data, however, is only for CG lightning. To study the relationship between total lightning (CG + IC) and updraft velocity we analyzed model outputs from all three regions shown in Figure 7.2. The peak flash rates [#/min] were calculated by averaging over five minute time bins. We focussed on storms with F_{peak} greater than 5 per min. The peak updraft velocities attained at 6km altitude during each storm are plotted against F_{peak} (Fig 7.6). Again, the data suggest a high order dependence of F_{peak} on w_{peak}. A best fit of this data gave $F_{peak} \sim w_{peak}^{7}$, giving an updraft threshold of $\sim$ 10 $m.s^{-1}$ for lightning. This is also in good agreement with the relationship predicted by Baker *et al.* (1995).

The sensitivity of F_{peak} to w_{peak} varied somewhat on a regional basis. In Fig 7.7 we see that the updraft threshold value is higher for tropical storms (CaPE, MCTEX) than for mid-latitude storms (New Mexico). In addition, Fig 7.7 indicates that F_{peak} was most sensitive to changes in w_{peak} in the CaPE cases where small changes in updraft velocity resulted in a large increase in flash rate.

Figure 7.4: Cross section, at 6km MSL, through a series of thunderstorm cells in Florida (CaPE field project). Filled contours are of vertical velocity [m.s^{-1}] with CG lightning locations superimposed.

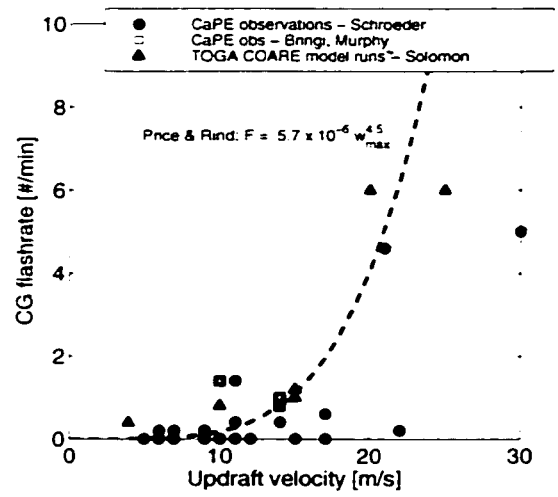

Figure 7.5: Observational data and model results of convective cell CG lightning flash rates as a function of updraft velocity at the charging zone boundary (-10°C). The dashed line, from Price and Rind (1992), shows the predicted variation in total (IC+CG) flash rate with updraft velocity.

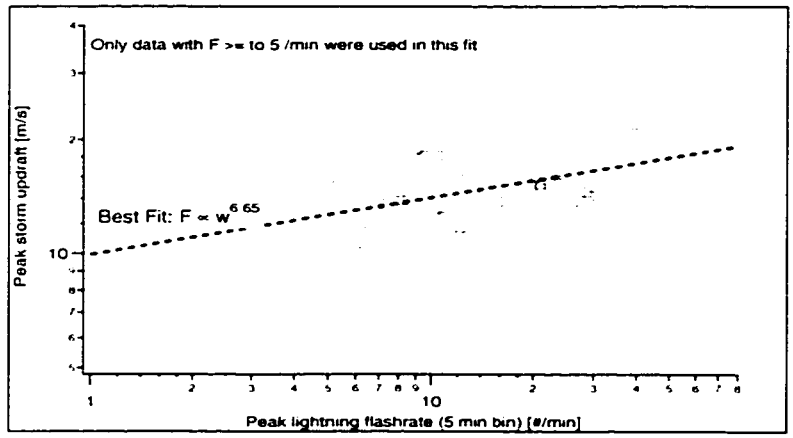

Figure 7.6: Peak updraft velocities as a function of peak lightning flash rates for numerically modeled thunderstorms that produced flash rates greater than 5 per minute. A best fit of the data shows that F_{peak} is very sensitive to w_{peak} with $F_{peak} \propto w_{peak}^{6.65}$.

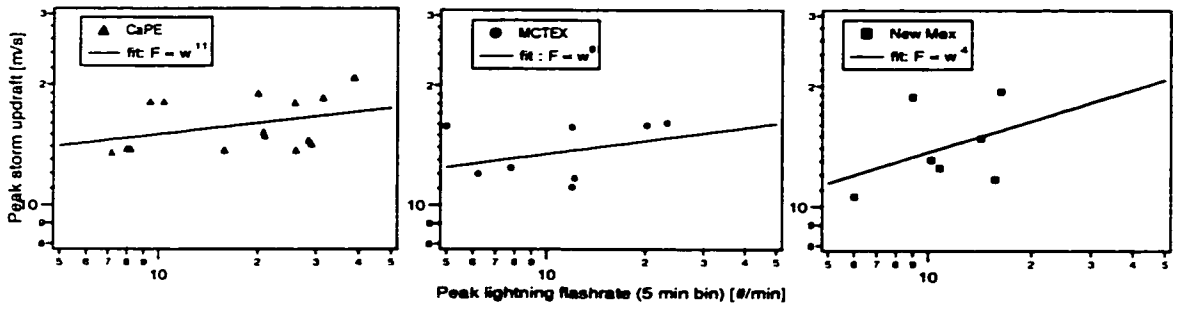

Figure 7.7: Regional sensitivities of peak lightning flash rates to peak updraft velocities in results from our numerical thunderstorm model. On the left, the CaPE flash rates are very sensitive to small variations in updraft velocity. The updraft threshold value is also largest for CaPE storms.

7.4.2 Lightning and convective water transport

As described in Chapter 1, the updraft velocity is only one of the important cloud properties governing the growth of the electric field - the presence of liquid water and ice are also required. The existence of threshold values in the amount of liquid water and ice entering the charging zone are illustrated in Fig 7.8 a & b; the results are from numerical thunderstorm model studies by Solomon and Baker (1998). A threshold value in the peak liquid water flux of $\sim$ 10 g.m^{-2}s^{-1} entering the charging zone is indicated in Fig 7.8a.

The ice crystal concentration also appears to have a strong influence on the lightning flash rate (see Fig 7.8b). The flash rate remains low ($<$ 10 min^{-1}) until the ice concentration enters the range $\sim 10 - 100$ l^{-1}, after which it rises rapidly.

This early model result appears to support the physical hypothesis that some minimum quantity of both water and ice are needed within the charging zone of convective cells in order to ensure electric fields large enough to produce lightning. Based on this early evidence we have proceeded with more detailed studies of the relationship between the lightning flash rate and water and ice masses lofted into the charging zone.

We define the total mass of condensate lofted into the charging zone (i.e. through the -10^{o}C isotherm) of a convective cell as:

$$C = \int_{lifetime} w \cdot \pi R^2 \cdot q_{water+ice} \cdot \rho_{air}\, dt \tag{7.3}$$

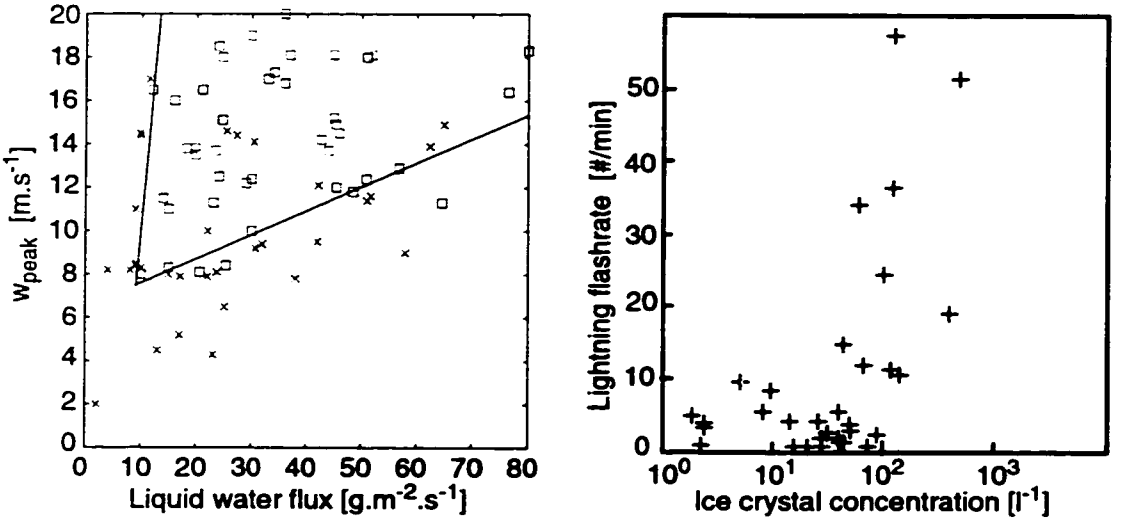

Figure 7.8: (a) Model data of maximum updraft velocity at the charging zone boundary as a function of the peak liquid water flux into the charging zone for lightning (squares) and non-lightning producing storms (x). The lower line represents the updraft threshold while the near- vertical line represents the liquid water flux threshold. (b): Model data of total lightning flash rate as a function of the ice crystal concentration in the charging zone. Figure (b) is from Solomon (1997).

where w [m.s^{-1}] is the average updraft velocity during each 100s in our model,

R [m] is the cell radius,

$q_{(water+ice)}$ [kg/kg] is the combined mixing ratio of ice and water

at the -10°C level, and

ρ_{air} [kg.m^{-3}] is the air density.

The integration is over the lifetime of the storm. We have found, from model studies, that most of the condensate is lofted shortly prior to (beginning $\sim$ 5 min before) and during lightning activity. This is consistent with polarimetric radar observations by Lopez and Aubagnac (1997). They estimated the mass of water, graupel and small hail between -10°C and -20°C (charging zone) and found that these masses peaked before, or early in, the period of lightning activity with the early and late stages of the cell contributing negligible amounts.

The active period is defined as the length of time during which lightning occurs in a convective cell. The average lightning flash rate of the storm, F_{ave}, is then defined as the total number of flashes

occurring in the cell divided by the active period of that cell. It should be noted that the values of flash rate determined using this method tend to be lower than flash rates often quoted in the literature - which are instantaneous flash- rates rather than averages over the entire active period.

By definition the condensate mass $C \approx w \cdot R^2 \cdot q(water+ice)$ while observations (Price and Rind, 1992) show that $F \approx w_{peak}^{4.5}$. In addition, Figs 7.8 a & b indicate that F is also linearly dependent on $q_{(water+ice)}$. Thus:

$$\frac{C}{F} \approx \frac{w_{peak} \cdot R^2 \cdot q_{(water+ice)}}{w_{peak}^{4.5} \cdot q_{(water+ice)}} \approx \frac{R^2}{w_{peak}^{3.5}} \tag{7.4}$$

(assuming we can replace w with w_{peak})

Fig 7.9 indicates that there is a relationship between the effective cell radius, R, and w_{peak} measured at the -10°C isotherm. The data includes vertical velocity data derived from dual Doppler radar as well as results from case studies using our numerical thunderstorm model. In our analysis of CaPE observational data we defined the cell area as the area over which $w > 5$ m.s^{-1}. The effective cell radius was then defined as the radius of a circular cell with equivalent area. Data from Bringi *et al.* (1997) and Lucas *et al.* (1994) appear to be consistent with our model results. There is definitely a positive correlation between R and w_{peak} - with a second order polynomial performing better than a linear fit of the data.

Using this $R - w_{peak}$ relationship in Eqn 7.4 together with P & R's $F - w_{peak}$ relationship, we obtain:

$$C \approx F^{1.1} \tag{7.5}$$

i.e. that C is approximately linear in F.

The values of C [kg] lofted into the charging zone and the corresponding lightning flash rates, F_{ave} , were obtained from our numerical model calculations for the 3 regions in Figure 7.2. We found, in agreement with the above analysis, that the relationship between condensate, C, and F_{ave} is approximately linear in each separate region (Fig 7.10). However, there are strong regional differences in this relationship.

Results from the New Mexico case studies show that C varies strongly with F_{ave} while in the MCTEX and CaPE cases, by contrast, there is negligible variation in C which remains in the range: $50 - 100 \times 10^6$ kg for all values of F_{ave}.

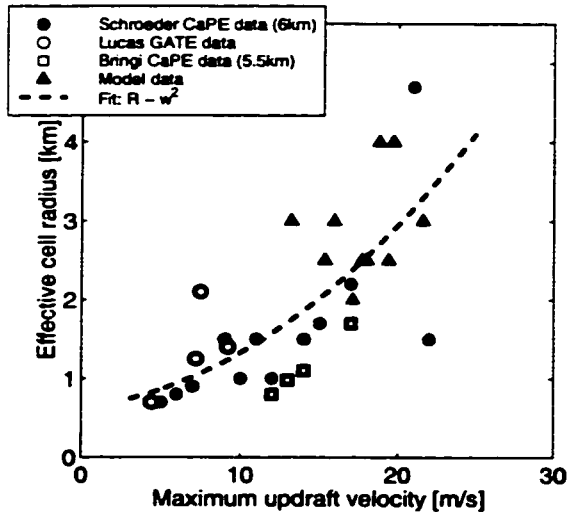

Figure 7.9: Effective convective cell radius [km] as a function of w_{peak} [m/s]. Observations (Doppler radar) are from CaPE 15 Aug 1991, CaPE 9 Aug 1991 (Bringi *et al.*, 1997) and GATE (Lucas *et al.*, 1994). Model data are from New Mexico case studies. A second order polynomial fit matched the data better than a linear fit.

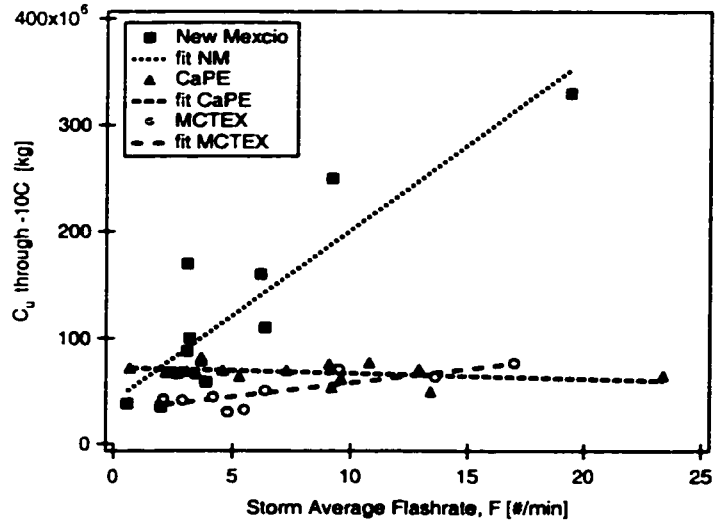

Figure 7.10: Condensate (C) [kg] lofted through the -10°C isotherm (into the charging zone) during the lifetime of modeled thunderstorms. The results show that the relationship between C and F_{ave} is approximately linear in each separate region. However, the slopes varied greatly. Results from the New Mexico case studies showed that a strong dependence exists between C and F_{ave} while in the MCTEX and CaPE studies F_{ave} displayed a weak dependence on C.

7.5 Discussion

7.5.1 Regional sensitivities

The schematic in Figure 7.11 summarizes the dependence of lightning production on storm updraft and water transport. The non-shaded area in $w_{peak} - C$ space indicates the w_{peak} and C value pairs in modeled storms that produced no lightning. The shaded areas indicate $w_{peak} - C$ combinations from lightning producing storms. As indicated $w_{peak} - C$ values were restricted to fairly narrow bands for each region.

CaPE storms gave lightning over a large range in w_{peak} values but a relatively narrow range of C values. In addition, CaPE storms that did not produce lightning all lay to the left of the *minimum C* line. This indicated that the absence of lightning can be attributed to a lack of water and ice within the charging zone. This is consistent with the cloud structure in this region. The CaPE and MCTEX storms have low cloud bases with large volumes of cloud below the -10^{o}C isotherm. Under these conditions the condensate can grow large and rain out before entering the charging zone, even when updraft velocities are quite high.

By contrast, the New Mexico storms, with their high cloud bases, have greater amounts of condensate entering the charging zone and have, on average, lower updraft speeds. New Mexico storms that failed to produce lightning were hampered by their low updraft velocities rather than a lack of condensate entering the charging zone. Once storm updrafts exceeded an updraft threshold and began to produce lightning it appears that variations in condensate supply to the charging zone then controlled the flash rate.

7.5.2 Applications

Condensate transport through the charging zone is clearly an important modulating factor in lightning flash rate. However, it does not seem feasible to use remotely sensed lightning data to make quantitative estimates of this quantity globally. The $C - F$ relationship varied widely across different climatic regions (Fig 7.11) and we do not feel that these relationships can be generalized with any high degree of confidence. In addition, while trends predicted by our simple numerical thunderstorm model have proved reliable in the past, the absolute values of condensate are definitely limited in accuracy by the simplicity of our model.

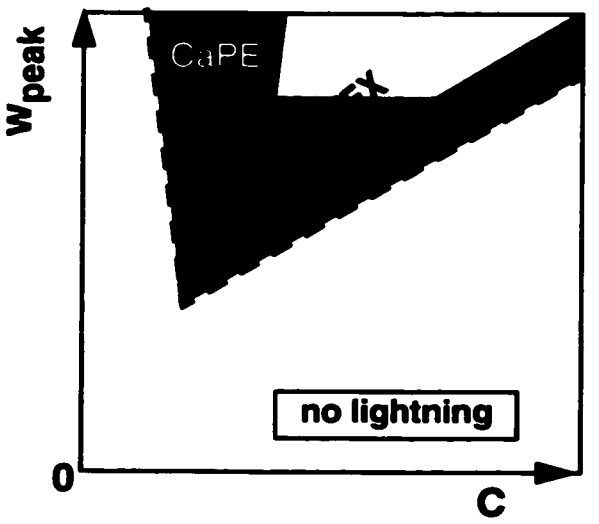

Figure 7.11: Schematic of relationships between the peak updraft velocity in the charging zone, w_{peak}, and the condensate lofted through the -10°C isotherm, C, for lightning and non-lightning producing storms in all 3 regions from model results.

Many atmospheric chemistry models make use of the P & R $F - w$ relationship to estimate lightning flash rates in their models. The P&R relationship distinguishes between continental and marine locations but all continental regions are represented by a single relationship. Our results indicate, however, that this relationship also varies significantly on a regional basis (fig 7.7). Since prediction of the global distribution of NO_x is the primary goal of many of these chemistry models, variations in the $F - w$ relationship by region will have an important impact on these results.

As we saw in the previous chapter, CCN concentration can also affect F_{peak}. It seems then that with so many parameters exerting a significant influence on lightning flash rate that it is not reasonable to use F as a proxy for any single parameter, or vice versa. This study suggests that local conditions dictate which parameters exert the largest influence on F. Thus models that use any one parameter to predict F risk making incorrect estimates of lightning distributions.

Chapter 8

Conclusions

In this thesis we have explored possible mechanisms for lightning initiation and considered which cloud properties exercise the most control over lightning frequency. Here we summarize the results presented in the preceding chapters.

8.1 Lightning Initiation

The electrical process by which lightning initiates remains a puzzle. The electric fields measured in clouds are an order of magnitude lower than the fields required for the electrical breakdown of air. We have investigated the two most commonly proposed mechanisms in an attempt to evaluate their respective merits. The hydrometeor mechanism relies on the enhancement of the large scale electric field in the vicinity of the hydrometeors while the runaway breakdown hypothesis suggests that high energy electrons, created in cosmic ray showers, multiply as they accelerate through the in-cloud electric field, resulting in the formation of a plasma region and an enhanced electric field outside this region.

As discussed in Chapter 4 we found that it was possible, if not probable, to initiate some form of breakdown in clouds with both the hydrometeor and the runaway breakdown mechanisms. It is important to note that the assessment of the relative probabilities of these two mechanisms relies heavily on measured in-cloud electric fields. Electric field profiles are made using instrumented balloons that take approximately 1 hour to ascend through the cloud. Thus, it is not possible to reliably know either the maximum electric field attained (especially if this field exists over only small distances) or the extent over which the electric field exceeds a particular value.

Until more accurate in-cloud electric field measurements are available it is not really possible to confidently choose one of these mechanisms over the other. Nor can we conclude that either of these mechanisms wholly solves the lightning initiation puzzle.

8.2 Lightning Frequency

If we can understand which cloud parameters control lightning frequency, F, and how they do so, we will be able to use this knowledge to both predict lightning activity based on cloud property information and to learn more about hard to measure cloud properties by looking at lightning flash rate data.

We have explored the relationships linking lightning flash rate to CCN concentration (Chapter 6), cloud updraft velocity (Chapter 7) and total water transported up through the charging zone of the cloud (Chapter 7) using a combination of observational data and model results.

We found that cloud condensation nucleus concentration (N_{CCN}) was a non-negligible factor in controlling lightning flash rate, with peak lightning flash rate increasing roughly linearly with increasing N_{CCN} in a given tropical sounding. We speculate that the anomalously high lightning activity observed in the ocean off the Southern African coast during southern winter is caused by an influx of 'dirty' (high N_{CCN}) continental air brought to this region by the Natal plume. Increased N_{CCN} values over and downwind of urban areas may also be an important contributing factor to observed increases in lightning activity in these regions.

Relationships between flash rate and updraft velocities in the literature have been derived by dimensional analysis and by combining relationships between flash rate and cloud top height and cloud top height and updraft velocity. Both methods indicate a high order dependence of peak flash rate (F_{peak}) on peak updraft velocity (w_{peak}). We made use of more direct lightning and vertical velocity measurements together with numerical modeling to study this relationship in more depth. We chose three distinct climatic regimes in our study. When we considered the results from all three regions together we found that $F_{peak} \sim w_{peak}^7$, with a threshold of $\sim 10\ \mathrm{m.s^{-1}}$, below which lightning was not observed. However, it is important to note that we found fairly significant variations in this relationship on a regional scale with the flash rates in the tropical location (Florida) being more sensitive to w_{peak} than F_{peak} in mid-latitude continental storms (New Mexico).

We also considered the feasibility of using lightning flash rate observations to give us estimates of how much water and ice (C) is lofted up through the charging zone during the lifetime of a storm. This is an important source term for water entering stratiform cloud regions. For the mid-latitude continental storms in our study we found a strong, roughly linear, relationship between the average

flash rate (F_{ave}) during the storm and C. In the other two regions our model predicted was only a weak relationship between these two quantities.

We thus conclude, due to the strong regional differences, that global satellite lightning flash rate data could not feasibly be used to make large scale estimates of vertical water transport without further understanding how regional factors lead to such different $C - F_{ave}$ relationships.

8.3 Recommendations for Future Work

As so often happens, this study has perhaps raised more questions than it has answered. Solving the lightning initiation puzzle is a fundamental problem that still requires much attention. Most urgently, improved electric field measurements in clouds will clarify a number of pressing questions regarding the magnitude and extent of these electric fields. Simultaneous observations of cosmic ray showers, runaway breakdown and lightning might help lend more credibility to the runaway breakdown hypothesis.

As we move from lightning initiation to the factors that control lightning flash rates we again see that our understanding could be greatly improved. I think we have come closer to narrowing down the most important parameters controlling lightning frequency but the exact relationship between F_{peak} and these parameters still eludes us. It is an important issue because there are currently a number of global models (e.g. atmospheric chemistry models) that parameterize lightning flash rates using, for example, w_{peak}. As we have shown this parameter on its own is not always a good proxy for lightning. Once again this work would benefit from more field data such as remotely sensed flash rate, N_{CCN}, cloud base forcing, cloud updraft velocity and radar data, together with in-situ water and ice concentration data.

We made use of direct observations whenever possible, but the scarcity of data meant that we had to rely heavily on our numerical thunderstorm model which is, of course, subject to its own set of limitations. The model is 1.5D which limits the reality with which the dynamics can be modeled. In addition, the threshold electric field for lightning initiation is pre-set in the model. This doesn't allow for the possibility that the initiation electric field threshold may depend on in-cloud properties and thus change during the lifetime of the storm. It is my hope that improved *in-situ* and remotely sensed data will allow us to improve on the work presented here in the near future.

Bibliography

Abdel-Salam, M., A. Zitoun, and M. El-Ragheb, Analysis of the Discharge Development of a Positive Rod-plane Gap in Air, *IEEE Transactions on Power Apparatus and Systems* **PAS-95**:1019 (1976).

Asai, T. and A. Kasahara, A theoretical study of the compensating downward motions associated with cumulus clouds, *J. Atmos. Sci.* **24**:487 (1967).

Badaloni, S. and I. Gallimberti, The inception mechanism of the first corona in non-uniform gaps., *UPee Report* **72/05** (1972).

Baker, B., M. Baker, E. Jayaratne, J. Latham, and C. Saunders, Influence of Diffusional Growth Rates on the Charge Transfer Accompa- nying Rebounding Collisions Between Ice Crystals and Hailstones, *Q. J. R. Met. Soc.* **113**:1193 (1987).

Baker, M., H. Christian, and J. Latham, A One–Dimensional Model of Lightning from Convective Clouds., *Q. J. R. Met. Soc.* **121**:1525 (1995).

Battan, L. J., *The thunderstorm* (New American Library, New York, 1964).

Blyth, A., H. Christian, and J. Latham, Corona initation in thunderclouds., *Proc. 9th International Conference on Atmospheric Electricity* pp. 104–107 (1992).

BMRC, MCTEX operations summary, *http://www.bom.gov.au/meso/* (1995).

Bondiou, A., private communication.

Bondiou, A. and I. Gallimberti, Theoretical modelling of the development of the positive spark in long gaps., *J. Phys. D.* **27**:1252 (1994).

Bringi, V., K. Knupp, A. Detwiler, L. Liu, I. Caylor, and R. Black, Evolution of a Florida thunderstorm during the Convection and Precipitation/Electrification Experiment: the case of 9 August 1991, *Mon. Wea. Rev.* **125**:2131 (1997).

Castellani, A., A. Bondiou, A. Bonamy, P. Lalande, and I. Gallimberti, Laboratory simulation of the bi-leader process on an electrically floating conductor., *International Conf. on Lightning and Static Electricity* (1994).

Christian, H. and J. Latham, Satellite measurements of global lightning, *Q. J. R. Met. Soc.* **124**:1771 (1998).

Christian, H., R. L. Frost, P. H. Gillaspy, S. J. Goodman, O. H. Vaughn, M. Brook, B. Vonnegut, and R. E. Orville, Observations of optical lightning emissions from above thunderstorms using U-2 aircraft., *Bull. Am. Meteor. Soc.* **64**:120 (1983).

Christian, H., R. J. Blakeslee, S. J. Goodman, D. A. Mach, M. F. Stewart, D. E. Buechler, W. J. Koshak, J. M. Hall, W. L. Boeck, K. T. Driscoll, and D. J. Bocippio, The Lightning Imaging Sensor, *Proceedings of the 11th International Conference on Atmospheric Electricity* pp. 746–749 (1999).

Cooray, V., M. Berg, M. Akyuz, A. Larsson, M. Zitnik, and V. Scuka, Initiation of Ground Flashes: some microscopic electrical processes associated with precipitation particles., *Proc. of 24th International Conference on Lightning Protection (ICLP).* pp. 128–133 (1998).

Coquillat, S. and S. Chauzy, Computed conditions of corona emission from raindrops, *J. Geophys. Res.* **99**:16897 (1994).

Crabb, J. and J. Latham, Corona from colliding drops as a possible mechanism for the triggering of lightning, *Q. J. Roy. Met. Soc.* **100**:191 (1974).

Dawson, G., Pressure dependence of water-drop corona onset and its atmospheric importance, *J. Geophys. Res.* **74**:6859 (1969).

Dawson, G. and W. Winn, A model for streamer propagation., *Z. Phys.* **183**:159 (1965).

Dye, J., W. Winn, J. Jones, and D. Breed, The Electrification of New Mexico Thunderstorms, 1. The Relationship between Precipitation Development and the Onset of Electrification, *J. Geophys. Res.* **94**:8643 (1989).

Fletcher, N. M., *The Physics of Rainclouds* (Cambridge University Press, 1962).

Gallimberti, I., A computer model for streamer propagation., *J. Phys. D* **5**:2179 (1972).

Gallimberti, I., The mechanism of the long spark formation., *J. de Physique* **40**:193 (1979).

Gamache, J. and R. Houze, Water Budget of a Mesoscale Convective System in the Tropics, *J. Atmos. Sci.* **40**:1835 (1983).

Georgis, J., S. Chauzy, and S. Coquillat, Computed conditions of corona emission from two interacting raindrops., *Q. J. R. Met. Soc.* **121**:1853 (1995).

Griffiths, R. and J. Latham, Electrical corona from ice hydrometeors., *Q. J. Roy. Met. Soc.* **100**:163 (1974).

Griffiths, R. and C. Phelps, The effects of air pressure and water vapor content on the propagation of positive corona streamers, *Q. J. Roy. Met. Soc.* **102**:419 (1976a).

Griffiths, R. and C. Phelps, A Model for Lightning Initiation Arising From Positive Corona Streamer Development, *J. Geophys. Res.* **31**:3671 (1976b).

Gurevich, A., G. Milikh, and R. Roussel-Dupre, Runaway Electron Mechanism of Air Breakdown and Preconditioning During a Thunderstorm., *Phys. Let. A* **165**:463 (1992).

Gurevich, A., K. Zybin, and R. Roussel-Dupre, Lightning initiation by simultaneous effect of runaway breakdown and cosmic ray showers, *Phys. Let. A* **254**:79 (1999).

Hallet, J. and S. C. Mossop, Production of secondary ice production during the riming process., *Nature* **249**:26 (1974).

Harrison, M. and R. Geballe, Simultaneous measurements of ionozation and attachment coefficients., *Phys. Rev.* **91**:1 (1953).

Healey, R. and J. Reed, *The behavior of Slow Electrons in Gases* (Wireless Press, Sydney, 1941).

Helsdon, J. H., G. Wu, and R. D. Farley, An intracloud lightniing parameterization scheme for a storm electrification model., *J, Geophys. Res.* **97**:5865 (1992).

Holzworth, R. H. and Y. T. Chiu, Sferics in the stratosphere, *CRC Handbook of Atmospherics* **2**:1 (1982).

Houze, R., *Cloud Dynamics.* (Academic Press, San Diego, 1993).

Ibrahim, A. and H. Singer, Calculation of Corona Discharge in Positive Point to Plane Gaps., *7th Int. Conf. on Gas Discharges and their Applications* pp. 128–31 (1982).

Jayaratne, E., Thunderstorm Electrification: The Effect of Chemical Impurities in Cloud Water., *11th International Conference on Atmospheric Electricity* (1999).

Jayaratne, E., C. Saunders, and J. Hallett, Laboratory Studies of the Charging of Soft-Hail During Ice Crystal Interactions., *Q. J. R. Met. Soc.* **109**:609 (1983).

Kraus, A. B., F. Rohrer, E. S. Grobler, and D. H. Ehhalt, The global tropospheric distribution of NO_x estimated by a three-dimensional chemical tracer model., *J. Geophys. Res.* pp. 18 587–18 604 (1996).

Krehbiel, P., The electrical structure of thunderstorms., *The Earth's Electrical Environment* pp. 90–113 (1986).

Lawrence, M. G., W. Chameides, P. Kasibhatla, H. L. II, and W. Moxim, Lightning and atmospheric chemistry: The rate of atmospheric NO production., *Handbook of Atmospheric Electrodynamics* **1**:189 (1995).

Loeb, L., *Electrical Coronas - Their Basic Physical Mechanisms.* (University of California Press, Berkeley, 1965).

Lopez, R. and J.-P. Aubagnac, The lightning activity of a hailstorm as a function of changes in its microphysical characteristics inferred from polarimetric radar observations, *J. Geophys. Res.* **102**:16799 (1997).

Lucas, C., E. Zipser, and M. LeMone, Vertical velocity in oceanic convection off tropical Australia, *J. Atmos. Sci.* **51**:3183 (1994).

Lyons, W. A., T. Nelson, E. Williams, J. Cramer, and T. Turner, Enhanced positive cloud-to-ground lightning in thunderstorms ingesting smoke from fires., *Science* **282**:77 (1998).

Macky, W., Some investigations on the deformation and breaking of water drops in strong electric fields., *Proc. R. Soc.* **133**:565 (1931).

Marshall, T., M. McCarthy, and W. Rust, Electric Field Magnitudes and Lightning Initiation in Thunderstorms., *J. Geophys. Res.* **100**:20815 (1995).

McCarthy, M. and G. Parks, Further observations of X-rays inside thunderstorms., *Geophys Res Lett* **12**:393 (1985).

Meyers, M. P., P. J. DeMott, and W. R. Cotton, New primary ice nucleation parameterizations in an explicit cloud model., *J. Appl. Meteor.* **31**:708 (1992).

Molinie, J. and C. A. Pontikis, A climatological study of tropical thunderstorm clouds and lightning frequencies on the French Guyana coast., *Geophys. Res. Let.* **22**:1085 (1995).

Morris, C., *Dictionary of Science and Technology* (Academic Press, 1996).

Orville, R. and R. Henderson, Global distribution of midnight lightning: December 1977 to August 1978., *Mon. Wea. Rev.* **114**:2640 (1986).

Parks, G., B. Mauk, R. Springer, and J. Chin, X-ray enhancements detected during thunderstorm and lightning activities., *Geophys. Res. Lett.* **11**:1176 (1981).

Penney, G. and G. Hummert, Photoionization Measurements in Air, Oxygen, and Nitrogen., *J. Appl. Phys.* **41**:572 (1970).

Price, C. and D. Rind, A Simple Lightning Parameterization for Calculating Global Lightning Distributions., *J. Geophys. Res.* **97**:9919 (1992).

Pruppacher, H. R. and J. Klett, *Microphysics of Clouds* (D Reidel. Hingham, Boston, 1978).

Quickfield, *Quickfield* (http://www.tor.ru/quickfield/, 1996).

Rayleigh, L., On the equilibrium of liquid conducting masses charged with electricity., *Phil. Mag.* **14**:184 (1882).

Raymond, D., R. Solomon, and A. Blyth, Mass Fluxes in New Mexico Mountain Thunderstorms from Radar and Aircraft Measurements., *Q. J. R. Met. Soc.* **117**:587 (1991).

Richards, C. and G. Dawson, The hydrodynamic instability of water drops falling at terminal velocity in vertical electric fields., *J. Geophys. Res.* **76**:3445 (1971).

Rodi, A. R., *Study of the fine structure of cumulus clouds*, Ph.D. thesis, University of Wyoming (1981).

Rosenfeld, D. and I. Lensky, Spaceborne sensed insights into precipitation fromation process in continental and maritime clouds., *Bull. Am. Met. Soc.* **79**:2457 (1998).

Roussel-Dupre, R., A. Gurevich, T. Tunnell, and G. Milikh, Kinetic Theory of Runaway Air Breakdown and the Implications for Lightning Initiation., *Los Alamos Report* **LA-12601-MS**:1 (1993).

Rutledge, S., E. Williams, and T. Keenan, The Down Under Doppler and Electricity Experiment (DUNDEE): Overview and preliminary results., *Bull. Am. Met. Soc.* **73**:3 (1992).

Saunders, C., Thunderstorm Electrification Laboratory Experiments and Charging Mechanisms., *J. Geophys. Res.* **99**:10773 (1994).

Saunders, C., W. Keith, and R. Mitzeva, The Effect of Liquid Water on Thunderstorm Charging., *J. Geophys. Res.* **96**:11007 (1991).

Schonland, S. B., *The Flight of Thunderbolts* (Clarendon Press, Oxford, 1964).

Schroeder, V. and M. Baker, Inferring Selected Cloud Properties from Satellite Lightning Data., *11th International Conference on Atmospheric Electricity* (1999).

Schroeder, V., M. Baker, and J. Latham, A model study of corona emission from hydrometeors, *Q. J. R. Met. Soc.* **125**:1681 (1999).

Shao, X. and P. Krehbiel, The Spatial and Temporary Development of Intracloud Lightning., *J.Geophys. Res.* **101**:26641 (1996).

Solomon, R., *A Modelling Study of Thunderstorm Electrification and Lightning Flash Rate*, Ph.D. thesis, University of Washington (1997).

Solomon, R. and M. Baker, Electrification of New Mexico Thunderstorms., *Mon. Wea. Rev.* **122**:1878 (1994).

Solomon, R. and M. Baker, A One-Dimensional Lightning Parameterization., *J. Geophys. Res.* **101**:14983 (1996).

Solomon, R. and M. Baker, Lightning Flash Rate and Type in Convective Storms., *J. Geophys. Res.* **103**:14041 (1998).

Solomon, R., V. Hoffman, and M. Baker, Lightning Frequency and Type in Tropical Storms: Model and Observations, *10th International Conference on Atmospheric Electricity* (1996).

Solomon, R., V. Schroeder, and M. Baker, Lightning initiation - hydrometeor and cosmic ray hypotheses. (2000), not yet published.

Takahashi, T., Riming electrification as a charge generation mechanism in thunderstorms., *J. Atmos. Sci.* **28**:1536 (1978).

Taylor, G., Disintegration of water drops in an electric field., *Proc. Roy. Soc.* **280**:383 (1964).

Taylor, G., *A numerical investigation of sulphate production and deposition in midlatitude continental cumulus clouds*, Ph.D. thesis, University of Washington (1987).

Tyson, P. and P. D'Abreton, Transport and recirculation of aerosols off Southern Africa - macroscale plume structure., *Atmospheric Environment* **32**:1511 (1998).

Tyson, P., M. Garstang, R. Swap, P. Kallberg, and M. Edwards, An air transport climatology for subtropical Southern Africa., *Int. J. of Climatology* **16**:265 (1996).

Uman, M., *The Lightning Discharge* (Academic Press, Inc., San Diego, 1987).

Vonnegut, B., Possible mechanism for the formation of thunderstorm electricity, *Bull. Amer. Meteor. Soc.* **34**:378 (1953).

Wang, Y., D. JAcob, and J. Logan, Global simulation of tropospheric O_3-NO_x - hydrocarbon chemistry. 1. Model formulation., *J. Geophys. Res.* **103**:10713 (1998).

Westcott, N. E., Summertime cloud-to-ground lightning activity around major midwestern urban areas., *J. Appl. Met.* **34**:1633 (1995).

Williams, E., Large-scale charge separation in thunderclouds, *J. Geophys. Res.* **90**:6013 (1985).

Williams, E., private communication.

Williams, E., D. Rosenfeld, N. Madden, C. Labrada, J. Gerlach, and L. Atkinson, The Role of Boundary Layer Aerosol in the Vertical Development of Precipitation and Electrification : Another Look at the Contrast Between Lightning Over Land and Over Ocean., *11th International Conference on Atmospheric Electricity* pp. 754–57 (1999).

Wilson, C., *Proc. Cambridge Philos. Soc.* **22**:34 (1924).

Winn, W., G. Schwede, and C. Moore, Measurements of electric fields in thunderclouds., *J. Geophys. Res.* **79**:1761 (1974).

Yau, M., A two-cylinder model of cumulus cells and its application in computing cumulus transports, *J. Atmos. Sci.* **37**:2470 (1980).

Zipser, E., Deep Cumulonimbus Cloud Systems in the Tropics with and without Lightning., *Mon. Wea. Rev.* **122**:1837 (1994).

Vita

Vicki Schroeder was born in Cape Town, South Africa in 1971 to Sophia and John Hoffman. After the untimely death of her father in 1976 she and her brother were raised by their mother with strong emphasis on education as the key to their future. In 1992 Vicki graduated with a first class B.Sc (Hons) in Physics from the University of Cape Town. After stints as a geophysicist and teacher she entered graduate school at the University of Washington in 1994 together with her husband Brett. In 2000 she graduates with a Ph.D in Geophysics, the first Ph.D in her family.

During her time at the University of Washington Vicki also pursued non-academic goals. She represented the UW at National Collegiate Cycling Championships on 4 separate occasions earning 4 National Championship titles and two silver medals. The collegiate national championship represents the only opportunity for non-US citizens to earn the coveted stars and stripes jersey of a national champion.

Education:

Ph.D., Geophysics, University of Washington, Seattle, USA, 2000

B.Sc.(Hons), Physics, University of Cape Town, South Africa, 1992

Publications:

- Vicki Schroeder, M.B. Baker and John Latham, A model study of corona emission from hydrometeors, *Quarterly Journal of the Royal Meteorological Society*, 125, July 1999, Part A, pp 1681 - 1694.
- C.M. Comrie and V. Hoffman (Schroeder), Epitaxial CoSi2 formation by pulsed laser annealing, *South African Journal of Physics*, 1993.

Conference Presentations:

- Vicki Schroeder and M.B. Baker, Variations of Lightning Flash Rate with CCN Concentration, *American Geophysical Union Fall Meeting*, Dec 1999, San Francisco, USA.
- Vicki Schroeder and M.B. Baker, Inferring selected cloud properties from satellite lightning data, *3rd International GEWEX Conference*, June 1999, Beijing, China.
- Vicki Schroeder and M.B. Baker, Inferring selected cloud properties from satellite lightning data, *11th International Conference on Atmospheric Electricity*, June 1999, Huntsville, USA.
- Vicki Schroeder and M.B. Baker, Corona initiation from raindrops - a step towards solving the lightning initiation problem, *51st Gaseous Electronics Conference*, October 1998, Maui, USA.
- Vicki Schroeder and M.B. Baker, Vertical water transport by convective systems, *American Meteorological Society Conference on Cloud Physics*, August 1998, Everett, USA.
- Vicki Schroeder and M.B. Baker, Corona from colliding hydrometeors - a model study, *American Geophysical Union Fall Meeting*, December 1997, San Francisco, USA.
- R. Solomon, Vicki Hoffman (Schroeder) and M.B. Baker, Lightning frequency and type in tropical storms: model and observations, *10th International Conference on Atmospheric Electricity*, June, 1996, Osaka, Japan.
- Vicki Schroeder and M.B. Baker, Pure corona from colliding raindrops, *American Geophysical Union Fall Meeting*, Dec. 1995, San Francisco, USA.
- C.M. Comrie and V. Hoffman (Schroeder), Laser induced epitaxial CoSi2 formation, *Materials Research Society Conference*, Boston, 1994